Master's thesis

NTNU
Norwegian University of Science and Technology
Faculty of Natural Sciences
Department of Physics

Endre Jacobsen

Scanning Precession Electron Diffraction Template Matching for Automated Phase Mapping of Precipitates in 6xxx Aluminium Alloys

Master's thesis in Applied Physics and Mathematics

Supervisor: Antonius Theodorus Johannes van Helvoort

August 2020

NTNU
Norwegian University of
Science and Technology

Endre Jacobsen

Scanning Precession Electron Diffraction Template Matching for Automated Phase Mapping of Precipitates in 6xxx Aluminium Alloys

Master's thesis in Applied Physics and Mathematics
Supervisor: Antonius Theodorus Johannes van Helvoort
August 2020

Norwegian University of Science and Technology
Faculty of Natural Sciences
Department of Physics

NTNU
Norwegian University of
Science and Technology

Abstract

Aluminium alloys are of technological importance. In the Al-Mg-Si-(Cu) (6xxx series) the mechanical properties are determined by precipitate phases formed after thermo-mechanical treatment. This study is the analysis of model-based template matching on scanning precession electron diffraction data for model-based phase mapping of the β', β'' and Q' precipitates. A concrete result is a constructed Jupyter notebook for phase mapping and the associated method for phase mapping. The notebook is able to map the precipitates β'', β' and the Al matrix accurately. The approach is based on a novel sampling routine using the orientation relationships between the phases and Al. This sampling routine achieved symmetry order invariance and a 10^4 magnitude reduction of the required template library. An orientation sampling resolution of 1.2° proved to be the coarsest resolution that still was able to distinguish these three phases in experimental datasets taken with default equipment. The reduction of the template bank allows most personal computers to perform the template matching routine in a reasonable time-frame without running out of RAM. A 8 GB RAM computer can perform the template matching routine with up to 2500 templates. In order to distinguish Al, β' and β", the old method requires around 6 000 000 templates, while the new method only requires around 1000. The results show that the deviation parameter s_{max}, is of upmost importance. For each phase and for each phase combination, there is a closed interval of s_{max} values that are able to provide good matches and that is able to distinguish the phases. A method for finding these intervals and using them to predict the possible s_{max} intervals for a template library with any combination of phases has been developed. The work has shown that pixel by pixel intensity based correlation functions for model-based template matching has two main weaknesses. The first weakness is when there is a relative reflection density difference between the phases, where the most dense phase will get a higher correlation score. The second weakness is when there is a relative intensity difference between the reflections of the phases, then the phase with the most intense reflections will be favored. More intense reflections also lowers the signal to noise ratio, which in turn increases the reflection density. A new method for determining an initial guess for s_{max}, has been developed using the intensity of the minimum detectable signal as a threshold to decrease the signal to noise differences between the phases. The results show that the current approach, using pixel by pixel correlation functions, is unable to distinguish the near identical β' and Q' patterns. Four pixel by pixel correlation functions have been tested, and normalized cross correlation achieved the best correlation scores and exhibited the best phase distinction. For future work, three approaches on improving the speed of the code has been presented, two proposals on improving the simulation has been presented, three alternative correlation functions have been suggested and improvements on the experimental side have been argued for.

Sammendrag

Aluminiumslegeringer er viktige i et teknologisk perspektiv. I Al-Mg-Si-(Cu) (6xxx serien) er de mekaniske egenskapene bestemt av presipitatfaser dannet etter termomekanisk behandling. Denne studien er en analyse av modellbasert malsammenligning av sveipe-presesjons-elektrondiffraksjons-datasett (SPED) for modellbasert fasetilordning av β', β" og Q' presipitater. Et konkret resultat er en konstruert Jupyter notisbok for fasetilordning og den assosierte fasetilordningsmetoden. Notisboken kan fasetilordne β', β" og Al presipitatene presist. Metoden er basert på en ny samplingsmetode som bruker orientasjonsrelasjonene mellom fasene og Al. Denne samplingsmetoden oppnådde symmetriorden-invarians og en reduksjon i det nødvendige malbiblioteket av størrelseorden 10^4. En vinkeloppløsning på 1.2° er den groveste oppløsningen som klarte å skille mellom de tre fasene i det eksperimentelle datasettet tatt med standardutstyr. Reduksjonen av malbanken gjør det mulig for personlige datamaskiner å utføre malsammenligningsmetoden uten å bruke for mye RAM. En 8 GB RAM datamaskin kan kjøre malsammenligningsmetoden for opp til 2500 maler. For å skille mellom Al, β' og β" kreves det rundt 6 000 000 maler med den gamle metoden. Den nye metoden trenger kun ca. 1000. Resultatene viser at eksitasjonsfeilparameteren s_{max} er viktig. For hver fase og for hver fasekombinasjon er det et lukket intervall av s_{max} verdier som kan brukes for å få gode matcher og som klarer å skille fasene fra hverandre. En metode for å finne dette intervallet og bruke dem til å forutsi de mulige s_{max} verdiene for et malbibliotek med hvilken som helst kombinasjon av faser har blitt utviklet. Arbeidet har vist at korrelasjonsfunksjoner som sammenligner intensiteten piksel for piksel for modellbasert malsammenligning har to svakheter. Den første svakheten er når det er en relativ refleksjonstetthetsforskjell mellom fasene, hvor de tetteste fasene vil få en høyere korrelasjonsskår. Den andre svakheten er når det er en relativ intensitetsforskjell mellom refleksjonene til fasene, da vil fasen med de mest intense refleksjonene bli foretrukket. Mer intense refleksjoner vil også senke signal til støy raten, som videre vil øke refleksjonstettheten. En ny metode for å estimere en begynnelsesverdi for s_{max} har blitt utviklet ved å bruke intensiteten til det laveste detektbare signalet som en terskel for å minke signal til støy differansen mellom fasene. Resultatet viser at den gjeldene metoden, som bruker korrelasjonsfunksjoner basert på piksel for piksel sammenligning, ikke klarer å skille mellom de svært like fasene β' og Q'. Fire korrelasjonsfunksjoner basert på piksel for piksel sammenligning har blitt testet, og normalisert krysskorrelasjon oppnådde den høyeste korrelasjonskåren og den beste fasedistinksjonen. For videre arbeid har tre muligheter for å øke hastigheten av koden, to forslag for å forbedre simuleringen og tre alternative korrelasjonsmetoder blitt foreslått. Flere forbedringer av den eksperimentelle delen har også blitt argumentert for.

Preface and Acknowledgements

This work is submitted as part of the requirements for the degree of Master of Science in Physics and Mathematics from the Norwegian University of Science and Technology (NTNU) in Trondheim. The work presented herein is in part a continuation of a 15 ECTS project work completed in the fall of 2019. The work was carried out in the spring of 2020, during the global COVID 19 pandemic, under the guidance of Professor Antonius Theodorus Johannes van Helvoort at the department of physics. The TEM data acquisition was done by Jonas Sunde. All method development and data analysis presented is the work of the author. All figures in the work are made by the author using a combination of Inkscape, Matplotlib and Vesta.

First of all, I want to thank my supervisor Professor Antonius T. J. van Helvoort for his excellent guidance. The weekly meetings have not only been a help for this work, but also inspirational and motivational. Thank you for proofreading the work, and for constructive feedback. I have learnt a lot.

I would also like to thank Jonas Sunde, as this is a continuation of some of his work. His expertise on the material system has been invaluable. He also provided me with the data sets which I have analyzed in this work.

I want to thank Doctor Duncan N. Johnstone and Philip Crout from the Electron Microscopy Group at the University of Cambridge. Through Skype meetings, numerous e-mails and Github conversations, I have been encouraged to contribute to pyXem and been guided in the right direction when I have been stuck.

Another thank you goes to Tina Bergh, Eirik Opheim and Håkon W. Ånes for constructive discussions and helpful suggestions.

Lastly, I want to give a special thank you to my mother Sonja I. Madsen and father Yngve Jacobsen. Without their unwavering support, and their continuous encouragement, I would not be where I am today. Thank you both for nurturing my curious mind and always being there for me. I am forever grateful, thank you.

Abbreviations

CCD Charge Coupled Device

CCW Counterclockwise

ED Electron Diffraction

FOLZ First-order Laue Zone

GUI Graphical User Interface

HOLZ Higher-order Laue Zone

IPF Inverted Pole Figure

NCC Normalized Cross Correlation

NMF Non-Negative Matrix Factorisation

OA Optical Axis

OR Orientation Relationship

PED Precession Electron Diffraction

SA Selected Area

SAD Sum of Absolute Differences

SP Stereographic Projection

SPED Scanning PED

SSD Sum of Squared Differences

ST Stereographic Triangle

TEM Transmission Electron Microscopy

VDF Virtual Dark Field

ZA Zone Axis

ZNCC Zero Mean Normalized Cross Correlation

ZOLZ Zeroth-order Laue Zone

Contents

Chapter 1

Introduction

This master thesis is structured into seven chapters: Introduction, theory, method, results, discussion, conclusion and future work. The introduction chapter, chapter 1, will provide the motivation and background of the work along with the problem statement. The theory chapter, chapter 2, gives a theoretical framework in which the rest of the work will rely upon. The method chapter, chapter 3, presents the TEM sample preparation, the image processing steps applied to the experimental data and the model simulation of diffraction with the associated python code, presented conveniently in a Jupyter Notebook file format. The results are presented in chapter 4. The following discussion chapter, chapter 5, discusses the results. The conclusion chapter, chapter 6, summarizes the results and discussion chapters. The future work chapter, chapter 7, summarizes the discussion of the results and provide concrete suggestions for further work.

1.1 Motivation

What lies beyond what we can see with our eyes? This is a question that has been asked by mankind for millennia. In fact the earliest known accounts of objects resembling lenses date back almost 4000 years. Though, a widespread use of simple lenses did not arrive before the 13th century, when the magnifying lenses were used as eyeglasses.[1] Galileo Galilei (also sometimes cited as the compound microscope inventor) arranged convex and concave lenses in a certain way such that light could enter and magnify the object. Galilei named this device "occhiolino" or "little eye" - in modern days known as *the microscope*.[2]

It is almost a rule that advances in scientific thought originate in the development of new tools or techniques of investigation. This has truly been the case in metallurgy and microscopy. It was long known that heat-treating a sword would harden it, but why this happened was not known until the microscopes were good enough. In the early 20th century a significant alternative to the light microscope was developed, namely the electron microscopes. The first prototype was made in 1933 by the German physicist Ernst Ruska.[3] Electron microscopes has given us the ability to understand (and even control) the properties of alloys.[2]

Aluminium based alloys are of upmost interest due to increasing demand for alloys that combine high strength, formability, low weight and corrosion resistance. Important applications include transport, construction and packaging. Al is the most heavily consumed non-ferrous metal in the world, with a world annual consumption at 24 million tons. Al, in the form of Al compounds such as Bauxite, is also the second most plentiful metallic element on Earth.[4]

The key for using Al based alloys is controlling its properties through controlling its structure via composition and thermo-mechanical history. Each step of this thermo-mechanical process will alter the nano/microstructure and thereby the properties of the alloy. Strength, ductility, thermal- and electrical conductivity are examples of important properties that can be controlled by tailoring the alloy's thermo-mechanical history.

For technical alloys, control over the the formation of small secondary phases, precipitates, is crucial. From an engineering viewpoint, dispersing fine precipitate particles over the matrix at high density is a common technique for improving the strength of metals and alloys. The movement of dislocations is inhibited by the strain field around the precipitates. Different precipitates will disperse at difference temperatures and will give a characteristic strain field.

This leads to a few questions that, when answered, will provide a measure of control (and understanding) of the Al alloy properties,

- What phases are present in the alloy?
- What is the density of the precipitates? (Precipitate count)
- What is the distribution of the precipitates? (Where are the precipitates located)
- How do precipitates evolve upon further thermo-mechanical treatment?
- How does one precipitate change into another precipitate? (How do they grow / annihilate)

A typical precipitate has a cross section of a few nm^2 and a length of a few nm. Thus, tools with high spatial resolution is needed. Microscopes can only observe an object with a length less than half the wavelength of the microscope's illumination source. This criterion, Rayleigh criterion[5], excludes the light microscope as the wavelength of visible light lies between 380 to 700 nm. Thus, another illumination source is needed.

Transmission Electron Microscopy (TEM) can achieve spatial resolutions of less than 1 Å (0.1 nm) as the wavelength (with 200 kV applied voltage) is about 25 pm. This is more than enough to satisfy Rayleigh criterion and allows quantification and identification of the secondary phases present in the alloy[5]. Lens imperfections are still a limitation, but modern TEMs reaches a sufficient resolution. Detector and lens technology is constantly improving and the mysteries of the nano-world is slowly unfolding.

Manual image-based precipitate identification and quantification is a tedious task, especially for statistically meaningful numbers. In order to get significant results with small error margins, a large area must be imaged. "Zooming in" on one part of the sample will not reveal the possible variations in precipitate types, sizes and distribution. Hence, it is paramount to develop an algorithm (or method) that is able to analyze large areas in a reasonable time-frame. This will allow for a statistical approach, which in turn will increase the sample size and lower the error margin.

A fundamental rule in the scientific method is that all research should be reproducible. This warrants the use of a physical model-based on a theoretical framework, utilizing a set of assumptions and axioms. Manual precipitate identification and quantification is prone to human error and is intrinsically subjective.[6] Automatic comparison of TEM images with a physical model on the other hand is an objective metric which can be reproduced.

Fortunately, the world of crystallography makes use of symmetry in its description. All possible three-dimensional crystal symmetries are described with 230 discrete number of space groups. This gives us the possibility to create databases of every possible configuration, with as high precision as needed. Furthermore, these large data bases can be analyzed automatically and the outcomes can be verified against a physical model.

Finally, another important aspect is transparency and accessibility. Open source programming deals with this facet quite beautifully. In contrast to most commercial software, each line of code is easily accessible and the user will have full control over the underlying assumptions. Giving the user full access to the internal workings of the program will remove the black-boxing effect found in commercial software. This makes the method more transparent, which in turn makes the research easier to reproduce and to justify. A major benefit to open-source programming is that it allows for collaboration between researchers all over the world.

1.2 Problem Statement

The work in this master thesis is a continuation of a 15 ECT credits project work from the fall of 2019, with the focus on handling large SPED data sets in open-source Python-based platforms. The overall goal of the project is to incorporate model-based verification of Non-Negative Matrix Factorisation (NMF) based precipitation counting and identification. Starting point is the work by Sunde et al [6].

The project work ended with a list of suggestions for future work, and the current work aim to follow up on these suggestions. First, a suggested new way of "sampling the orientations for each phase in the template library utilizing the known orientation relationships between the phase and the Al-matrix", as sampling all orientations is not necessary and will limit the attainable resolution. Secondly, it is suggested that "alternative correlation functions must be implemented and tested to attempt to distinguish almost identical phases", as the current approach[7] might be skewed.

The Al-Mg-Si(-Cu) (6xxx series) alloys form one of the main groups of age-hardening Al alloys. Aging forms a limited number of possible precipitates - some well studied with established orientation relationships. This knowledge is currently not used for template phase mapping. Certain precipitates enhances properties in the alloy, such as a hardening of the material. The occurrence of the precipitates are seen in TEM images, and the precipitates can be manually labeled and categorized. Inferring the occurrence of precipitates from just a tiny area gives rise to large uncertainties. Therefore, on the data acquisition side, automation through scanning approaches over larger volumes instead of sequential (i.e. precipitate-by-precipitate imaging) is important. Using available computer resources to do the large data analyses, statistics and phase mapping is the next logical step.

Sunde et al[6] has through a series of preprocessing operations and NMF been able to reduce the problem size significantly. The machine learning algoritm has decomposed the problem to around 100 candidates. However, from studying the system, we know that there is only 9 possible candidates. Therefore, each of the 100 candidates will need to be manually matched with the right phase. This matching step is what this project aims to automatize.

Currently, precipitate identification is done using the commercial software NanoMegas Index.[8] Due to its commercial nature, and the fact that there exists a monopoly, the software is expensive and further developments since its launch has been incremental. This lowers the accessibility and consequently leads to less research being achieved. The software is also 'blackboxed' behind a Graphical User Interface (GUI). The user has some measure of control on the input variables, however the researcher have little to no control over the underlying calculations, assumptions or simulations. This lowers the reproducibility, transparency and credibility of the research done. Therefore, it is a worthy pursuit to make software accessible to everyone. Non-profit open-source frameworks can achieve this accessibility.

Python is the chosen programming-language for this task. As an interpreted language, in opposition to a compiled language, Python provides an intuitive and readily accessible platform for researchers of all levels. Python has become the lingua franca in science and allows for seamless collaboration between different researchers.[9] Python is also free, which has lead to a plethora of packages and libraries being developed. However, a compromise on computational speed is taken when choosing an interpreted language. Compiled languages such as Fortran or C is faster which in turn allows for larger data sets to be analyzed. Tackling Python's inherent computational bottleneck with clever usage of symmetry and physics is paramount.

The overall goal of the project is to make a matching procedure that is able to map precipitates accurately and integrate this into Sunde et Als. [6] procedure, so an automatic (minimal user input) procedure becomes available. This will not just allow Sunde et al. procedure to be fully automated, but will also be a useful procedure for anyone wanting to map out precipitates. This is an enormous task and decomposing the problem into sub-tasks is necessary.

This work will analyze a Scanning PED (SPED) data set of a Al-Mg-Si-(-Cu) system that has been heat treated as to only contain the following phases: Pure Al, hexagonal β'' and monoclinic β'. The first milestone is to be able to distinguish and map out these three candidates accurately. The next step is then to introduce more complex data sets containing more precipitates, and lastly when the code is able to distinguish all the phases accurately, use it on preprocessed/NMF data sets. When all of these steps are completed, a fully automated precipitate matching procedure is achieved, and a statistical approach to phase mapping precipitates is presented.

Chapter 2

Theory

This chapter gives a theoretical framework in which the rest of the work will rely upon. Section 2.1 introduces all crystal structures both in real space and in reciprocal space. Section 2.2 provides fundamental theory about diffraction, deriving the diffraction conditions both in real space and in reciprocal space. This section also introduces the wave-particle duality, from which a few important properties are derived. Section 2.3 introduces the TEM and explains the various parts of the TEM column. Section 2.4 introduces the microscopy technique SPED. Section 2.5 introduces the concept of precipitation and also provides important characteristics about the Al-Mg-Si(-Cu) system, which has been analyzed in this work. Lastly, section 2.6 gives the theoretical framework for template matching.

2.1 Basic Crystallography

2.1.1 Characterisation of Crystal Structures

Lattice types

The following deduction follows De Graef.[5, pp 1-5]. Ideal crystals are constructed by infinite repetition of identical groups of atoms. A group is called the basis. The *lattice* is defined as the set of points which is created by integer linear combinations of the three basis vectors a_1, a_2 and a_3. In other words, the lattice $\mathcal{T}$ is the set of all vectors $\mathbf{t}$ of the form

$$\boldsymbol{t} = u_1\boldsymbol{a_1} + u_2\boldsymbol{a_2} + u_3\boldsymbol{a_3}, \quad u_i \in \mathbb{Z} \tag{2.1}$$

or, using Einstein's summation convention

$$\boldsymbol{t} = u_i\boldsymbol{a_i}, \quad u_i \in \mathbb{Z} \tag{2.2}$$

In order to distinguish between different crystal systems, we need to know the lengths of the translation vectors: $|\boldsymbol{a_1}| \equiv a$. $|\boldsymbol{a_2}| \equiv b$ and lastly $|\boldsymbol{a_3}| \equiv c$. We will also need to know the angles between the vectors, α, β and γ. These six numbers a, b, c, α, β, γ are known as the *lattice parameters* of the unit cell. With these lattice parameters we can derive seven primitive lattice types, which are presented in Table 2.1.

Table 2.1: The seven primitive lattice types

$\{a,\ b,\ c,\ \alpha,\ \beta,\ \gamma\}$	$a \neq b \neq c;\ \alpha \neq \beta \neq \gamma$	triclinic or anorthic (a);
$\{a,\ b,\ c,\ \frac{\pi}{2},\ \beta,\ \frac{\pi}{2}$	$a \neq b \neq c;\ \beta \neq \frac{\pi}{2}$	monoclinic (m):
$\{a,\ a,\ c,\ \frac{\pi}{2},\ \frac{\pi}{2},\ \frac{3\pi}{2}\}$	$a = b \neq c$	hexagonal (h)
$\{a,\ a,\ a,\ \alpha,\ \alpha,\ \alpha\}$	$a = b = c;\ \alpha \neq \frac{\pi}{2}$	rhombohedral (R)
$\{a,\ a,\ c,\ \frac{\pi}{2},\ \frac{\pi}{2},\ \frac{\pi}{2}\}$	$a \neq b \neq c$	orthorhombic (o);
$\{a,\ a,\ c,\ \frac{\pi}{2},\ \frac{\pi}{2},\ \frac{\pi}{2}\}$	$a = b \neq c$	tetragonal (t);
$\{a,\ a,\ a,\ \frac{\pi}{2},\ \frac{\pi}{2},\ \frac{\pi}{2}\}$	$a = b = c$	cubic (c);

We can place more lattice sites at the end points of *centering vectors*:

$$\boldsymbol{A} = \left(0, \frac{1}{2}, \frac{1}{2}\right), \quad \boldsymbol{B} = \left(\frac{1}{2}, 0.\frac{1}{2}\right), \quad \boldsymbol{C} = \left(\frac{1}{2}, \frac{1}{2}, 0\right), \quad \boldsymbol{I} = \left(\frac{1}{2}, \frac{1}{2}, \frac{1}{2}\right). \tag{2.3}$$

Thus, by combining one of the seven primitive lattice systems with one of the centering types, we obtain some more lattice systems. August Bravais derived in 1850 that there are 14 unique lattices, as some of the combinations found are equivalent to each other.[10] These 14 lattices are called *Bravais lattices*, and are represented by the crystal system symbol followed by a centering symbol as shown in Figure 2.1.

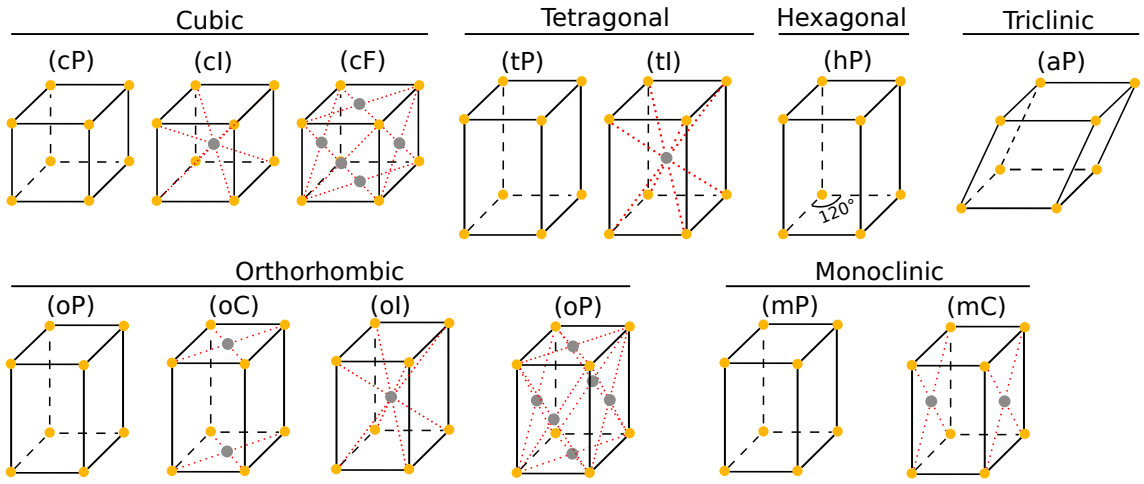

Figure 2.1: The 14 Bravais lattices. Each lattice is represented with the crystal system symbol and a centering symbol.

Symmetry operations

There are four different symmetry operations which may be applied to the Bravais lattices. These operations are translations, rotations, reflections and inversions. Moreover, these operations can be combined to unique groups, as for example rotation and reflection (e.g 2/m) or two sequential rotations on different axis (e.g 23). It can be shown that only a finite number of these combinations are possible for the 14 Bravais lattices, and that only one-fold, two-fold, four-fold and six-fold rotations has to be considered. The operators 1, 2, 4, 6, m, $\bar{1}$ are respectively used for n-fold rotation, mirroring and inversion. The definition of the symmetries may be found in a standard crystallography textbook, i.e *Essentials of Crystallography* by McKie.[11]

Only six combinations of multiple rotation axes are possible for any given Bravais lattice.[11, 10] When combining these six combinations with all possible combinations of mirror planes and inversions, one attains a finite number of possibilities. In total, we get 32 *point groups*.

The 32 point groups does not take into account the translation symmetry elements, namely the glide planes and screw axes. A *screw axis*, $\boldsymbol{n_m}$, is a combination of a Counterclockwise (CCW) rotation around $2\pi/n$ and a translation $\boldsymbol{T} = \frac{m}{n}\boldsymbol{t}$ where $\boldsymbol{t}$ is a translation vector $(m, n = \mathbb{Z})$. A *glide plane* is a combination of a mirror with a translation over half a lattice parallel to the mirror plane.

A point group describes the symmetry of a crystal with respect to a single static point. When combining point groups with Bravais lattices and eventually including translation symmetry, one attains 230 *space groups*. Every crystal system in the world can be assigned to one of the 230 space groups. There are two different notation systems in use for naming the point and space groups, Schonflies and Hermann-Mauguin notation. I.e a two-fold rotation with reflection is named 2/m in Hermann-Mauguin notation and C_{2h} in Schonflies notation. In this work, Hermann-Mauguin notation will be used. The fact that there is a discrete number of space groups has a profound effect, as one thus may catalogue all crystal systems. Group theory allows us to relate crystal systems (e.g cubic), to the Bravais lattice (P, I, F), to point group (e.g 23) to space group (e.g P23). Section 2.6 will show why this is important when dealing with them digitally and describing them in computer software.

The *symmetry order* of an crystal system is the number of different but indistinguishable arrangements of the crystal system. I.e a triclic crystal from the pedial point group has no symmetries, so the symmetry order is 1 - there is only one arrangement that gives different but equivalent views of the crystal system. On the other end of the spectrum lies cubic structure, i.e Al, with a symmetry order 24.

Stereographic projection

The Stereographic Projection (SP) is a construction which projects a directional property of a 3D crystal onto a 2D disc (equatorial plane). The projection conserves angles, meaning that a measurement of an angle on the equatorial plane corresponds to the real 3D angle. Figure 2.2 shows a schematic overview of the SP of the normals on crystal phases. The construction is quite straightforward, in order to get the SP of the point P, connect P with S. The intersection with the equatorial plane is the SP of P. It is clear that every possible orientation of the crystal is mapped onto the equatorial plane, and this fact proves useful for crystallography and TEM.[12, pp 29-31]

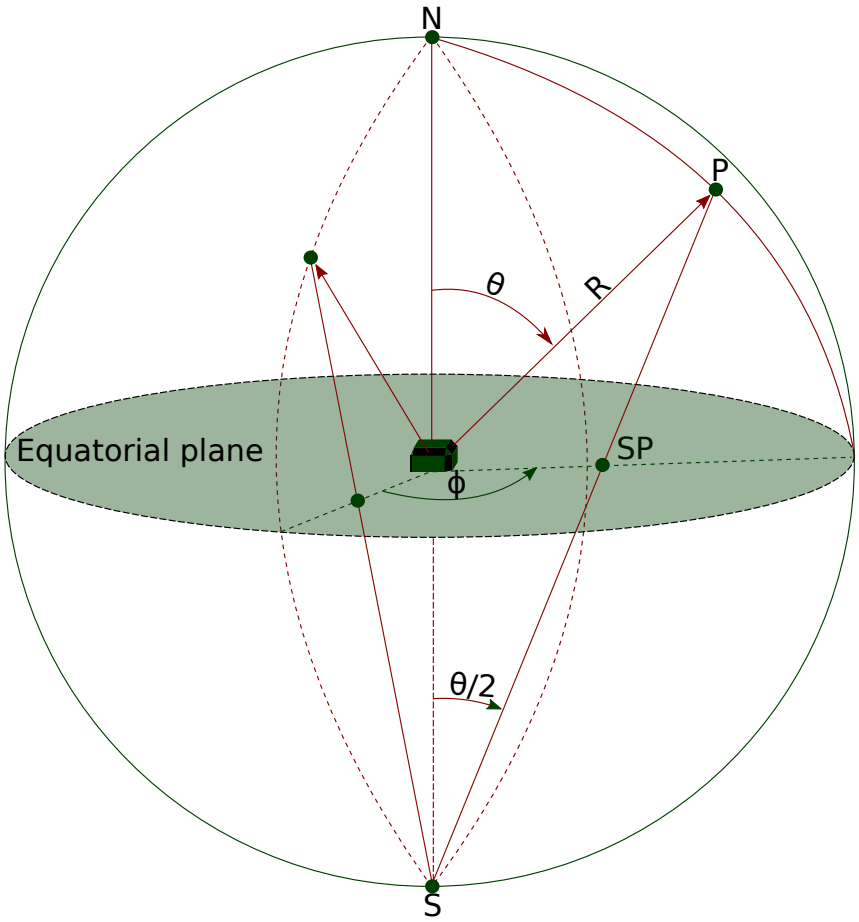

Figure 2.2: Schematic overview of a stereographic projection of the normals on crystal faces. R is the radius of the sphere, SP is the stereographic projection of point P(R, ϕ, θ) on the sphere, which is achieved by mapping the intersection on the equatorial plane from a beam from P to S. Figure inspired by [5, p. 30].

As the SP can represent information about all possible three-dimensional orientations of a crystal, and with the knowledge that each crystal system has a certain symmetry order, it is easy to see that some of the orientations given by the SP are equivalent. In fact, all of the possible orientations may be mapped onto a triangle.[1] This construction is called the Stereographic Triangle (ST)(also known as Inverted Pole Figure (IPF)). The ST for crystal systems for a few symmetry orders, are shown in Figure 2.3.

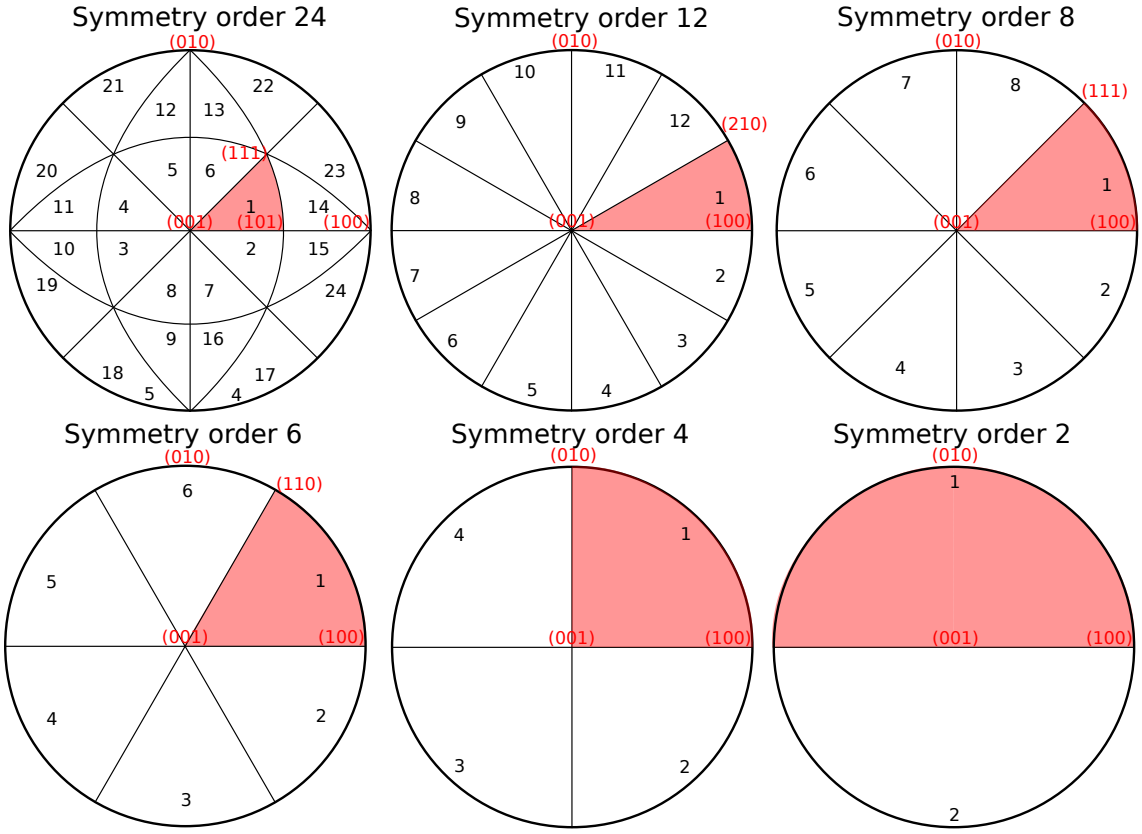

Figure 2.3: Stereographic triangles for symmetry orders; 2, 4, 6, 8, 12, 24. The equatorial plane (disk) from Figure 2.2 can be mapped to a triangle(shown in red) due to some orientations being equivalent due to the inherent symmetry of the crystal system.[13]

[1]Except for triclinic crystal systems, as they have symmetry order 1.

2.1.2 Planes and Reciprocal Lattice

Miller indices

The orientation of a crystal plane is determined by three points and may be represented using numerous systems. However, the crystallography-world has determined William H. Millers system from 1839 to be the most fitting.[14, 12] The Miller system of indexing is quite straightforward, as seen with Figure 2.4 in conjunction with the the following recipe:

- Find intercept on the axes in terms of the lattice parameters $\boldsymbol{a_1}$, $\boldsymbol{a_2}$, $\boldsymbol{a_3}$.
- Take the inverse of these numbers and then, by keeping the same ratio, reduce the integers to the smallest three integers.[14]

The three integer *Miller indices*, (hkl), may denote a single plane or a set of parallel planes. Planes that are equivalent by symmetry are denoted by curly braces, e.q the set of cube faces is $\{100\}$. There is no (except in special cases) fixed relation between the orientation of the vector t from (2.1) with respect to the plane (hkl).

A Zone Axis (ZA) (denoted by [uvw]) is parallel to a family of lattice planes of Miller indices (hkl) if Weiss law is fulfilled:[14]

$$uh + vk + wl = 0. \tag{2.4}$$

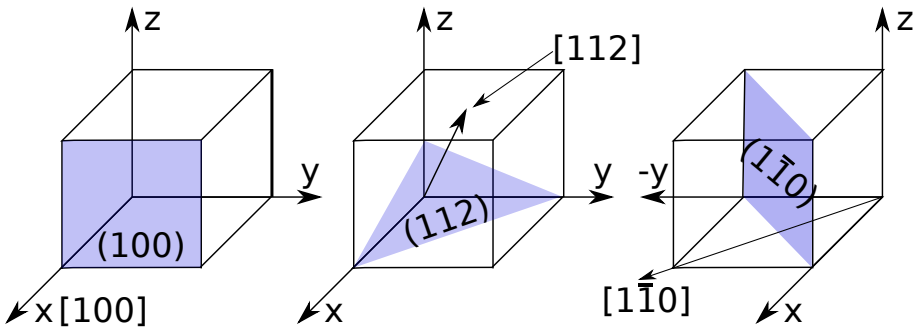

Figure 2.4: Miller indices construction. Indices and plane normals of three planes in a cubic crystal. Intercepts (x,y,z) from left to right: (1,0,0), (1,1,1/2), (1,-1,0).

Reciprocal lattice

We want to relate the miller indices (hkl) to the basis vectors $\boldsymbol{a_1}$, $\boldsymbol{a_2}$, $\boldsymbol{a_3}$, hence we must find a new triplet of basis vectors, $\boldsymbol{a_1^*}$, $\boldsymbol{a_2^*}$, $\boldsymbol{a_3^*}$, in which the vector

$$\boldsymbol{g} = h\boldsymbol{a_1^*} + k\boldsymbol{a_2^*} + l\boldsymbol{a_3^*} \tag{2.5}$$

conveys meaningful information about the plane. It turns out that such an arrangement exists, and they are known as the *reciprocal basis vectors* and have a dimension of [1/length]: [2]

$$\boldsymbol{a_1^*} = 2\pi\frac{\boldsymbol{a_2}\times\boldsymbol{a_3}}{\boldsymbol{a_1}\cdot\boldsymbol{a_2}\times\boldsymbol{a_3}}; \quad \boldsymbol{a_2^*} = 2\pi\frac{\boldsymbol{a_3}\times\boldsymbol{a_1}}{\boldsymbol{a_1}\cdot\boldsymbol{a_2}\times\boldsymbol{a_3}}; \quad \boldsymbol{a_3^*} = 2\pi\frac{\boldsymbol{a_1}\times\boldsymbol{a_2}}{\boldsymbol{a_1}\cdot\boldsymbol{a_2}\times\boldsymbol{a_3}}. \tag{2.6}$$

2.1.3 Rotation Conventions

In linear algebra, a rotation matrix is a matrix that is used to perform rotation in Euclidean space. The basic rotation matrices defined in Equation 2.7 rotate vectors by an angle θ about the x-, y- and z-axis in Euclidean space.

$$R_x(\theta) = \begin{bmatrix} 1 & 0 & 0 \\ 0 & \cos(\theta) & -\sin(\theta) \\ 0 & \sin(\theta) & \cos(\theta) \end{bmatrix} \tag{2.7}$$

$$R_y(\theta) = \begin{bmatrix} \cos(\theta) & 0 & \sin(\theta) \\ 0 & 1 & 0 \\ \sin(\theta) & 0 & \cos(\theta) \end{bmatrix} \tag{2.8}$$

$$R_z(\theta) = \begin{bmatrix} \cos(\theta) & -\sin(\theta) & 0 \\ \sin(\theta) & \cos(\theta) & 0 \\ 0 & 0 & 1 \end{bmatrix} \tag{2.9}$$

Calculating the rotation matrix is computationally taxing. For rigid bodies, it is possible to decompose the rotational matrix to individual degrees of freedom. Leonard Euler proved in 1775 that pure rotation about a fixed point is governed by the following theorem (Euler's rotation theorem)[15]:

Theorem 1 *The general displacement of a rigid body with one point fixed is a rotation about some axis.*

[2] A full deduction of the reciprocal basis vectors is given by Kittel.[14, p. 27-29]

Thus, it is always possible for such a rotation to find an axis through the fixed point oriented at particular polar angles α and β such that a rotation about another angle γ about this axis duplicates the general rotation. Therefore, one only needs three parameters(angles) to fully describe a rotation. When these rotations are done in succession in a specific sequence they are called *Euler Angles*, and are often inserted into a Euler angle vector $[\alpha, \beta, \gamma]$.

The convention that will be used in this work is widely used in solid-state physics and crystallography and is named 'rzxz'. The first character is 'r' (rotation), meaning that the rotation also changes the alignment of the axes, contrary to 's'(static) where the axes are fixed. The last three characters specify how the rotation is done. First z is rotated by α, then the new x is rotated by β, and finally the new z is rotated by γ as illustrated in Figure 2.5.

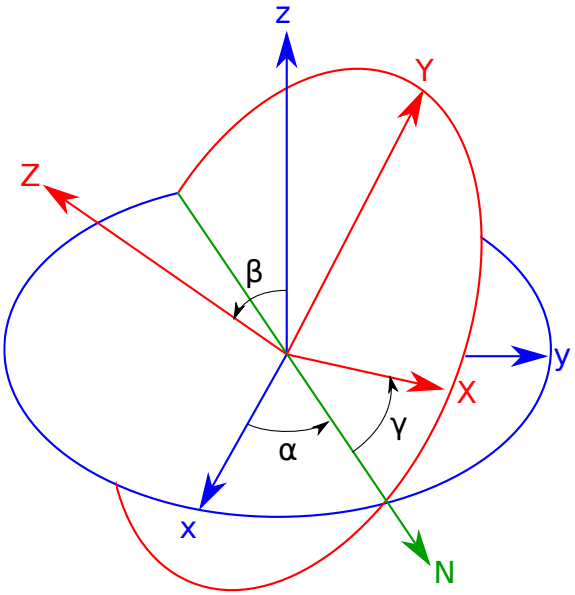

Figure 2.5: Schematic drawing of the Euler angles. The rotation convention used in this work. First a rotation is performed about z (by α), then the new x (by β), and finally the new z (by γ).

2.2 Diffraction

The previous section, section 2.1, laid the foundation to describe all possible 3D crystals in a systematic way. It also introduced a formalism describing orientations which is used throughout the work. When we study a crystal structure, we study it through *diffraction* of photons, neutrons or electrons on the regular lattice. This section will give the necessary Electron Diffraction (ED) theory that is utilized to collect signatures of the experimental lattice and to simulate ED patterns in the attached template matching notebook. All assumptions, models and calculations used for the simulation are described.

2.2.1 Bragg Equation in Real Space

Consider Figure 2.6. Plane waves are incident on two parallel planes with interplanar spacing d_{hkl}. Part of the wave is perfectly reflected at the top plane,

$$\theta_{in} = \theta_{out} = \theta.^{3}$$

Part of the wave passes through the upper plane and is reflected in the lower plane. However, this wave has travelled further and the two reflected waves will have a phase difference. In-phase arrival is determined by the path length difference whose geometry is shown in Figure 2.6. In order to get constructive interference, *Braggs condition* must hence be fulfilled,

$$2d_{hkl} \sin\theta = n\lambda \quad n \in \mathbb{Z}^{+}. \tag{2.10}$$

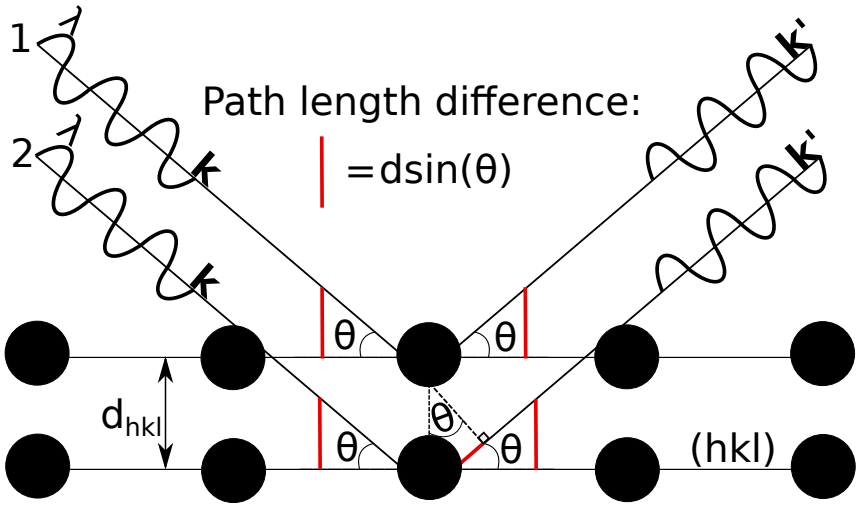

Figure 2.6: Geometric real space representation of Bragg's law. λ is the wavelength of the two incident plane waves with incoming wave vector $\boldsymbol{k}$ (outgoing wavevector $\boldsymbol{k}$'). θ is the incident and reflected angle. d_{hkl} is the distance between the two planes. Half the path-length difference is shown in red.

[3]Regarding the planes as semi-transparent mirrors (each plane reflects 10^{-5} to 10^{-3} of the incident wave) and applying Snells law[14, p. 26].

Braggs condition does not refer to the motif associated to every lattice point. The composition of the basis determines the relative intensity of the n diffraction orders. Equation 2.10 does not contain any information about the *intensity* of the diffracted wave, it only states the geometric condition for diffraction to occur.

2.2.2 Laue Condition and the Ewald Sphere Construction

The previous section established that diffraction occurs according to Equation 2.10, now a derivation of the equivalent diffraction condition in reciprocal space is shown. Each plane (hkl) is described by Equation 2.5 and an incoming plane wave has a wave vector k with magnitude

$$|\boldsymbol{k}| = \frac{1}{\lambda} \tag{2.11}$$

where

$$\lambda = \frac{h}{p} \tag{2.12}$$

is the *De Broglie wavelength*, which incorporates the wave-particle duality. h is Plancks constant and $\boldsymbol{p}$ is the momentum of the particle.

Consider Figure 2.6, notice how the outgoing wave vector $\boldsymbol{k'}$ may be written as $\boldsymbol{k'} = \boldsymbol{k} + \boldsymbol{g}$. This is equivalent to Braggs condition for first-order diffraction. By projecting $\boldsymbol{k'}$ onto $\boldsymbol{g}$ one easily confirm the geometrical proof:

$$\begin{aligned}
\boldsymbol{k'} \cdot \boldsymbol{g} &= \boldsymbol{k} \cdot \boldsymbol{g} + |g|^2 \\
|\boldsymbol{k}||\boldsymbol{g}| \sin\theta &= -|\boldsymbol{k}||\boldsymbol{g}| \sin\theta + |\boldsymbol{g}|^2 \\
\frac{\sin\theta}{\lambda} &= -\frac{\sin\theta}{\lambda} + \frac{1}{d_{hkl}} \\
2d_{hkl} \sin\theta &= \lambda.
\end{aligned}$$

Where we in the second step used the *elastic scattering condition*, $\boldsymbol{k'} = \boldsymbol{k}$.

By defining the *scattering vector* $\boldsymbol{k'} - \boldsymbol{k} = \Delta\boldsymbol{k}$, we arrive at the diffraction condition in reciprocal space known as the *Laue condition*,

$$\Delta\boldsymbol{k} = \boldsymbol{g}. \tag{2.13}$$

Equation 2.13 can be decomposed into three *Laue equations* by projection onto the three reciprocal basis vectors Equation 2.6,

$$\boldsymbol{a_1^*} \cdot \Delta\boldsymbol{k} = 2\pi h \tag{2.14}$$
$$\boldsymbol{a_2^*} \cdot \Delta\boldsymbol{k} = 2\pi k \tag{2.15}$$
$$\boldsymbol{a_3^*} \cdot \Delta\boldsymbol{k} = 2\pi l, \tag{2.16}$$

where h,k and l are the Miller indices.

This gives rise to a geometrical construction known as the *Ewald Sphere*, which is depicted in Figure 2.7. First draw the reciprocal lattice with origin $\boldsymbol{O}$. A plane wave is incident on $\boldsymbol{O}$, so $\boldsymbol{k}$ is drawn with its endpoint coinciding with $\boldsymbol{O}$. The starting point of $\boldsymbol{k}$ is the center of the Ewald sphere, and the radius of the sphere is only dependent on the wavelength of the incoming wave, in accordance with Equation 2.11. Only reciprocal lattice points that touches the sphere will satisfy the Laue condition, and may give diffracted waves with wave vectors $\boldsymbol{k} + \boldsymbol{g}$. Note that the radius of the Ewald sphere typically is two to three orders of magnitude less than the the typical length of $\boldsymbol{g}$ meaning that near the origin the Ewald sphere is almost planar.

As the calculated arc is planar, we pick up many points in one layer of the reciprocal lattice. This layer is called the Zeroth-order Laue Zone (ZOLZ), and will always contain the origin $\boldsymbol{O}$. However, if the collection angle is large, we may observe points that intersect in the other layers. These n observed layers will produce outer rings known as Higher-order Laue Zone (HOLZ). If we observe the first layer, then $n = 1$ and this layer is named First-order Laue Zone (FOLZ), and will produce FOLZ rings in the diffraction pattern.

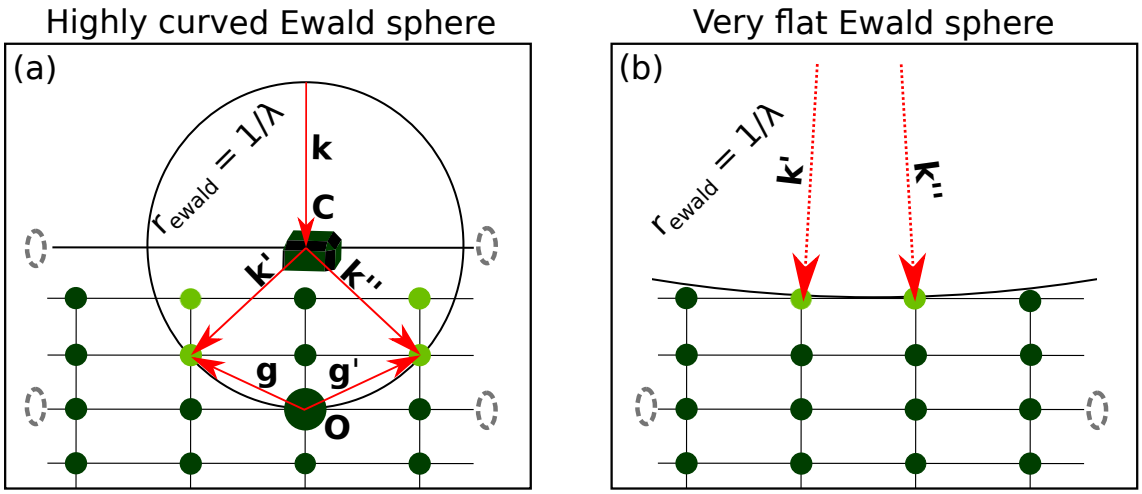

Figure 2.7: Ewald sphere construction. (a): Origin $\boldsymbol{O}$, center $\boldsymbol{C}$ and incoming wave $\boldsymbol{k}$ with wavelength λ. Two reciprocal lattice points coincide with the Ewald sphere, with radius $r_{ewald} = 1/\lambda$, and thus satisfy the Laue condition. These create the two diffracted beams in directions $\boldsymbol{k'}$ and $\boldsymbol{k''}$. By tilting the sample, two more reciprocal lattice points will hit the Ewald sphere, and satisfy the Laue condition. All four points are colored in bright green. The tilting of the sample is illustrated by the two circles over and under $\boldsymbol{O}$ and $\boldsymbol{C}$. (b): When the Ewald sphere is flat, fewer reciprocal lattice points will hit the Ewald sphere and thus satisfy the Laue condition. SPED aims to rectify this by a precession of the incident beam. Detailed description about SPED is found in section 2.4.

.

In diffraction experiments, there are a few ways one may sample more of reciprocal space. A translation of the Ewald sphere through the reciprocal lattice is achieved by changing the incident beam direction and keeping the sample static. Similarly, the sample may be tilted in all directions, which corresponds to translating the reciprocal lattice through the Ewald sphere. One may also change the wavelength of the incoming beam, in order to get more or less diffraction by increasing/decreasing the radius of the Ewald sphere. These options are further discussed in section 2.3

If the reciprocal lattice points are mathematical points then only a few spots will fulfill the Laue conditions. However, as the sample in real space is small, there are only a smaller number of repetitions. This will result in that the reciprocal lattice points are extended in that direction. The Laue condition is fulfilled if this so-called relrod intersects the Ewald sphere.[5]

There will be additional reflections visible in each Laue zone due to the finite value of the excitation error s_g. s_g is the deviation from a Bragg condition for a certain reflection g. The excitation error is defined as the distance from the reciprocal lattice point g to a point on the Ewald sphere measured along the vertical direction to the upper surface of the specimen. s_g is inversely dependent on thickness of sample and varies with $\sin^2$.

2.2.3 Quantum Mechanical Approach

We now incorporate the wave-particle duality of quantum mechanics in order to deduce a few important properties.[4]

First define the Hamiltonian operator,

$$\hat{H} = \hat{T} + \hat{V}, \tag{2.17}$$

where $\hat{V} = V(\boldsymbol{r}, t)$ is the potential energy operator and

$$\hat{T} = \frac{\hat{\boldsymbol{p}} \cdot \hat{\boldsymbol{p}}}{2m} = \frac{\hat{p}^2}{2m} = -\frac{\hbar^2}{2m}\nabla^2 \tag{2.18}$$

is the kinetic energy operator in which m is the mass of the particle, the dot denoting the dot product, and

$$\hat{p} = -i\hbar\nabla \tag{2.19}$$

is the momentum operator.

We want an expression for the wave function, $\Psi(\boldsymbol{r})$ of the electron beam. The eigenvalues $\boldsymbol{p}$ corresponding to the eigenfunctions $|\Psi\rangle$ are determined by

$$\hat{p}\,|\Psi\rangle = -i\hbar\nabla\Psi(\boldsymbol{r}) = \boldsymbol{p}\Psi. \tag{2.20}$$

[4]This subsection follows the deduction from 'Introduction to Conventional Transmission Electron Microscopy' by Marc De Graef[5] quite closely.

Which is a trivial first order differential equation with solutions

$$\Psi(\boldsymbol{r}) = Ce^{\frac{1}{h}\boldsymbol{p}\cdot\boldsymbol{r}}, \tag{2.21}$$

where C is a constant. Using Equation 2.12, one finally attains the wave function of a particle in coordinate space, written as a linear combination of the momentum eigenfunctions(that are all plane waves),

$$\Psi(r) = \sum_k c_k e^{2\pi i\boldsymbol{k}\cdot\boldsymbol{r}}. \tag{2.22}$$

Where C and $e^{2\pi}$ has been absorbed by the constant c_k.

We now have the tools necessary to calculate some important properties. First, we start with the total scattering amplitude F.

According to Equation 2.22 the incoming wave $\boldsymbol{k}$ and the outgoing wave $\boldsymbol{k'}$, see Figure 2.6, has a phase difference of $e^{i(\boldsymbol{k}-\boldsymbol{k'})\cdot r}$. The amplitude of an electron being scattered to a particular wave vector is proportional to the the electron number density, $n(\boldsymbol{r})$. The *scattering amplitude*, $f^e(\Delta\boldsymbol{k})$ of an electron describes how the momentum of the electron changes upon elastic scattering. The total scattering amplitude, $f_{tot}(\boldsymbol{g})$ from N unit cells is then attained by summing up the contribution over the whole crystal V, given that the Laue condition $\Delta\boldsymbol{k} = \boldsymbol{g}$ is fulfilled

$$f_{tot} = N\int^V n(\boldsymbol{r})e^{i\boldsymbol{g}\cdot r}dV = NF_{hkl}, \tag{2.23}$$

where the *structure factor* F_{hkl} is introduced.

The electron number density can be rewritten as a sum of over N,

$$n(\boldsymbol{r}) = \sum_{j=1}^{m} n_j(\boldsymbol{r} - \boldsymbol{r_j}), \tag{2.24}$$

By insertion Equation 2.24 into Equation 2.23, F_{hkl} can be rewritten as

$$F_{hkl} = \sum_{j=1}^{N} f_j e^{-i\boldsymbol{g}\boldsymbol{r}_j} \tag{2.25}$$

$$F_{hkl} = \sum_{j=1}^{N} f_j e^{-2\pi(hx_j+ky_j+lz_j)} \tag{2.26}$$

Where the *atomic form factor*, f_j, is introduced, and Equation 2.5 is inserted for $\boldsymbol{g}$.

Finally, the intensity of each reflection, $\boldsymbol{g}$, is given in the *kinematic* approximation as the modulus square of the structure factor.

$$I_{hkl} \propto F_{hkl}F^*_{hkl} \tag{2.27}$$

2.2.4 Converting from Real Space to Reciprocal Space

As a consequence of Equation 2.12, we find that the reciprocal space is identical to momentum space, apart from the scaling factor of $\hbar$. Hence, we want to express $\Psi = \Psi(\boldsymbol{k})$. The contribution of $\boldsymbol{k}$ to $\Psi(\boldsymbol{r})$ is given by the projection of $\Psi(r)$ onto the momentum eigenfunction corresponding to $\boldsymbol{k}$,

$$\Psi(\boldsymbol{k}) = \mathcal{F}|\Psi(\boldsymbol{r})| \equiv \iiint \Psi(\boldsymbol{r}e^{-2\pi i\boldsymbol{k}\cdot\boldsymbol{r}})d\boldsymbol{r}. \tag{2.28}$$

Where $\mathcal{F}$ represents the discrete Fourier transform. This transformation can be inversed by an *inverse Fourier Transform*,

$$\Psi(\boldsymbol{k}) = \mathcal{F}^{-1}|\Psi(\boldsymbol{k})| \equiv \iiint \Psi(\boldsymbol{k}e^{2\pi i\boldsymbol{k}\cdot\boldsymbol{r}})d\boldsymbol{k}. \tag{2.29}$$

Equation 2.28 and Equation 2.29 are tools for converting between real space representations and reciprocal space representations.[5]

2.3 Transmission Electron Microscopy

TEM is a microscopy technique in which a beam of electrons is transmitted through a specimen to form an image. A TEM consists of five main stages: The *electron gun stage*, the *illumination stage*, the *objective lens stage*, the *magnification stage* and lastly the *observation stage*. The electron path is following on the Optical Axis (OA). Please refer to Figure 2.8, which outlies the *TEM column* schematically, each aforementioned stage is labelled (a)-(e).

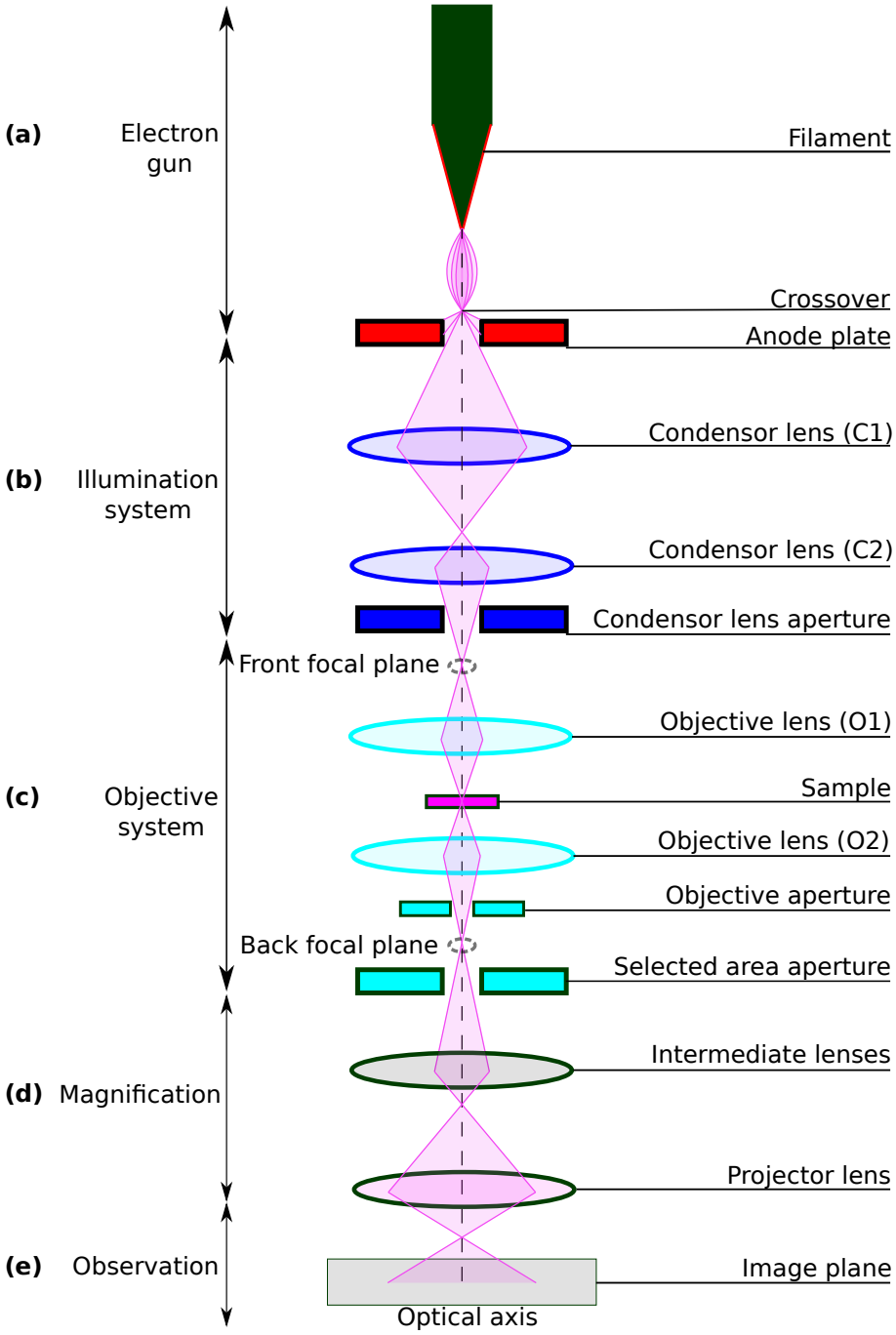

Figure 2.8: Schematic overview of a TEM column. The electron travels downwards from the the electron gun to the detector through five stages labelled (a)-(e).

Starting at the source (a), at the top of the TEM column the electron gun is located. A good electron gun provides a steady stream of electrons with constant kinetic energy - a *monochromatic* electron beam. To achieve this a high voltage system is connected to the electron gun in order to create an *accelerating voltage* between the filament and the anode plate. Accelerating voltages of 100–300 kV are common or a good compromise for the majority of TEM specimen, avoiding the expense of high-voltage microscopy but providing the possibility of atomic resolution.[16] In order to reduce lens aberration effects, it is best to have electrons emanating from a point source and a small angle, α, between the trajectory of the electron and the optical path. α is also known as the gun divergence semi-angle.[5]

The illumination system (b) provides incident electrons and controls their intensity and angular convergence on the sample. After the electrons moves past the crossover, they pass through the anode at relatively high velocity. The electron beam then moves into a condenser lens system which provides a demagnification of the crossover and thus producing a better point source. This demagnification effect can be controlled by alterations to C1, and is often called controlling the "spot size". By varying the strength of C2, one may choose whether converge the beam to, diverge the beam to a cone, or get parallel rays on the sample. To improve the beam divergence, and remove the worst aberration effects from the condenser lenses, an aperture is used in order to eliminate off-axis rays. The illumination, or convergence angle, is determined by this aperture and C2.[12]

After the condenser system the electron beam travels through the objective lens system (c). The two objective lenses form a diffraction pattern in the back focal plane after the dispersing the electrons emerging from the sample and recombining them to form an image further down in the column. An objective aperture may be used to eliminate high-angle scattered images to select specific part of the total transmitted beam, for example to select only the not-scattered or direct beam and construct a bright-field image.

The Selected Area (SA) method in TEM for diffraction is performed by focusing the *intermediate lens* on the back focal plane of the objective lens. The intermediate aperture is positioned in the image plane of the objective lens in order to have the diffraction pattern contributing to the final by selecting a limited area on the sample. This aperture is needed for diffraction patterns when using large parallel beams. As parallel beams are focused on focal length, this gives a spotty pattern.

To switch between images, either as Bright Field-TEM or as diffraction patterns, the intermediate lens system is used. The intermediate lens system (d) allows for two different imaging modes, image mode and diffraction mode. The two modes are visualized in Figure 2.9. In order to change modes, the intermediate lens strength is altered while the objective aperture and the SA aperture is engaged or disengaged. Image mode allows a real space visualization of the specimen, and is achieved by adjusting the TEM column so that the intermediate lenses make the object plane coincide with the image plane. Diffraction mode however, is achieved when the intermediate lenses' object plane is the back focal plane of the object plane.

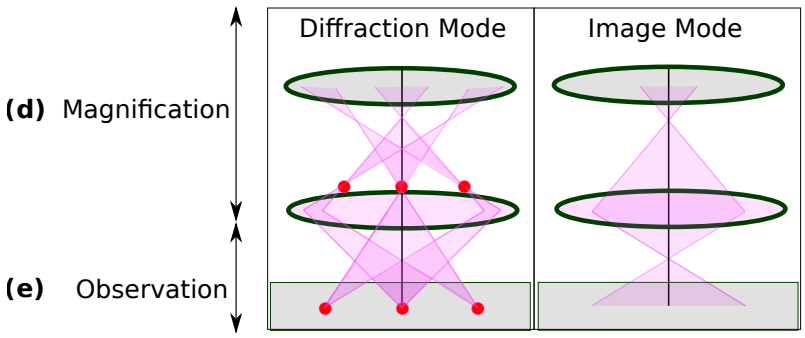

Figure 2.9: Visualization of diffraction mode and image mode for stages (d) and (e). By altering the intermediate lens strength while the objective aperture is engaged or disengaged one may switch between the two modes. Diffraction mode maps the sample to a reciprocal representation, where the observed spots represent the angular distribution of intensity. Image mode allows for a (magnified) real space visualization of the specimen.

The diffraction pattern that is seen in diffraction mode is the angular distribution of intensity. Spots are observed because the specimen is crystalline, and so it acts as a diffraction grating for the electrons, which really behave as waves. The projector lens projects all electrons with the same incoming angle to the same spot on the detecting sensor, as shown in Figure 2.9. For an in-depth explanation of diffraction, see section 2.2.

The image, whether from image mode or diffraction mode, is projected on the detector (e), which is a Charge Coupled Device (CCD) camera. A CCD camera is an integrated circuit etched onto a silicon surface forming light sensitive elements. For electron beam detection, electrons are converted into light by a fluorescent material(or a YAG crystal). When the CCD camera is irradiated with this light one may see the resultant image in real-time. Having a high field of view, frame rate, fill factor and resolution are especially important when choosing a CCD detector. [17]

The sample is held in a specimen holder. Two of the most commonly used holders are the single tilt holder, which allows a tilt around the axis of the holder, and the double tilt holder, which allows in-plane and out-of-plane tilting. Tilt-rotate holders allows both tilting and rotation of the sample. These holders allow to orient the sample relative to the electron beam so that a symmetric pattern is formed from a low index direction.[18, Chapter 10]

Another important part of a TEM is its vacuum system. In order to increase the mean free path of the electron, a TEM is evacuated to low pressures. This nullifies arcing between the cathode and ground, as the collision frequency of electrons decreases with longer mean free paths. Furthermore, poor vacuum may cause deposition of gas onto the sample. For regular TEMs the pressure is decreased to 10^{-4} Pa, while high-voltage TEMs require ultra-high vacuums ranging from 10^{-7} to 10^{-9} Pa.[19]

2.4 Scanning Precession Electron Diffraction

Precession Electron Diffraction (PED) is accomplished by utilizing the standard instrument configuration of a modern TEM. Instead of using parallel beams to get sharp diffraction maxima, a small probe is used to converge the beam onto a chosen part of the specimen. By double conical rocking (precession) of a tilted incident electron beam around the central axis of the microscope, a PED pattern is formed by integration over a collection of diffraction conditions determined by the *precession angle*, ϕ. ϕ usually lies in the range of 0-3°. For most SPED analysis 0.5-1° is used, as a higher precession angle greatly deteriorates the spatial resolution. PED was first described in detail by Vincent and Midgley in 1994. [20, 21]

The intensity at each point can be collected and combined in order to create an image. PED suppresses the intensity variation due to dynamical scattering, thickness variations and bending, which leads to an easier interpretation of the diffraction patterns. One obtains a quasi-kinematical diffraction pattern that is more suitable as input into direct methods algorithms to determine crystal structures. The diffraction data is stored as four-dimensional data arrays, two real and two reciprocal dimensions (4D-PED). [22, 23]

The diffraction pattern consists of an Laue circle with a radius equal to ϕ. The Laue circle that is excited extends far into reciprocal space. After integration, many more reflections from ZOLZ are present and their relative intensities are more kinematical in nature. Likewise, additional HOLZ reflections will be present which may provide information about three-dimensional reciprocal space, even from a two-dimensional PED pattern. This makes it easier to determine the space group and orientations, but the recording space is often limited to ZOLZ.

During precession $\boldsymbol{k}$ changes. When the ZA is aligned with the OA, the zero-layer expands as a function of ϕ from a point to a circular area and the HOLZ reflection rings become annuli. In reciprocal space, this can visualized as a change in the radius of the Ewald sphere, while keeping the origin static, as seen in Figure 2.10. When there, the Laue zones may overlap. Both the differences in periodicities and the shifts between the ZOLZ and HOLZ are easy to detect, which makes PED a good tool to identify the Bravais lattice, and also the absence of glide planes.[20]

Since the measurement is an average over many incident beam directions, due to differing ϕ, the pattern is less sensitive to slight misorientation of the ZA from the OA of the microscope. Hence the resulting summed PED patterns will display the ZA symmetry more clearly. This provides a benefit of more robust data collection. The integration also reduces contributions from inelastic scattering effects such as Kikuchi lines.

Precession extends the thickness of the Ewald sphere, see Figure 2.10. The extension leads to more relrods cutting the sphere and thus more reciprocal lattice points satisfying the Laue condition. The relrods are still equally long as in non-precessed experiments. The effective excitation error s_g in precession experiments are thus longer than 1/length.

By scanning the electron beam across the sample with a small step size, usually in the order of nm, PED patterns from the whole sample can be acquired - this method is called SPED. The scan step size and the size of the probe determine the spatial resolution. This allows statistical approaches to phase determination and also orientation mapping.

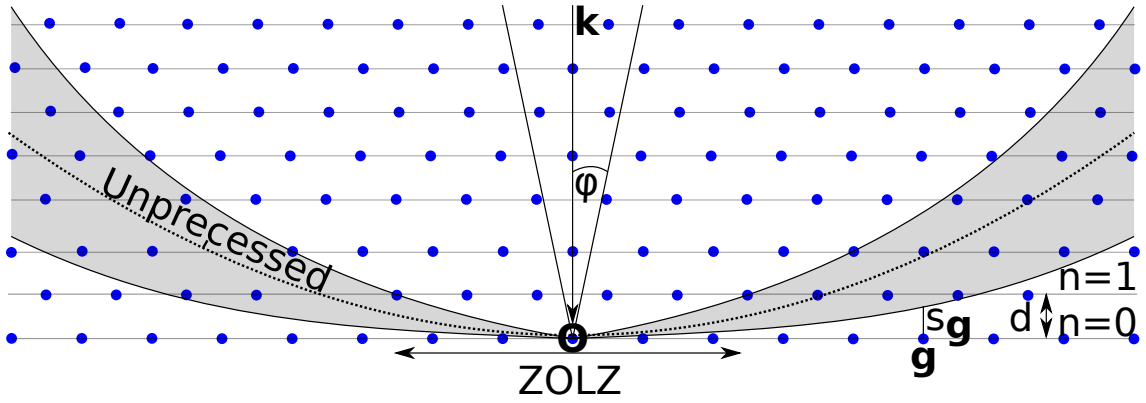

Figure 2.10: Schematic illustration (not on scale, sphere is much flatter) of the precession geometry for intersections of the Ewald Sphere and reciprocal lattice layers. As the direction of the $\boldsymbol{k}$ changes, the radius of the Ewald sphere moves and the intersections change. A beam is incident with the ZA at angle ϕ, $\boldsymbol{O}$ is the (static) origin, D is the distance between the reciprocal layers, $s_{\boldsymbol{g}}$ is the excitation error for the $\boldsymbol{g}$ reflection. The dotted line represents the unprecessed Ewald sphere from $\boldsymbol{k}$. Figure inspired by [20].

2.5 Aluminium System

2.5.1 Precipitation

For technical alloys, control over the the formation of small secondary phases, precipitates, is crucial. From an engineering viewpoint, dispersing fine precipitate particles over the matrix at high density is a common technique for improving the strength of metals and alloys. *Precipitates* form during an aging process at an elevated temperature, as long as the system has a decreasing solid solubility with decreasing temperature. Unlike ordinary tempering, alloys must be kept at a higher temperature for several hours for precipitation to take place, this is called *aging* the alloy. Not all precipitates have the same size, a typical precipitate has a cross section of a few nm^2 and a length of a few nm. The aging process can also produce microstructures that contains more than just one precipitate.

Hard, minority-phase particles inhibit the movement of dislocations and since dislocations often are the dominant carriers of plasticity, this serves to harden the material. If the strengthening is due to the presence of coherent precipitates which are sheared by dislocations, then this mechanism is called *precipitate hardening*.[4] The theory that the shear modulus is the driving force of the strengthening is the traditional theory, developed in 1950s-1960s. However, recent discoveries gives rise to another mechanism entirely; when the slip plane of dislocations in precipitates is not parallel to that in the matrix, dislocations are unable to cut through the precipitates, resulting in the aforementioned hardening, regardless of the shear modulus.[24]

2.5.2 Al-Mg-Si(-Cu) (6xxx series)

The Al(-Mg-Si) (6xxx series) alloys form one of the main groups of *age-hardening* Al alloys. An alloying element element always strengthens the solvent metal. In dilute solutions, as is the case with the Al-Mg-Si(-Cu), the strengthening is usually proportional to the solvent concentration. However for ternary alloys, like Al-Mg-Si(-Cu), the solution strengthening effect is greater than predicted when the elements work in combination.[4]. In this work the (6082) Al-Mg-Si(-Cu) alloy will be studied.

During aging, this alloy precipitates. The precipitation has been studied and a summarized version of each phases' composition, space group(Hermann-Mauguin notation) and lattice parameters is shown in Table 2.2. Some of the phases are more common than the others, and is thus regarded as more important for the current work. This thesis analyzes β', β'' and Q'.

All of the regarded phases, except β' has *coherent interfaces* with the Al matrix. A coherent interface is formed when the two crystals or part of the crystal has a good 'match' and the two lattices are continuous across the interface. Figure 2.11 shows the 6 most important phases in the Al-Mg-Si(-Cu) system along with their coherent interface with the [001] Al plane. It is energetically favourable for the phase to align according to the Orientation Relationship (OR), and it is improbable that it will align itself in other ways. β' does not have any coherent interfaces, however, it aligns itself according to certain OR, this due to β' having a intermediate phase between itself and the Al-matrix.[25]

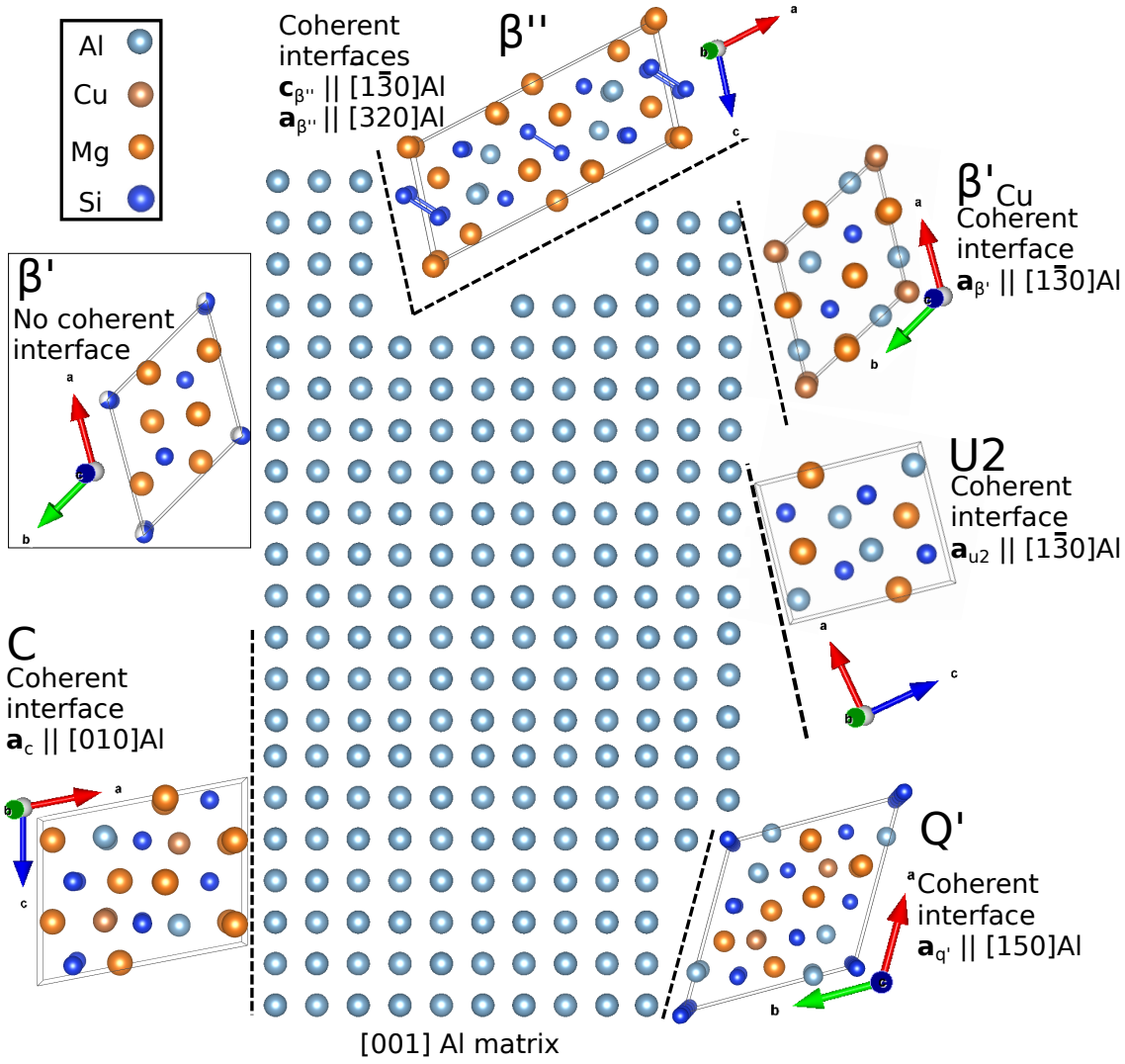

Figure 2.11: Schematic representation of six main precipitates in the Al 6xxx series. Unit cell for β'', β', β'_{Cu}, $U2$, Q' and C oriented in order to have coherent interfaces with the [001] Al ZA according to their OR. Inspired by Sunde et Al [26].

Table 2.2: Table over all phases known to occur in the Al-Mg-Si(-Cu) system. Their respective composition, space group and lattice parameters are listed. This is all the information needed in order to construct a CIF.

Phase	Composition	Space Group	Lattice Parameters [Å]	References
β'	$Mg_6Si_{3,33}$	$P6_3/m$	$a = 7.15$, $b = 7.15$ $c = 4.05$, $\gamma = 120^\circ$	[25]
β''	$Al_2Mg_5Si_4$	C2/m	$a = 15.16$, $b = 4.05$, $\beta = 105.3^\circ$, c = 6.74	[27, 28]
β'_{Cu}	$Al_3Mg_3Si_2Cu$	$P\bar{6}2m$	$a = 6.90$, $b = 6.90$, $\beta = 60^\circ$, c = 4.05	[29]
Q'	$Al_xMg_{12-x}Si_7Cu_2$[b]	P6	$a = 10.32$, $b = 10.32$, $c = 4.05$, $\gamma = 120^\circ$	[27, 30]
C	$AlMg_4Si_3Cu$	$P2_1$	$a = 10.32$, $b = 4.05$, $\beta = 100.9^\circ$, c =8.10	[31]
U2	AlMgSi	Pnma	$a = 6.75$, $b = 4.05$, $c = 7.94$	[32]
Q	$Al_xMg_{12-x}Si_7Cu_2$[b]	P6	a = 10.39, $b = 10.39$, $c = 4.05$, $\gamma = 120^\circ$	[27, 30]
S	Varies	Varies	Varies	[33]
L	Varies	Varies	$a = 10.39$, $b = 4.05$, $\beta = 100.9^\circ$, $c = 8.10$	

2.6 Data Processing

2.6.1 Template Matching

Template matching is a technique in digital image processing for finding small parts of an image that match a template image. For the purposes of this work, template matching has been tailored to compare experimental diffraction patterns with a database of simulated diffraction patterns with known phase and orientation.[34]

As explained in section 2.4, each pixel in SPED image contains a 2D reciprocal image. Template matching compares this pattern with a template pattern in a template bank. The comparison can be done in many ways, the most common one is *pixel by pixel* comparison but other comparison methods are also used, see subsection 2.6.2. By ranking the best matches for each pattern the best orientation and best phase can produced. This work looks at a small number of candidate phases, see Figure 2.11, and a small number of possible orientations.

The *phase map* is a visual representation, often using different colors for different phases that shows the spatial location of each precipitate that has been formed on the specimen. Information such as, precipitate occurrence, precipitate clustering, and phase-transitions may be investigated using a phase map. [35]

As described in section 2.4, PED gives diffraction patterns that are closer to the kinematic model. This fact gives us the theoretical grounds to calculate the scattering intensity at all reciprocal lattice points according to equation Equation 2.27. This intensity calculations is done for each reciprocal lattice point which are used to build a database of diffraction patterns. Each entry, i, in the database contains two spatial coordinates,x_i, x_j, and the corresponding intensity function $I(x_i, y_i)$ determined by Equation 2.27.

For every database entry T_i, a correlation index Q is created (here Normalized Cross Correlation (NCC) is used, other correlation functions are discussed in the following subsection),

$$Q(i,\phi) = \frac{\sum_{j=1}^{m} I(x_j, y_j) T_i(x_j, y_j, \phi)}{\sqrt{\sum_{j=1}^{m} I^2(x_j, y_j \phi)} \sqrt{\sum_{j=1}^{m} T_i^2(x_j, y_j, \phi)}} \tag{2.30}$$

Where $\phi \in [0, 2\pi\rangle$ is a constant in-plane rotation.

Q is calculated for every experimental diffraction pattern for every template library entry and the best match is stored.

The reliability score is calculated by,

$$R = 100 \left(1 - \frac{Q_2}{Q_1}\right), \tag{2.31}$$

and is a measure of the difference between the best, Q_1 and second best, Q_2 match.

In order to sample enough orientations to get a good (and reliable) correlation score, the code utilizes the symmetry order of the precipitates, see section 2.1.1. Instead of getting orientations from the whole SP, we instead sample from the ST for each phase. This reduces the template library, which reduces the number of computations required and hence allows for a finer orientation sampling using less time.

2.6.2 Correlation Functions

Template matching implements a set of methods for finding the image regions that are similar to the given template. This *similarity* can be calculated in several ways with the use of different *correlation functions*. There is no exact metric that defines similarity, but there exists several different mathematical methods which attempts to correlate a template library with an image. In modern image recognition, the most common metrics for determining similarity are so called *pixel by pixel* correlation functions.

Pixel by pixel compares each pixel in the template image with the corresponding pixel in the image. Usually the image is converted to a color gradient map that normalizes the value of a image attribute, i.e intensity, to the numerical range [0, 1]. For our case, each pixel represents an amount of light; that is, the pixel carries only intensity information. The term *grey scale image* is often used to describe the transformed image. White has a value of 1 and black has a value of 0 when normalized. I.e when using 32 byte data, there is 256 different possible grey levels (bits). This pixel by pixel comparison method is schematically shown in Figure 2.12

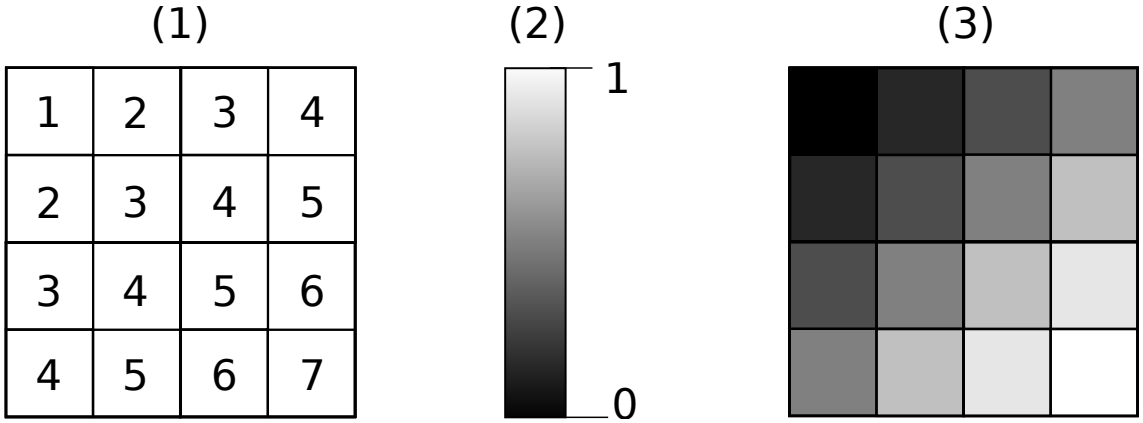

Figure 2.12: Schematic explanation of grey scale images. (1): An image is reduced to a matrix of intensity values. The elements in the matrix corresponds to the pixels in the image. (2): The intensities are normalized to the numerical range [0, 1] and mapped to a unique color on the grey scale. (3): Resulting grey-scale image.

Humans recognize a multitude of features in images with almost no effort, the image of the objects may vary somewhat in different view points, in many different sizes and scales or even when they are translated or rotated. When analysing TEM images of different samples, the view point is often fixed as the TEM camera is located directly perpendicular to the sample, but the camera length and magnification may be altered by the TEM operator. Different samples will have different thickness, curvature and other physical traits like strain that may translate and rotate the reciprocal image. Humans may even recognise the features even though it is partially obstructed by a dust particle on the camera lens. This task is still a challenge for computer vision systems. In this work pixel by pixel approaches is analyzed, but the correlation can be done in different ways.

Sum of absolute differences and sum of squared differences

The Sum of Absolute Differences (SAD), see Equation 2.32, is in digital image processing one of the simplest measures of similarity. By taking the absolute difference between each pixel at position (x_j, y_j) in the analyzed image(I) and the corresponding pixel in the template image T and then summing these differences up, one obtains the L^1 norm.

$$Q(i,\phi) = \frac{\sum_{j=1}^{m} |T(x_j, y_j) - I(x_j, y_j, \phi)|}{\sqrt{\sum_{j=1}^{m} I^2(x_j, y_j, \phi) \cdot \sum_{j=1}^{m} T_i^2(x_j, y_j, \phi)}} \tag{2.32}$$

Where $\phi \in [0, 2\pi\rangle$ is a constant in-plane rotation, and the result is normalized to the numerical range [0,1] where 0 represents the best possible match.

SAD is intuitively the simplest, and computationally the least expensive of all the matching procedures. It is easily parallelizable since it analyzes each pixel separately. A closely related correlation metric is the Sum of Squared Differences (SSD), see Equation 2.33. If there is a constant offset between the pixel intensities in the two images SAD and SSD will yield bad results. A schematic comparison is given in Figure 2.13.[36]

$$Q(i,\phi) = \frac{\sum_{j=1}^{m} (T(x_j, y_j) - I(x_j, y_j, \phi))^2}{\sqrt{\sum_{j=1}^{m} I^2(x_j, y_j, \phi) \cdot \sum_{j=1}^{m} T_i^2(x_j, y_j, \phi)}} \tag{2.33}$$

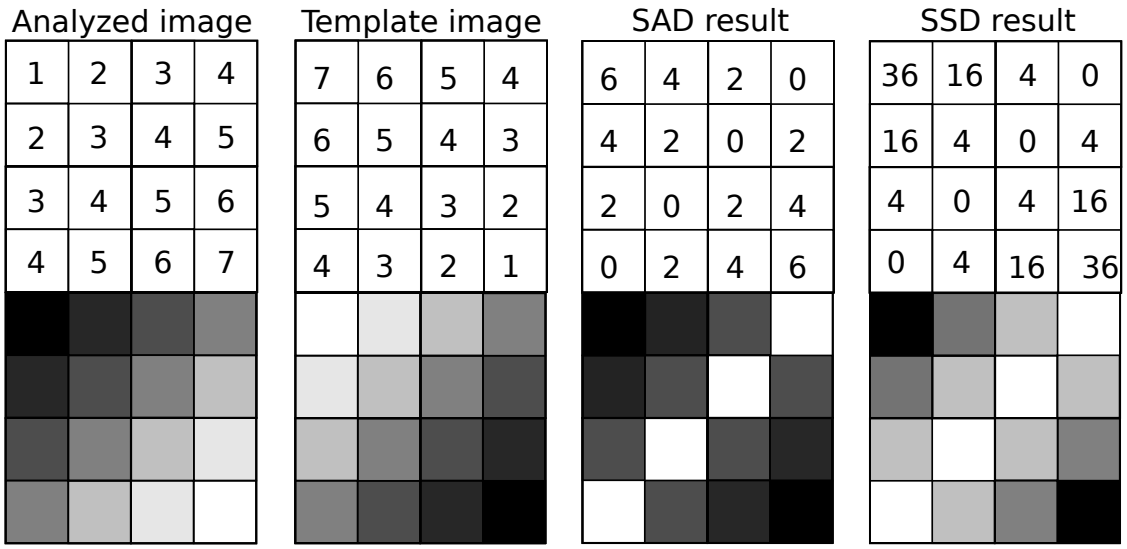

Figure 2.13: Schematic comparison of SAD and SSD based template matching. The analyzed image is correlated with the template image using SAD and SSD methods without doing the normalization. Observe that the template image and the analyzed image is mirrors of each other, this leads to a perfect match along the diagonal and extremely bad match near the other corners.

Cross correlation and zero mean cross correlation

A common problem that must be circumvented occur when the pixel intensities in one image are equal to the intensities in the other image multiplied with a gain factor. The brightness of the image will then directly effect the correlation score. To deal with problems that may arise with SAD and SSD, more sophisticated pixel by pixel correlation functions are introduced.

NCC, Equation 2.34, deals with the difference in brightness problem by dividing on the variance for each window. The normalized quantity $Q(i, \phi)$ will vary between -1 and 1. A value of $Q(i, \phi) = 1$ indicates that the two images have the exact same shape (the intensities may be different) while a value of $Q(i, \phi) = -1$ indicates that they have they have the same shape, but have opposite signs. Lastly, a value of $Q(i, \phi) = 0$ indicates that they are completely uncorrelated. In practice when applying this normalization to real signals a correlation coefficient of 0.7 or 0.8 indicates a pretty good match.[37]

$$Q(i, \phi) = \frac{\sum_{j=1}^{m} I(x_j, y_j) T_i(x_j, y_j, \phi)}{\sqrt{\sum_{j=1}^{m} I^2(x_j, y_j \phi)} \sqrt{\sum_{j=1}^{m} T_i^2(x_j, y_j, \phi)}} \tag{2.34}$$

Zero Mean Normalized Cross Correlation (ZNCC), Equation 2.35, is an extension of NCC and deals with the offset problem subtracting the average from each pixel value. This means that the template image and the analyzed image not necessarily needs to be precisely centered to get a good correlation score. However, this advantage comes with a great cost on computational resources.[37]

$$Q(i,\phi) = \frac{\sum_{j=1}^{m} P(x_j,y_j)T(x_j,y_j) - \bar{P}(x_j,y_j)\bar{T}(x_j,y_j)}{\sqrt{\sum_{j=1}^{m}(T(x_j,y_j) - \bar{T}(x_j,y_j))^2 + \sum_{Notj}\bar{T}(x_j,y_j)}} \tag{2.35}$$

Chapter 3

Method

This chapter is divided into three sections. First, section 3.1 describes how the TEM sample has been prepared and the SPED data acquired. Second, section 3.2 describes the developed data processing workflow for both the experimental data set and for the simulated model. Third, section 3.3 describes the implementation of the Python code in detail.

A substantial amount of work has gone into creating a working model-based method for phase mapping the precipitates. The methods used has undergone numerous iterations and the final version is in itself a result of the work. As part of the development process, a series of contributions have been made to the open-source libraries DiffSims and pyXem, these are shown in Table A.1.

3.1 Material and TEM Sample Preparation

The material studied was the aforementioned Al-Mg-Si alloy (6082) with low Cu addition introduced in section 2.5. The nominal composition is shown in Table 3.1. The sample preparation is shown in the flow chart (Figure 3.1).

Table 3.1: The elemental nominal composition of the (6082) Al-Mg-Si(-Cu) alloy.

Element	Al	Si	Mg	Cu	Fe	Mn	Cr
at.%	bal.	.85	.8	.01	.12	.25	.08
wt.%	bal	.88	.72	.03	.24	.51	.16

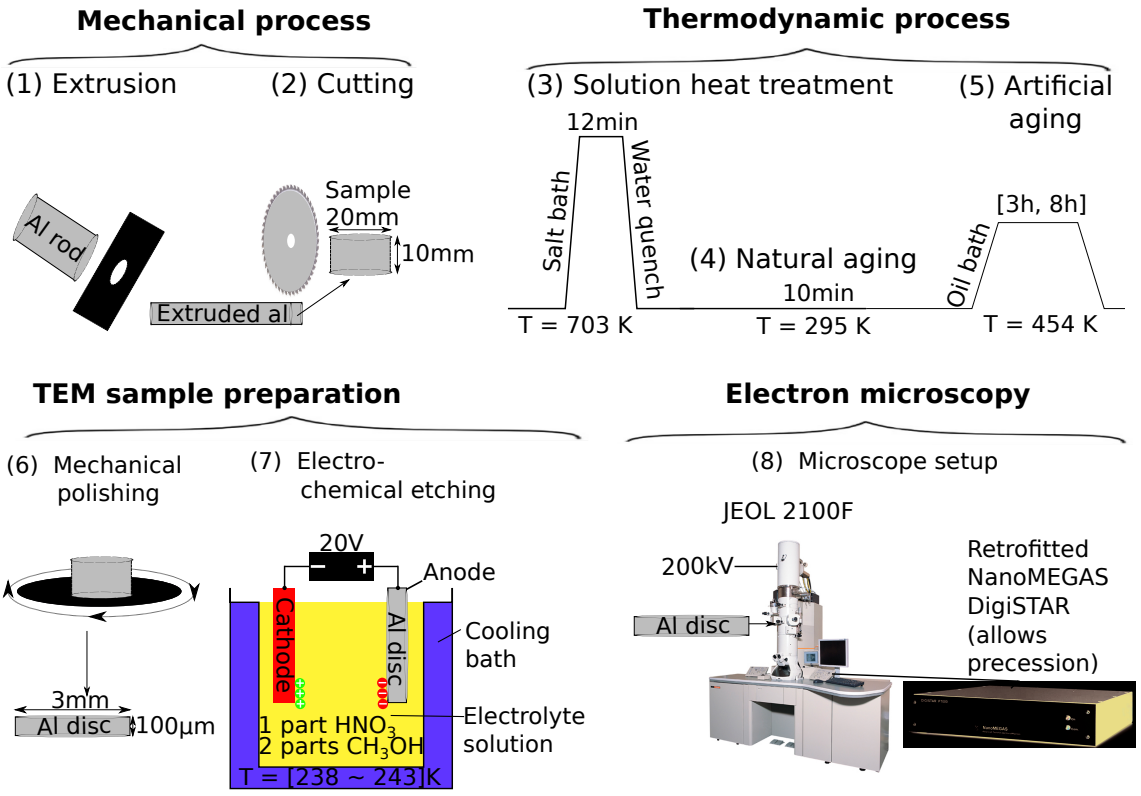

Figure 3.1: Sample preparation flow chart. (1)-(5): Description of the thermo-mechanical history of the sample. (6)-(8): The TEM sample preparation steps and the experimental data collection. Please refer to the associated body for details.

(1), (2): Neuman Aluminium in Raufoss performed the casting and extrusion[38]. Cast Al-Mg-Si-(Cu) was extruded into a long circular rod which was subsequently cut into a smaller more manageable size ready to undergo a thermo-dynamic process.

(3), (4), (5): The sample underwent a three-step thermo-dynamical process consisting of a 12 minute solution heat treatment at 703 K, subsequently followed water-quenched to room temperature for a natural aging process of 10 minutes. After the natural aging, the sample was artificially aged in an oil bath for 3 hours at 454 K to obtain peak hardness[6]. This concludes the heat treatment and the sample now had to be prepared for the TEM.

(6), (7): The sample was mechanically polished down to about 3 mm diameter and 100 µm thickness. A high precision is achieved by using a polishing clock, instead application of manual pressure. Following the polishing, the sample was electro-chemically etched at 20V in a electrolyte solution with one part HNO_3 and two parts CH_3OH. A cooling bath retained the temperature of the solution at between 238 K to 243 K. The sample was now ready to be inserted into the microscope.

(8): A JEOL 2100F microscope with acceleration voltage of 200 kV was used. In order to simultaneously scan and acquire diffraction patterns an external camera was mounted to capture the viewing screen of the microscope. This, in conjunction with a NanoMEGAS DigiSTAR retrofitted to the TEM allowed for the acquisition of precessed diffraction data. To reduce the risk of carbon contamination build up, Fischione 1020 Plasma Cleaner was applied to the sample before being inserted to the TEM.

3.2 Data Processing Workflow

In order to perform template matching between a physical, simulated model and an experimental SPED data set the data processing workflow diagram shown in Figure 3.2 has been developed. The workflow diagram illustrates that there are two branches: Experimental (left side) and simulation (right side).

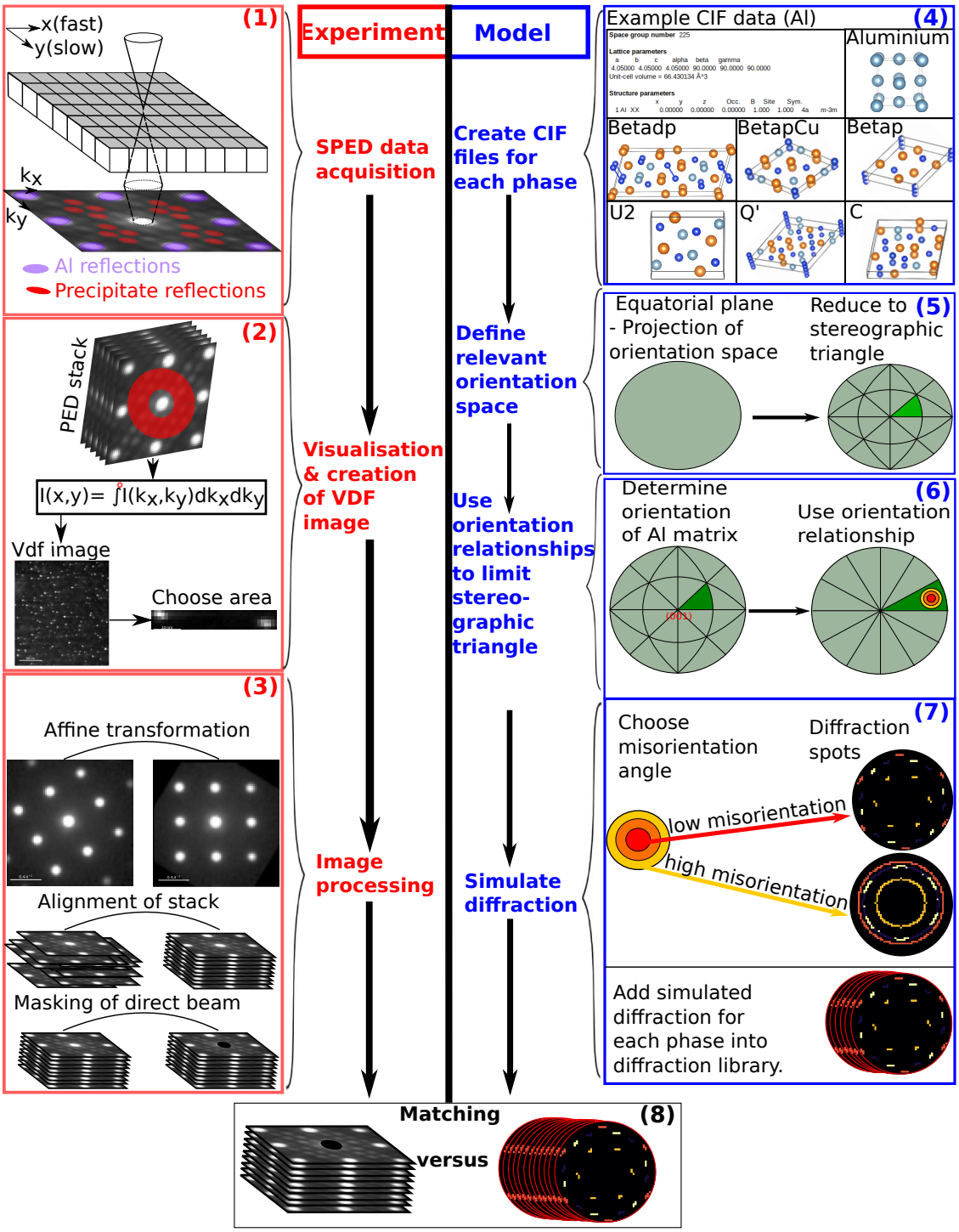

Figure 3.2: Method workflow diagram. (1)-(3): Illustration of the treatment of the experimental dataset. (4)-(7): Illustration of the creation of the simulated model. (8): Illustration of the matching step. The details are explained in the body.

3.2.1 Experimental Data Processing

This subsection discusses the experimental (left) branch of Figure 3.2.

(1): The SPED data, or more specifically, the HDF5 files, is acquired from the NanoMEGAS DigiSTAR. The obtained 4D SPED datasets, comprising a 2D PED pattern at each probe position (illustrated as cubes in (1)) of a 2D area scan, were analysed using the pyXem and Hyperspy Python libraries in addition to code written by the author.

(2): To identify and visualize the position of the precipitates, a map of the precipitate locations has to created. In order to create this map of precipitates, also known as Virtual Dark Field (VDF) images, an intensity $I(x, y)$, integration over an annulus A, is performed as per Equation 3.1. This annulus is defined from the edge of the direct beam to the edge of the underlying Al matrix reflections, illustrated in (2) as a red overlay on the PED pattern. At this point, a smaller area containing a few precipitates may be chosen in order to achieve faster computational speed. One may also choose to crop the reciprocal space - however be mindful not to crop enough to lose important phase reflection information. A rule of thumb is to use the underlying noise as a starting point. For the Al-Mg-Si-(Cu) dataset, enough relevant phase information is contained within the Al cubic frame seen in the purple Al reflections in (1).

$$I(x, y) = \int_A I(k_x, k_y) dk_x dk_y, \tag{3.1}$$

(3): Three forms of image processing have been applied to the experimental data set in order to get better matches with the simulated model. These three steps have been thoroughly tested and shown to be required to be able to phase map the different precipitates. All of the three image processing steps are lossless, meaning that no information is lost when performing them. A lossless approach is crucial to keep the procedure objective. In the present case only central part of patterns, (144 x 144)px mrad (just outside the 200Al reflections), is used.

The first image processing step is an in-plane rotation. An in-plane rotation is a form an affine transformation (linear mapping method that preserves points, straight lines and planes). This affine transformation is performed in order to attain a constant frame of reference for each PED pattern. This creates an rotational invariance between the PED pattern and the simulated model which removes one degree of freedom when later performing the matching.

The second image processing step is aligning the PED stack to compensate for any tilt-shift impurity. This is a crucial step, which if done incorrectly will make any form of pixel by pixel comparison method (as described in section 2.6 yield wrong results. When done correctly, this alignment opens up for the possibility for pixel by pixel comparison. This step must always be done after the in-plane rotation, as a perfectly centered stack is needed for the next image processing step.

Table 3.2: Crystallographic information used for simulation (Figure 3.2, panel 4). This is an example showing the information needed to create the CIF file for the β' phase.

Symmetry information	
Lattice type	P
Space group name	P 63/m
SG number	176
Setting number	1

Lattice param.					
a	b	c	α	β	γ
7.15	7.15	4.05	90	90	120

Unit-cell volume	179.307217Å^3

Structure param.							
Element	x	y	z	Occ.	B	Site	Sym.
Si	0.00000	0.00000	0.25000	0.660	1.000	2a	-6..
Si	0.66667	0.33333	0.25000	1.000	1.000	2d	-6..
Mg	0.61530	0.69540	0.25000	1.000	1.000	6h	m..

The last image processing step is to mask the (intense and possibly saturated) direct beam. The direct beam is present in all of the PED patterns in the PED stack and used for aligning the stack. However, it is not present in the simulation model. This step must always be done directly after the alignment of the stack. As the masking of the direct beam assumes that the direct beam is in the middle of the PED pattern for all the PED stacks. This concludes the image processing for the experimental data and the PED patterns are now ready to be matched with the simulated data.

3.2.2 Simulated Model Data Processing

This subsection discusses the simulation (right) branch of Figure 3.2.

(4): The first step to create simulated (kinematic and not-processed) diffraction patterns based on a physical model is to define the CIF for each phase. It can be quite time-consuming to retrieve all the required crystallographic information from literature, but it is a crucial step in order to create a good physical simulation. The creation of the CIF file is quite straightforward as long as the crystallographic information is available, Table 3.2 shows the information needed in order to create a CIF file, here for the phase β'. With the CIF file created, several visualizing tools (for example: VESTA, JEMS or MTEX) can be used to visualize the crystal structure or diffraction pattern. [39, 40, 41]

(5): By using each phases symmetry order, shown in Table 3.3, each point on the full equatorial plane, defined in section 2.1.1, can be mapped to the stereographic triangle (IPF). This reduces the number of possible orientations by a factor of 2 (low symmetry, i.e. monoclinic) to 24 (high symmetry, i.e. cubic).

(6): By first finding the orientation of the Al matrix, the possible orientations of the associated phases are further limited. This is one of the essential novel steps in the present study. The phases will move toward the lowest energy configuration. This lowest energy configuration has a fixed OR with the Al orientation. Since rotational invariance is achieved by doing the affine transformation described in (3), the orientation of the Al matrix is known and fixed. This allows us to calculate the OR without first finding the orientation of the Al matrix, thus removing one degree of freedom. The OR for the current system is shown in Figure 2.11. I.e, β' will have a lowest energy configuration in the [010] direction when the Al matrix is oriented in the [001] direction. This allows to further reduce the number of possible orientations.

(6)-(7): For a perfect sample, the OR will give a perfect 1 to 1 mapping, which in theory would allow for only one entry in the template library for each phase. However, due to not having a perfect sample or perfect detector, an error margin needs to be considered. The sample can i.e have internal stresses or it may be slightly bent. Hence a misorientation angle is allowed. The figure shows a few concentric circles, these circles illustrates different misorientation angles. Higher misorientation angles will allow a larger error and will thus sample a larger portion of the reciprocal space. Low misorientation angles will allow for a smaller template library, but requires a better detector and a flatter region of the sample. After choosing the misorientation angle, diffraction can be simulated for all of the phases. Experimental parameters, such as the camera length, acceleration voltage and the diffraction calibration must be provided to the model.

A max excitation error, s_{max}, has to be provided. This parameter is studied in this work, see chapter 5 for an in depth analysis. Using the theory of non-precessed diffraction, see subsection 2.2.2 and section 2.4, an initial value can be chosen to be the inverse of the sample thickness. However, manual iterations will be necessary to reach a satisfactory match. To find the best value, the bisection method can be used. The template library is now ready to be matched with the experimental PED patterns.

3.2.3 Matching Simulated Data with Experimental Data

(8): The final step is to match the rotated, aligned and masked PED stack with each template library entry. The workflow has made sure that there is rotational and translational invariance between the PED stack and the simulated diffraction library. This is a requirement for good pixel by pixel comparison methods. The pixel by pixel correlation methods tested in this work are: SAD, NSAD, SSD, NSSD, NCC and ZNCC, as defined in subsection 2.6.2. For each PED pattern in the stack the similarity is calculated with each entry in the template library.

The number of comparisons, C is governed by Equation 3.2. The workflow presented in this chapter was tailored to minimize the number of comparisons, while still being able to distinguish the relevant phases. The number of PED patterns, s, is chosen in step (2), the number of phases, p, is chosen in step (4) and the number of orientations, o, is chosen in step (7) when defining an misorientation angle. The number of pixels per pattern, px is governed by the size of the reciprocal space, and can be altered in (2).

$$C = (s \cdot px\cdot)(p \cdot o \cdot px) \tag{3.2}$$

Some material systems will have important reflections further out in the reciprocal space, thus having to expand the number of pixels. Altering the number of simulated orientations will allow for a finer/coarser angular resolution, for the Al-β'-β'' material system it has been shown (subsection 4.3.1) that an angular resolution of 1.2% is sufficient to reliable distinguish the three phases in experimental data sets. An initial value of 1% step size can be used.

SPED analysis is often used to analyze large areas in order to get good statistics. However, this increases the number of number of PED patterns and is computationally expensive. Introducing more phases to the template library will increase the problem size proportionally. So, sampling density could be guided by computing resources. The present work has been done on a computer with the following specifications; Intel(R) Core(TM) I7-4700HQ CPU @ 2.40GHz with 8.00GB installed memory (RAM) using Ubuntu Linux.

3.3 Template Matching Notebook

A working template matching Jupyter Notebook, using pyXem v0.11.0 is provided in section A.2. The current section will explain the notebook step by step starting from the top.

First, the notebook loads the required libraries (section A.2 panel 1). There are four main libraries that have been used: NumPy, DiffPy, DiffSims and pyXem. DiffPy is a prerequisite needed in order to load .cif files into a proper DiffPy structure. pyXem is the main open-source library used, and this is also where the contributions have been made. DiffSims is needed in order to simulate diffraction for pyXem.

Next the experimental parameters are set, (section A.2 panel 2). The accelerating voltage and camera length is described in section 2.3. The real space step length is set in order to set the scan calibration. The diffraction calibration parameter is the number of pixels that correspond to one nm, this is easily calculated by looking at Al, which is aligned to the 100 ZA, the distance from the direct beam to a reflection is known - hence one only need to do a simple calibration.

The data is then loaded into a DiffPy structure and normalized, (section A.2 panel 3). This data is 256px·256px, where each pixel represents one (4D-SPED) image, as described in section 2.4. The data is be cropped with the member function dp.inav() in order to do the matching in a reasonable time frame. This cropping is shown in Figure 3.3. Now the data must be calibrated and normalized. The data type of the individual pixels should be 64-bit floats, however as a fail safe, this is performed explicitly. The normalization is done in the usual way, by using the highest number of the data as the reference, this achieves a unitless number in the range [0.0, 1.0].

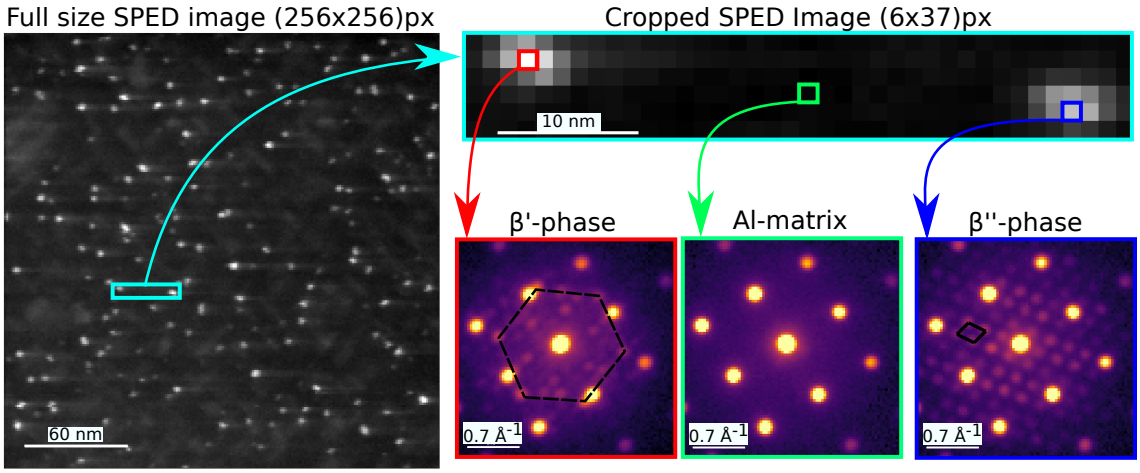

Figure 3.3: The full size SPED image(256x256)px is cropped to an area, (6x37)px, containing two different precipitates. The precipitate to the left is the β'' precipitate and the precipitate to the right is the β' precipitate. The underlying hexagonal and monoclinic structure has been highlighted by a black-line overlay.

Panel 2 in section A.2 performs the three image processing steps discussed in Figure 3.2 panel 3. The in-plane rotation is performed by Euler's convention (Figure 2.5) in order to get a constant frame of reference. The function center_direct_beam() performs the alignment of the PED stack. The parameters radius_start, radius_finish and square_width currently has to be found by manual inspection of the experimental data set, and a schematical view of how they are found are shown in Figure 3.4. The masking of the direct beam is performed after the alignment, as the center of the direct beam then is assured to be in the center pixel. The center pixel is approximated by a circle with radius $r_{mask} = 7$ for the current data set. The intensity is then inverted within the circular mask.

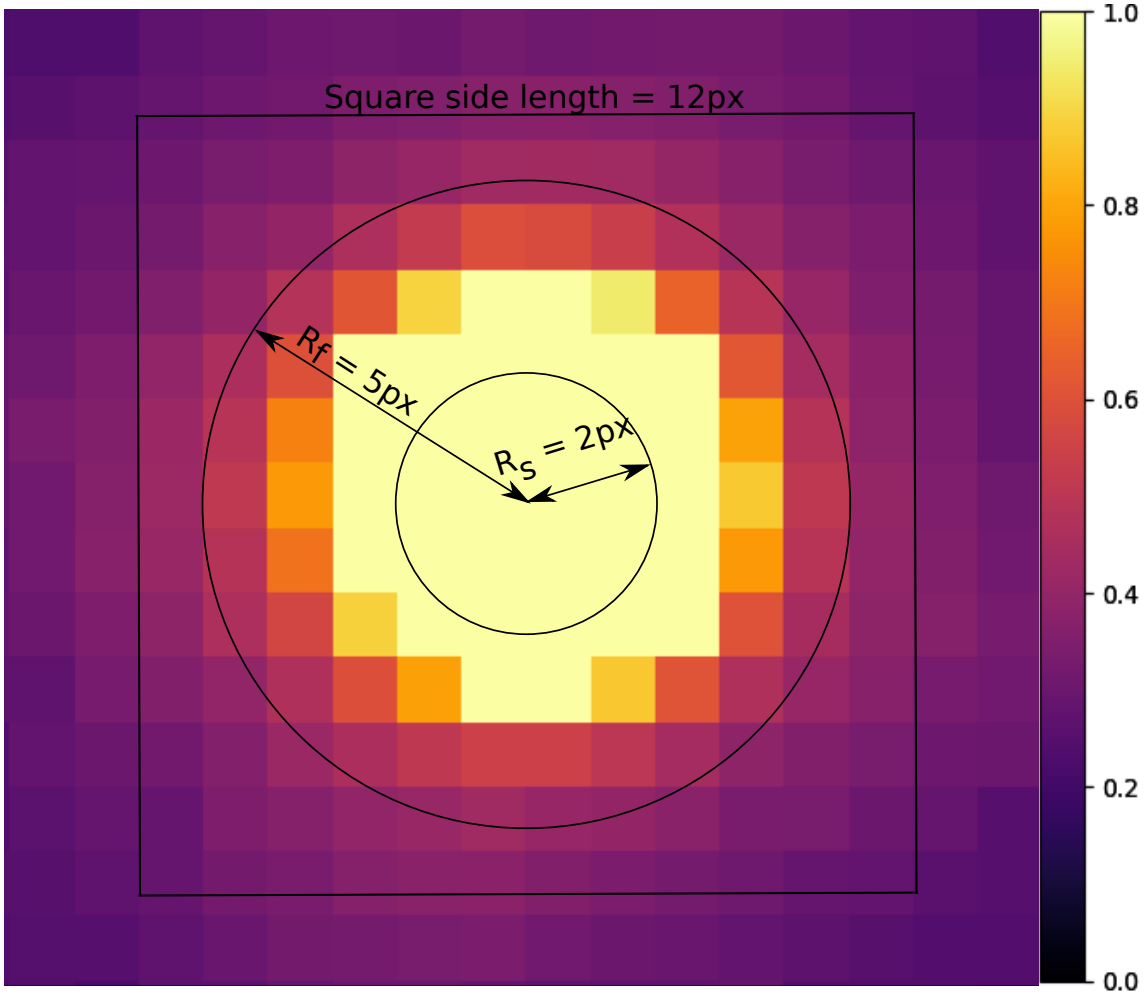

Figure 3.4: A close-up view of the direct beam in the raw dataset. R_s is the radius_start parameter, while R_f is the radius_finish parameter used in the function center_direct_beam(), they represent the lower and the upper bound for the radii of the central discs used in the alignment of the stack. The square width is half the side length that captures the direct beam in all scans, meaning that the centering algorithm is stable against diffracted spots brighter than the direct beam. The colorbar shows the relative intensity

Table 3.3: Crystal system and symmetry order of the four candidates that are analyzed in this work. The information about their crystal structure and symmetry order is given by their SG shown in Table 2.2.

Candidate	Crystal system	Symmetry order
Al	Cubic	24
Q'	Hexagonal	12
β'	Hexagonal	12
β''	Monoclinic	4

The next step is to create a precise CIF for all of the phases. As shown in section 2.1.1, all crystal systems in existence can be described using knowledge about their unit cell, space group and lattice parameters. For the Al-Mg-Si(-Cu) (6xxx series), this information is summarized in Table 2.2.Panel 2 in section A.2 loads a folder containing all the CIF files, while the optional panel 5.1 prints the name of each phase in the CIF folder. Panel 6 allows investigation of any combination of phases contained in the CIF folder. The user must provide the phase names (use panel 5.1 to input the correct name) and the associated crystal systems in the list of tuples phase_info.

The work will put special emphasis on three phases, β', β'' and Q' in addition to the Al matrix. The easiest phase distinction is when the phases have very different diffraction patterns, as is the case with Al, β' and β" phase distinction. A measure for how different the diffraction patterns will be is the difference in symmetry orders. As Table 3.3 shows, the most symmetric candidate is cubic Al with symmetry order 24, and the least symmetric is monoclinic β'' with symmetry order 4. Of all the phases known to occur in Al-Mg-Si-(Cu) there are no triclinic candidates with symmetry order 1, the only less symmetric phase is C with symmetry order 2. Thus, Al, β' and β" should provide the highest difference in the diffraction patterns between any 3-phase combination in the Al-Mg-Si-(Cu) alloy, which in turn should give the correlation function the best chances for phase distinction. The hardest phase distinction is when the phases have very similar diffraction patterns, as is the case with Q' and β'. Both the easy case and the hardest case is analyzed in section 4.5 and section 4.6.

Next the parameters for the simulation are set in section A.2 panel 7. Finding a good value for s_{max} is hard, but subsection 5.2.2 describes a method for finding an initial value for s_{max}. The angular resolution needs to be less than 1.2°, as discussed in subsection 4.3.1. The misorientation angle is however dependent on the accuracy of the OR and the thermo-mechanical history of the sample.

Panel 8 in section A.2 creates a rotation list using the OR with Al for each phase. Panel 8.1 samples around the [0,0,1] direction of Al with a given misorientation angle and given angular resolution. Panels 8.2, 8.3 and 8.4 applies the OR to the β" β' and Q' phases and makes rotation lists.

Panel 9 in section A.2 combines the phase names with the associated crystal systems and rotation lists. This is loaded into a StructureLibrary object, which is needed in order to compute the ED patterns. Before computation of the ED patterns, the the size of the structure library can be found with panel 9.1. It is important to check that the size of the structure library not exceeds the maximum library size that the computer can handle, discussed in section 4.1. Too many templates will lead to rapid swapping on the RAM-disk which causes the computer to slow down or stop.

Panel 10 in section A.2 computes electron diffraction patterns for a given crystal structure. The DiffractionGenerator object only accepts two arguments accelerating_voltage and max_excitation_error. It then performs the three following steps:

- Calculates the reciprocal lattice of the structure - Finds all reciprocal points within the Ewald sphere with radius $r_{ewald} = \frac{1}{\lambda}$, as derived in subsection 2.2.2.
- For each reciprocal point $\boldsymbol{g_{hkl}}$ corresponding to the lattice plane (hkl), compute the Bragg condition, Equation 2.10.
- The intensity of each reflection is then given (in the kinematic approximation) by Equation 2.27.

The diffraction library (or template library) is now ready to be filled with diffraction patterns. Each phase in the structure library is rotated to each associated orientation and the diffraction pattern is calculated each time. The resultant diffraction patterns can be animated or plotted using panel 10.1 in order to verify that the correct rotation list has been applied. This verification process has been done for Al and β' in panel 10.1.1. The diffraction library can be saved using panel 10.2.

The final step in the template matching notebook is to perform the template matching step. This entails calculating the correlation score between the template library and the experimental data. In indexer.correlate() the correlation functions defined in subsection 2.6.2 can be chosen. The correlation results are then saved for each diffraction pattern, and the results may be visualized as e.q. phase maps or as an overlay onto the experimental data set.

Chapter 4

Results

The main work has been creating the template matching notebook described in section 3.3, which does a bare minimum of preprocessing steps in order to accommodate the future use of NMF-processed data sets. In this chapter, the results produced with that notebook are presented. A discussion follows the results.

4.1 Maximum Template Library Size

The maximum number of simulated diffraction images for two different RAM sizes have been tested. The maximum number of templates are here defined by when the the memory needed exceeds the memory available. This leads to rapid swapping on the RAM-disk, which slows down the computer to a nearly inoperable state. The results are shown in Table 4.1.

Table 4.1: Maximum template library size

RAM [GB]	Max templates [#]
8	2500
128	6000

The maximum number of templates is an important number. In order to be able to perform the template matching routine the number of templates in the template bank has to be below the maximum number of templates. With the common equidistant sampling routine on the whole IPF, with angular resolution 1.2°, the number of templates needed is about 6 million for the three phase system. A new sampling routine is thus needed to decrease the number of templates. The next section shows how sampling around the OR with a given misorientation angle decreases the number of templates to satisfy the maximum template library size criteria.

4.2 Using OR to Decrease the Number of Templates

The number of required templates in the template library bank has been greatly reduced using the method described in Figure 3.2 panels 6 and 7. For the relevant, low step size area, the amount of simulated templates is reduced by a magnitude of around 10^4, from 10^7 to 10^3. This reduction is shown in Figure 4.1.

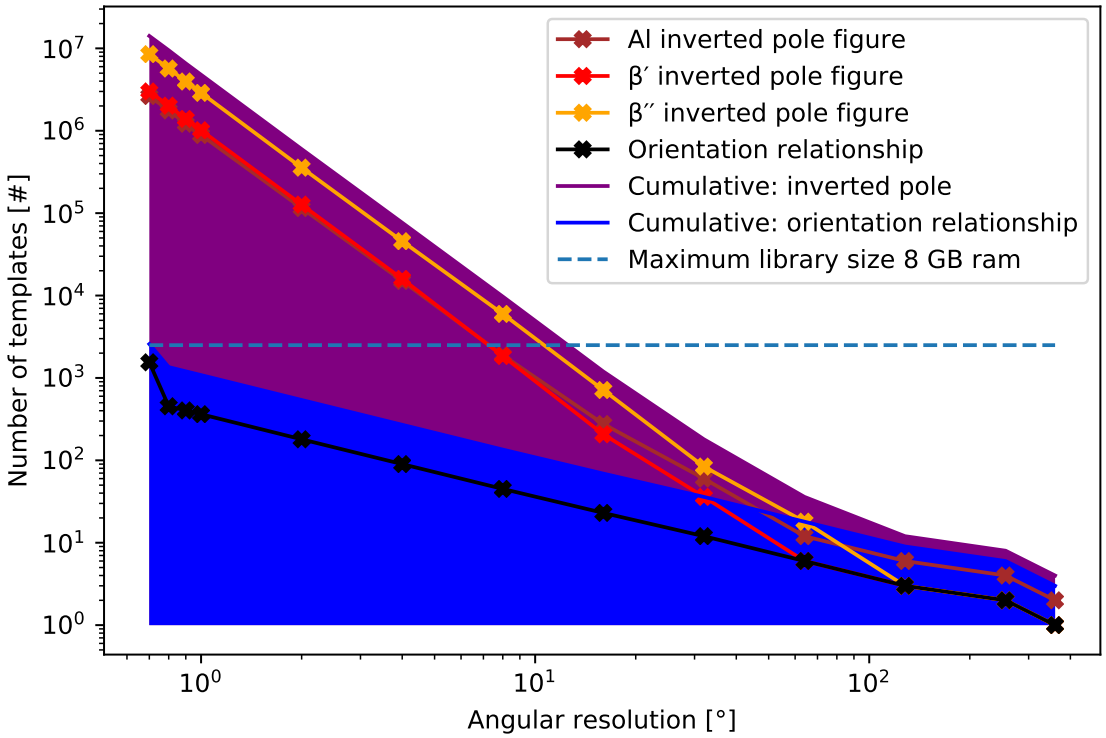

Figure 4.1: Template bank reduction when using OR. The brown, red and yellow lines shows the number of templates needed when using the old (commercially used) method, sampling equidistantly on the IPF for Al, β' and β". For this three-phase system, the cumulative graph is shown in blue shading. Meanwhile, the black line shows the number of templates needed when using the novel orientation relationship method, with a misorientation angle of 1°, for all three phases. Since the template is rotated to a common frame of reference (see Figure 3.2 panel 3), only one template for Al is required, this is discussed in chapter 5. The purple shaded area is the cumulative graph for the three phase system using the new novel method. The horisontal line at $N = 2500$ shows the maximum library size for a 8 GB RAM computer.

With the new sampling method, the size of the template library is no longer proportional to the symmetry order of the phase. This can be seen in the yellow line in Figure 4.1, where the monoclinic β" with the lowest symmetry order requires the higher number of templates in order to sample the full IPF than the red(Al) or brown(β') lines. In contrast to this, the new method is symmetry order invariant, as the black line (Al, β', β") shows. Since the new method is symmetry order invariant, the number of templates, N, with misorientation angle ϕ, angular resolution θ and number of phases n, is defined by the following relationship:

$$N = \left\lceil n \cdot \frac{360 \cdot \phi}{\theta} \right\rceil \tag{4.1}$$

4.3 Angular Resolution and Correlation Score

It is valuable to know what the coarsest θ which is able to distinguish the Al, β' and β" phases. As sampling finer than what is needed will only increase the needed computational resources. There will exist an optimal θ value which will minimize the computational resources needed, while still achieving good phase distinction and high correlation scores.

4.3.1 Coarsest Angular Resolution Estimation

An angular resolution of $\theta = 1.2°$ has been found to be the coarsest resolution which distinguishes the three phase system β', β" and Al accurately. At the tipping point, when θ exceeds 1.2°, the β' precipitate is falsely identified as a β" precipitate. The tipping point is shown in Figure 4.2

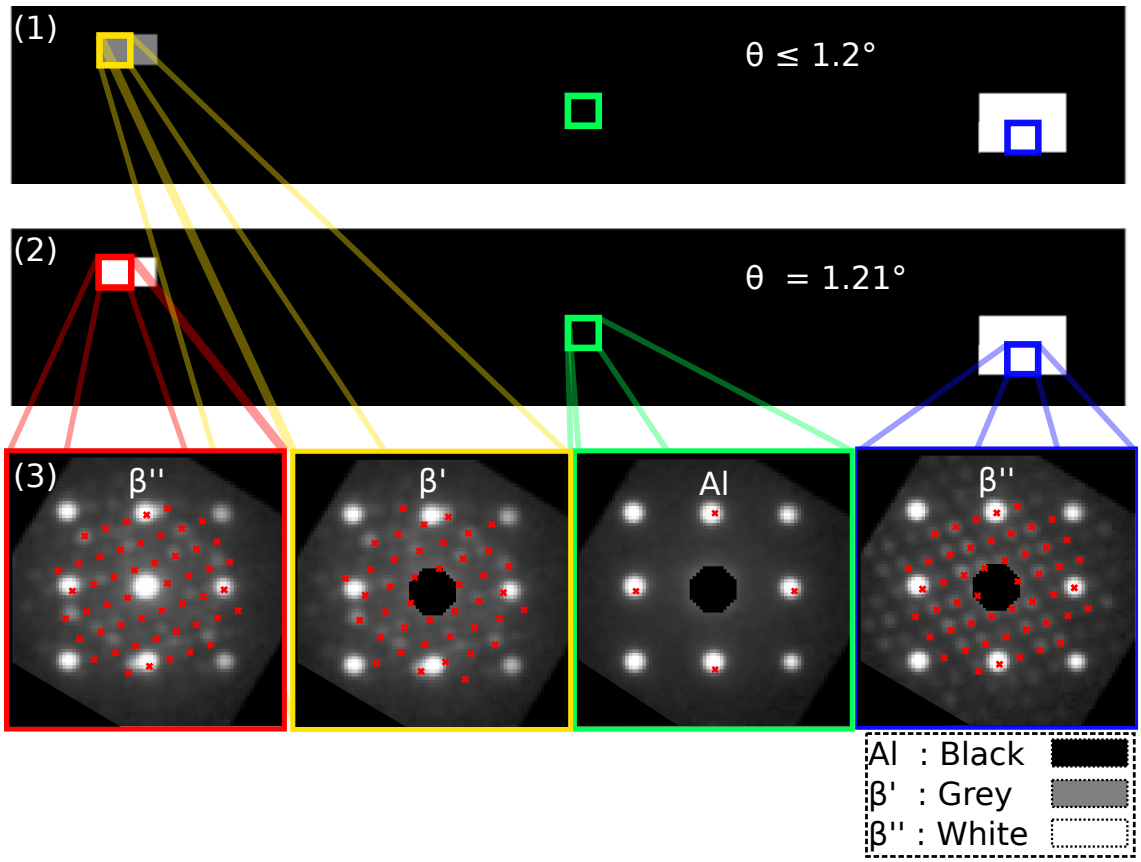

Figure 4.2: Estimation of the coarsest possible angular resolution. (1): Phase map for $\theta \leq 1.2°$, the angular resolution is fine enough to properly distinguish β', β" and Al. (2): Phase map for $\theta > 1.2°$ the angular resolution is too coarse and the β' precipitate gets falsely identified as the denser β" phase. (3): Best matches overlayed on the signals from (1) and (2).

4.3.2 Correlation Score Evolution

The NCC correlation score Q(θ), for β' and β" precipitates exhibiting strong reflections have been analyzed. Since the precipitates have different phases, different reflection densities and relative intensity differences, the correlation score for each phase has been normalized according to the following equation.

$$\frac{Q(\theta) - Q(\theta)_{\min}}{Q(\theta)_{\max} - Q(\theta)_{\min}} \tag{4.2}$$

where $Q(\theta)_{\min}$ and Q$(\theta)_{\max}$ is the highest and lowest correlation scores attained for each phase.

Figure 4.3 show that a finer θ than 1.2° yields diminishing returns. The highest correlation score is achieved with $\theta \leq 0.6°$ for β" and $\theta \leq 1.4°$ for β". The decrease in $Q(\theta)$ is only 3.4% for β" until $\theta = 4°$, where $Q(\theta)$ decreases with 44%. In summary, $\theta \leq 0.6°$ provides the highest correlation scores for β" and β'.

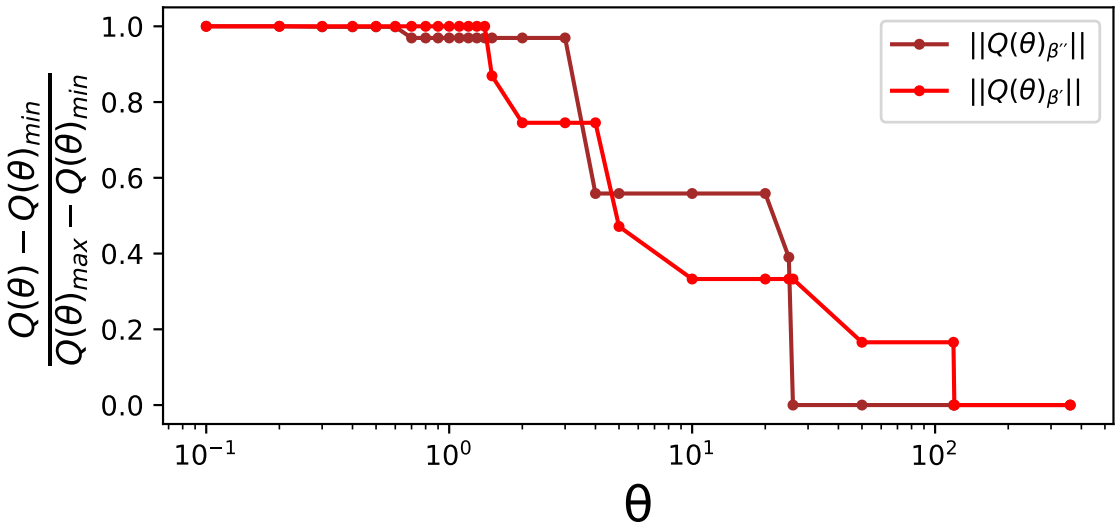

Figure 4.3: Correlation score evolution for β' and β" for $\theta \in [0.1, 360]$ when matching them with the Al matrix. $\theta \leq 0.6°$ provides the highest correlation scores for both β" and β'. When $\theta \geq 26°$, the analyzed β" pixel is no longer recognised as a β" phase. When $\theta \geq 120$, the analyzed β' pixel is no longer recognised as a β' phase.

4.4 Max excitation Error Determination and Sensitivity Analysis

The parameter max excitation error, s_{max} has been analyzed. The results show that for each phase and for each phase combination, there is a closed interval of s_{max} values that are able to provide good matches and that is able to distinguish the phases. Normalized cross correlation, as described in subsection 2.6.2, has been used as a measure of similarity in the following section.

4.4.1 Determining s_{max} Interval for Al

Determining the closed interval of s_{max} values for Al was performed by running the attached notebook and keeping all variables except s_{max} constant. This allows to find the lower and upper bounds for the interval by visual examination of the best matches versus the Al reflections. The s_{max} ranges and their effect on the phase matching are schematically shown in Figure 4.4 and analyzed in Figure 4.5. The s_{max} interval that gives the best matches is shown in panels 2 and 3 when $s_{max} \geq 0.241$, with panel 3 having the best correlation score due to the higher amount of good matches.

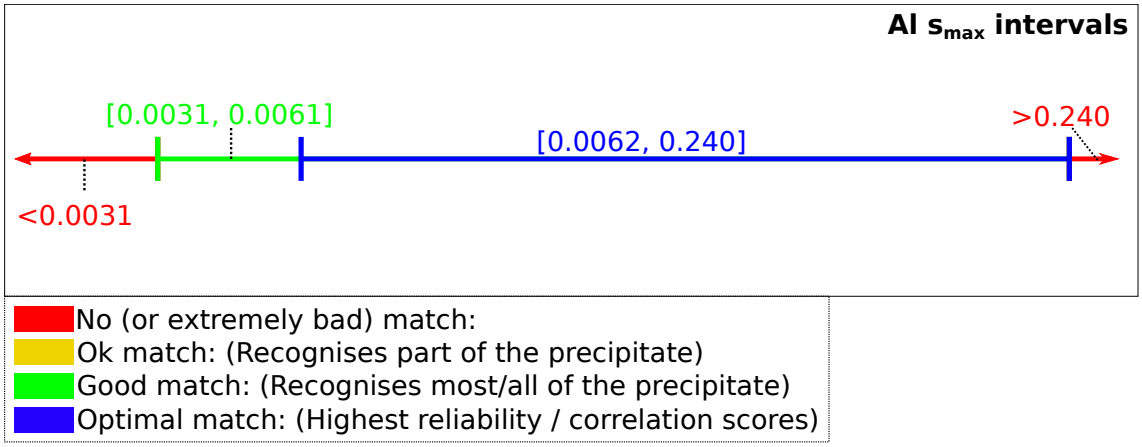

Figure 4.4: The possible s_{max} values gathered by visual analysis of the best matches versus the Al reflections analyzed in Figure 4.5.

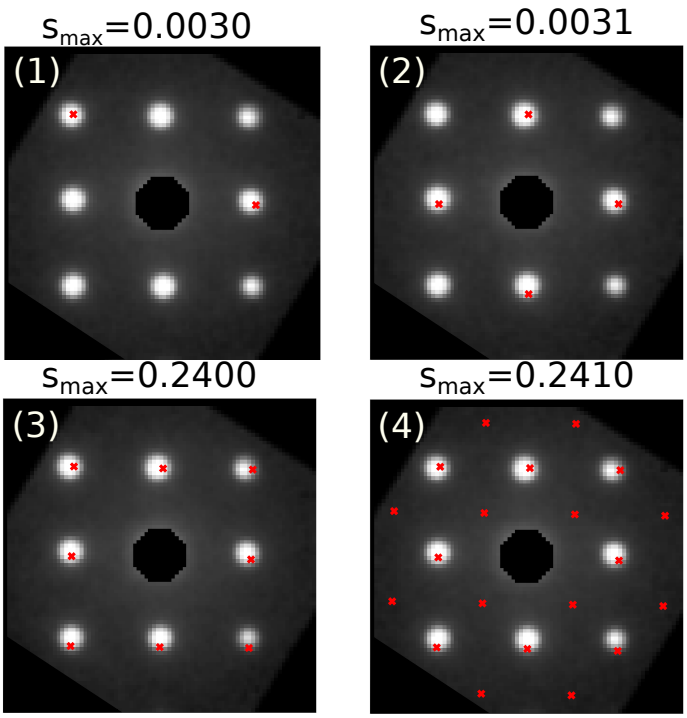

Figure 4.5: Determination of the s_{max} interval for Al. (1): If $s_{max} \leq 0.0032$ then the best matches will jump randomly from reflection to reflection for each pixel, without regard to which reflection is close or far away from the center. (2): The four closest Al reflections are always the best matches when $s_{max} = [0.031, 0.061]$. (3): Ideal s_{max} configuration is achieved when $s_{max} = [0.062, 0.240]$, all of the matches correspond with the Al reflections. (4): When $s_{max} \geq 0.241$ more matches than there are reflections are achieved. (1) and (4) is considered bad matches, which leads to an s_{max} interval of [0.0031, 0.240] for Al.

4.4.2 Determining s_{max} Interval for β'

The s_{max} ranges for β' and their effect on the phase matching are schematically shown in Figure 4.6. For β', the accepted range of s_{max} was determined by two criteria. The first criterion being visual examination of the best matches versus the β' reflections. This criterion is analyzed in Figure 4.7. The second criterion being that the best match comes from the β' template library - not from the Al template library. In other words, the phase map must be able to distinguish the Al matrix from the β' precipitate. This criterion is analyzed in Figure 4.8.

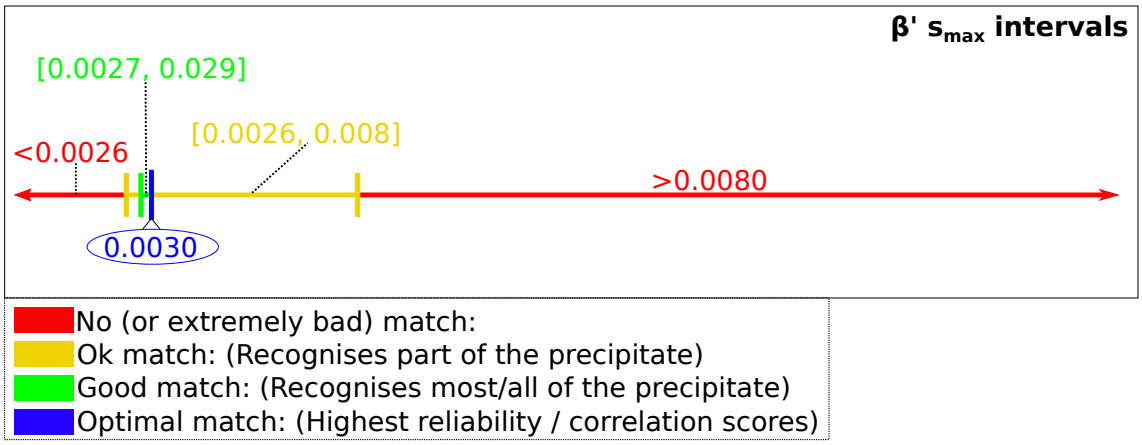

Figure 4.6: The possible s_{max} values gathered by visual analysis of the best matches versus the β' reflections analyzed in Figure 4.7 and the associated phase map analysis in Figure 4.8.

Determining the closed interval of s_{max} values for β' was performed by running the attached notebook and keeping all variables except s_{max} constant. The s_{max} interval that satisfies the criteria defined above lies in the range [0.0026, 0.008] (panels 2-11). However, the range $s_{max} \in [0.0027, 0.0030]$ (panels 3-5) stands out as the best being able to correctly identify a larger area of the precipitate. With $s_{max} = 0.0030$ (panel 5) being the optimal value for β', as it correctly identifies the largest area of the precipitate. When $s_{max} \in [0.0055, 0.0080]$ (panels 9-12), more matches than there are visible reflections is observed, however the algorithm still distinguishes Al and β'.

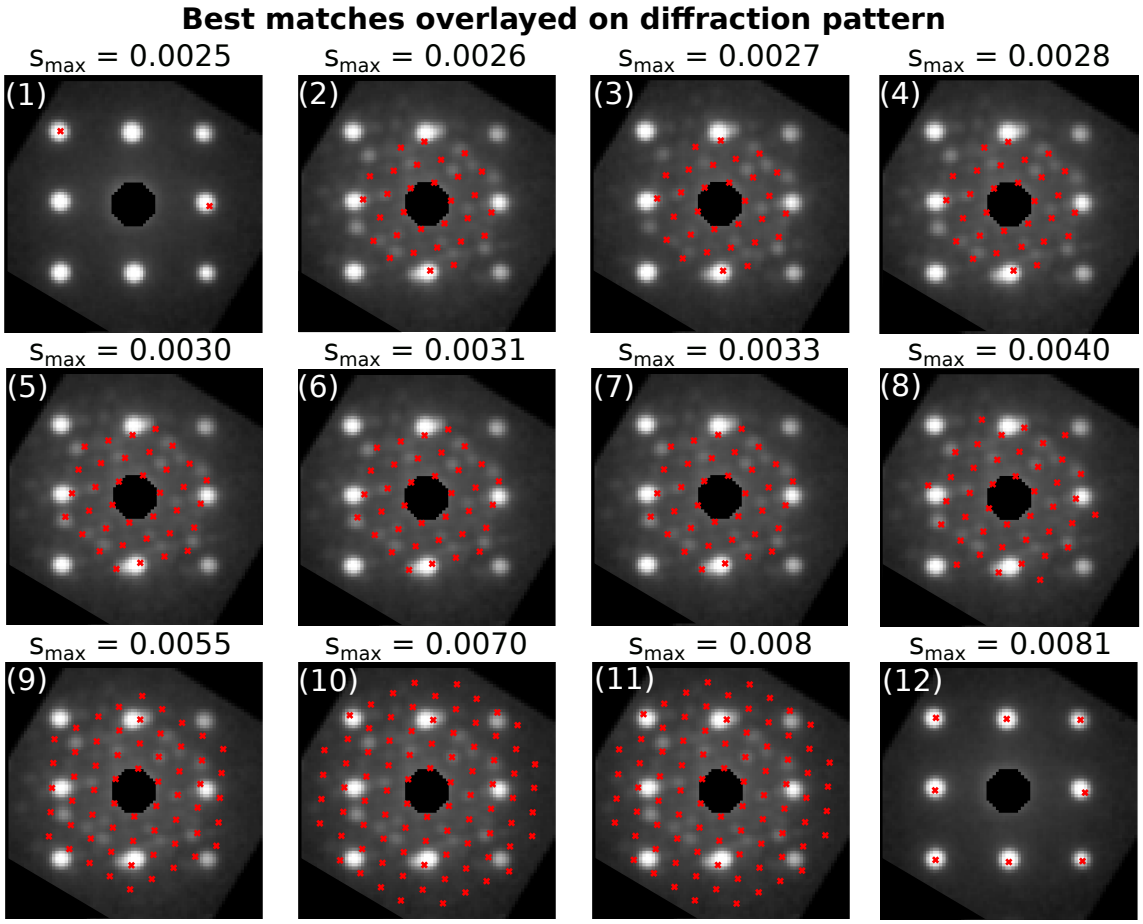

Figure 4.7: (1)-(12) shows the best match for increasing s_{max} values, the associated phase map is shown in Figure 4.8. (1),(12): The best match is not in the β' template library when $0.0025 \geq s_{max} \geq 0.0081$. (2)-(11): The best match is in the β' library. (9)-(12):When $s_{max} \in [0.0055, 0.0080]$ more matches than there are visible reflections is observed.

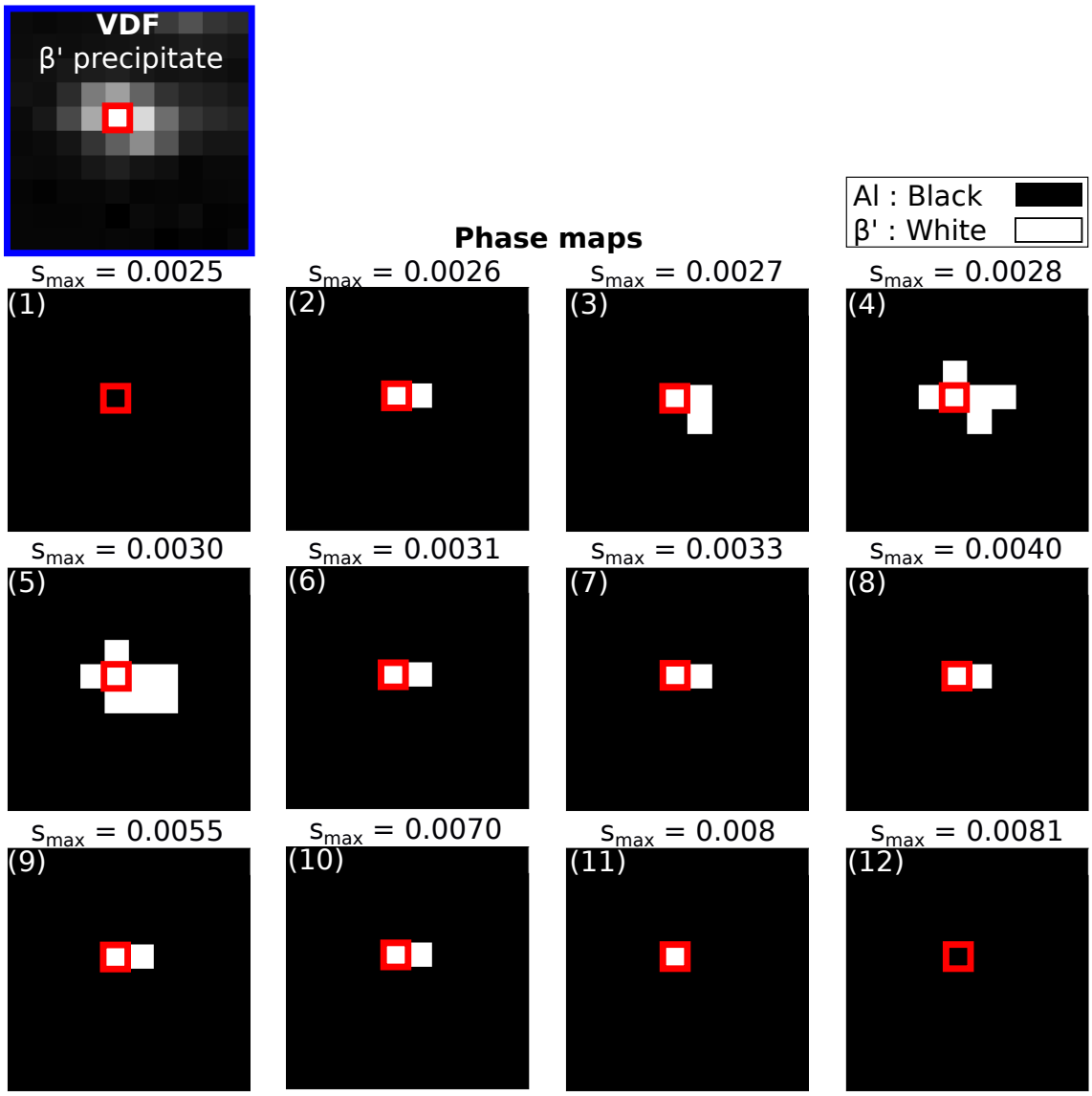

Figure 4.8: The phase maps on a β' precipitate for increasing values of s_{max}. The SPED image is cropped as to only contain a manually identified β' precipitate shown in the VDF. (1),(12): The notebook can not distinguish Al from β' when $0.0025 \geq s_{max} \geq 0.0081$. (2)-(11): When $s_{max} \in [0.0025, 0.008]$, the notebook can distinguish Al from β'. (3)-(5): When $s_{max} \in [0.0027, 0.0030]$, a larger area of the precipitate is correctly identified, with $s_{max} = 0.0030$ being the optimal value for β'. Each image (1)-(12) has a red pixel, whose best match is shown in Figure 4.7.

4.4.3 Determining s_{max} Interval for β"

The s_{max} ranges for β" and their effect on the phase matching are schematically shown in Figure 4.9. For β", the accepted range of s_{max} was determined by two criteria. The first criterion being visual examination of the best matches versus the β" reflections. This criterion is analyzed in Figure 4.10. The second criterion being that the best match comes from the β" template library - not from the Al template library. In other words, the phase map must be able to distinguish the Al matrix from the β" precipitate. This criterion is analyzed in Figure 4.11. Determining the closed interval of s_{max} values for β" was performed by running the attached notebook and keeping all variables except s_{max} constant. β" is special as it has two candidate s_{max} intervals yielding good phase distinction.

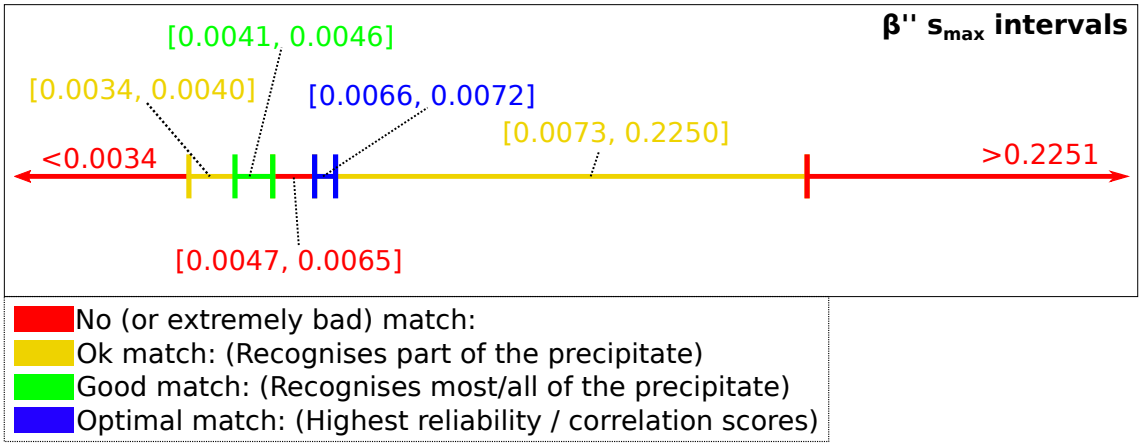

Figure 4.9: The possible s_{max} values gathered by visual analysis of the best matches versus the β" reflections analyzed in Figure 4.10 and the associated phase map analysis in Figure 4.11.

Figure 4.11 shows how the β" phase map evolves with increasing s_{max}. When $s_{max} \in [0.0034, 0.0046]$ (panels 2-8), the notebook accurately distinguishes Al and β". Moreover, the subinterval $s_{max} \in [0.0041, 0.0046]$ correctly identifies the whole β" precipitate on a level comparable with manual (expert knowledge) inspection.

When $s_{max} \in [0.0047, 0.0065]$ (panels 8-12), the dense β" pattern falsely outmatches the sparse Al matches. In this interval, only the four closest Al reflections are matched (see Figure 4.5 panel 2). When $s_{max} \in [0.0066, 0, 0073]$, the number of correct Al reflections (Figure 4.5 panel 3) increases from the four closest to all eight, which increases the correlation score for Al and thus allows for a good phase map in this interval. This interval also has the highest correlation score, as more reflections is correctly matched. However, even the extended interval $s_{max} \in [0.0066, 0.2250]$ yields good phase distinction.

When $s_{max} \geq 0.2250$ the β" density of matches again falsely starts to identify Al as β", this effect is exaggerated by the fact that Al when $s_{max} \geq 2.41$(Figure 4.5 panel 4) gets a sudden drop in correlation score.

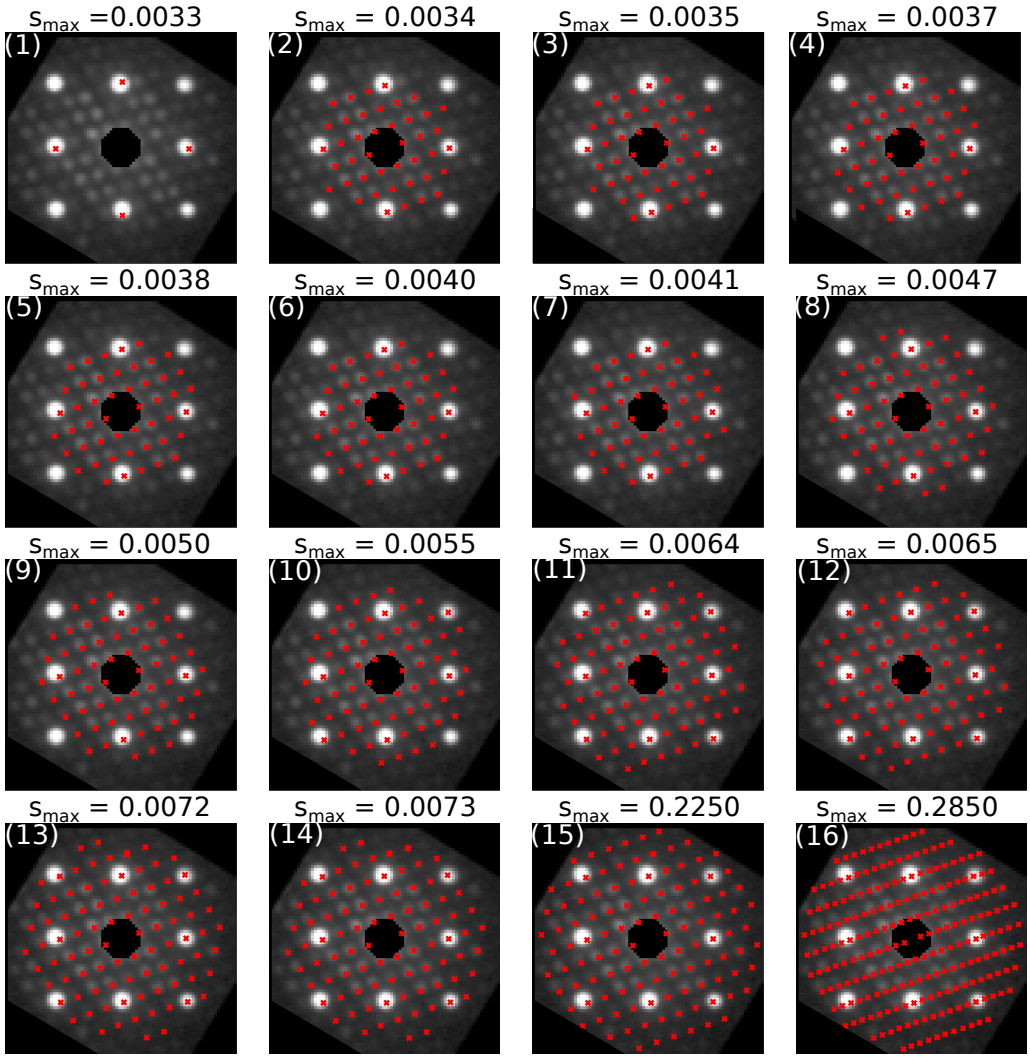

Figure 4.10: (1)-(16): Shows the best match on a β" precipitate for increasing s_{max} values, the associated phase map is shown in Figure 4.11. (1): When $s_{max} \leq 0.0033$ Al has a better correlation score than β". (2)-(15): When $s_{max} \in [0.0034, 0.2250]$ all the best matches are lined up near perfectly with the β" reflections. (16): When $s_{max} = 0.2850$ There are twice as many matches as there are β" reflections. Also, when $s_{max} \geq 0.2850$ the the best match is always from the β" library and the density of matches increases.

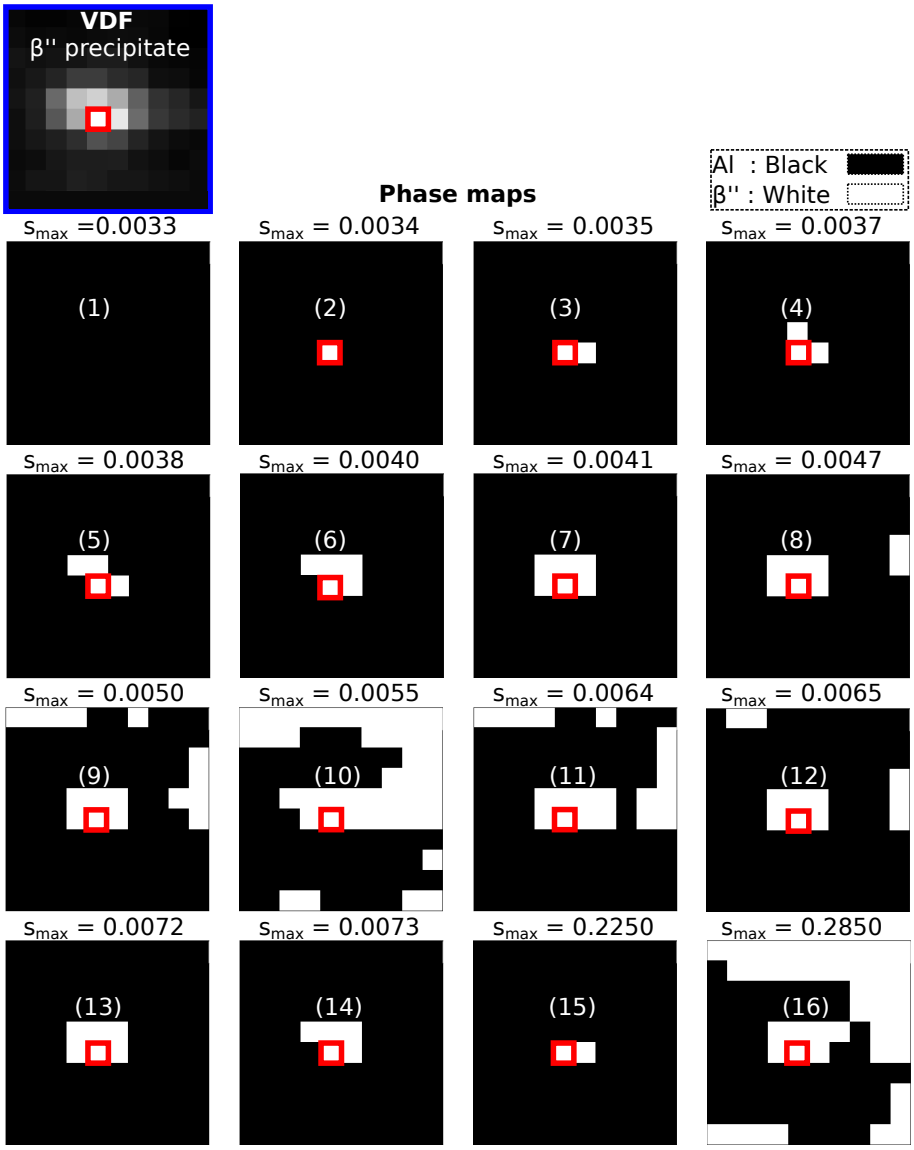

Figure 4.11: The phase maps on a β" precipitate for increasing values of s_{max}. (1): The notebook can not distinguish Al from β" when $s_{max} \leq 0.0033$. (2)-(6): When $s_{max} \in [0.0034, 0.004]$ more and more of the β" precipitate is identified correctly. (7): When $s_{max} \in [0.0041, 0.0047]$ the β" precipitate is perfectly identified. (8)-(12): When $s_{max} \in [0.0047, 0.0065]$ Al gets falsely identified as β" precipitates, this false identification effect reaches its peak when approaching $s_{max} = 0.0061$ and diminishes when reaching the endpoints of the interval. (13): When $s_{max} \in [0.0066, 0.0072]$ β" is perfectly identified. (14)-(15): When $s_{max} \in [0.0073, 0.2250]$ less and less of the precipitate is correctly identified. (16): When $s_{max} \geq 0.2250$ β" starts to overshadow Al until β" eventually is the only identified phase. Each image (1)-(16) has a red pixel, whose best match is shown in Figure 4.10

4.5 Phase Mapping of Phases with Different Symmetry Order

Increasing the number of phases to a three-phase system from a two-phase system limits the interval of possible s_{max} values. By superpositioning the information about possible s_{max} values, presented in section 4.4, for cubic Al, hexagonal β' and monoclinic β", two possible ranges of s_{max} emerges; $s_{max} \in [0.0034, 0.0040]$ and $s_{max} \in [0.0066, 0.0072]$, see Figure 4.12.

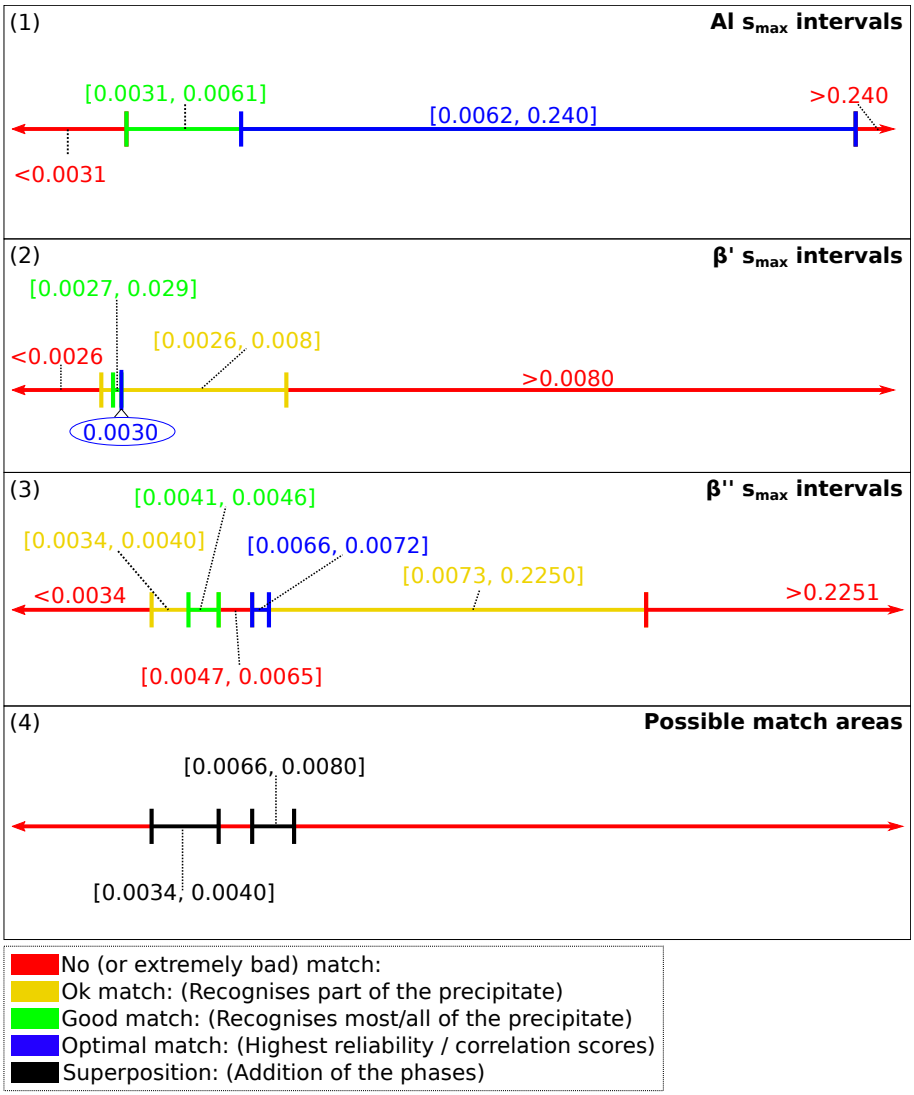

Figure 4.12: Determining possible s_{max} intervals for the three-phase system Al, β' and β". The s_{max} ranges from section 4.4 are summarized for each phase. The possible match area is a superposition of the allowed values (yellow, green, blue) and the red no-match area. The superpositioning reveals two possible match areas. The lower possible match area emerges when $s_{max} \in [0.0034, 0.0040]$ and the higher possible match area emerges when $s_{max} \in [0.0066, 0.0080]$

These ranges are two possible s_{max} candidates for a three phase system. The upper interval contains the optimal value for both Al and β" identification, while only a part of the β" precipitate is identified. The lower interval contains good (not optimal) matches for both β" and Al, while β' identification still is limited to part of the precipitate.

The lowest interval, when $s_{max} \in [0.0034, 0.0040]$, allows for identification of β', β" and Al simultaneously while achieving a high correlation score. Figure 4.13 shows that for the lowest s_{max} interval, $[0.0066, 0.0072]$, both of the precipitates are accurately matched. The phase map, panel 3, is perfect when comparing it to manual (expert knowledge) identification. The orientations, seen in panel 3, is also near perfect, there is a small centering issue, in which the best match is somewhat shifted in regards to the center of mass. Thus, this method is able to distinguish at least 3 different symmetry order phases.

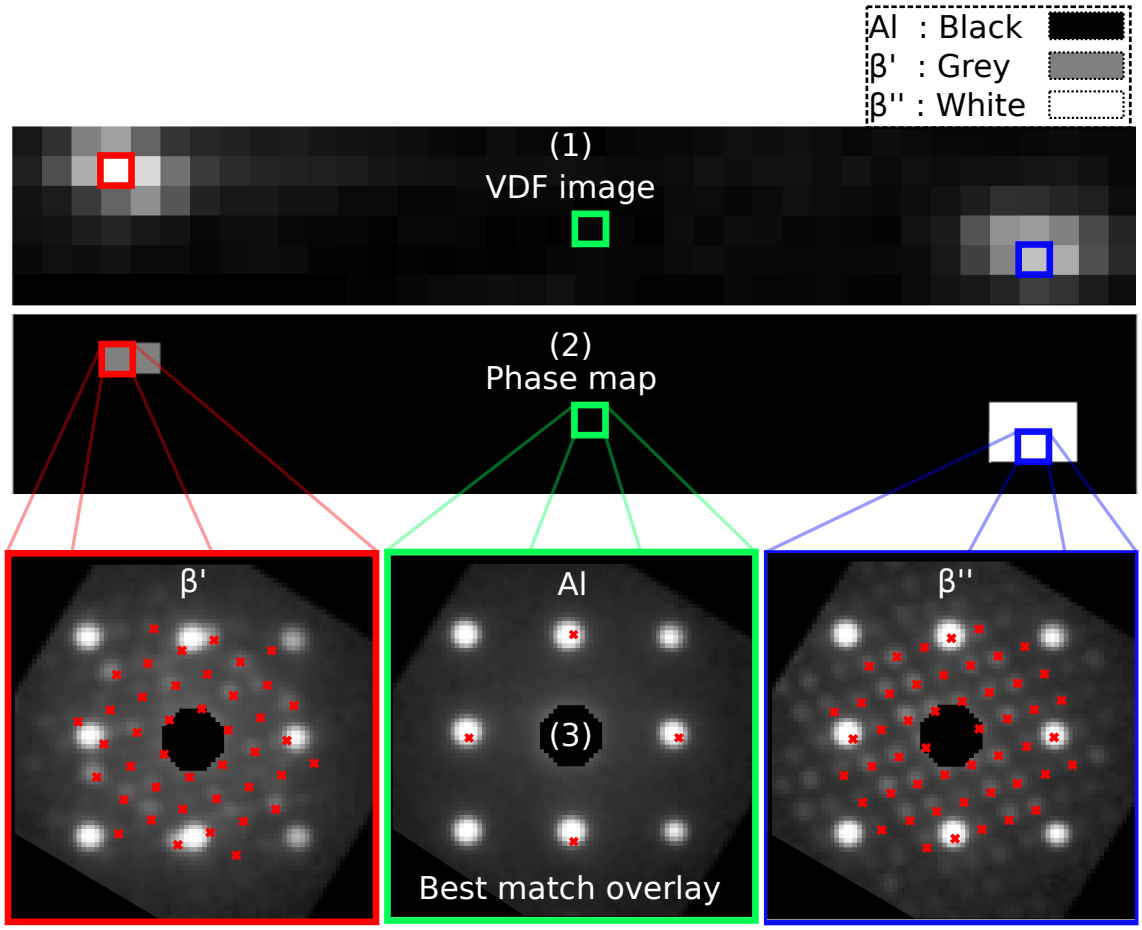

Figure 4.13: Phase map and associated diffraction pattern with the best match overlayed for $s_{max} = 0.0040$. (1): Shows the VDF image containing two precipitates β' and β" along with Al. (2): The resultant phase map after performing the template matching routine. (3): The best matches for β', Al and β" overlayed on the associated diffraction pattern

The higher interval, when $s_{max} \in [0.0066, 0.0080]$, does not allow for identification of β', β" and Al simultaneously. Figure 4.14 shows that both of the precipitates are identified as β" for four different s_{max} values equally distributed in the interval. Meaning that the highest correlation scores come from the β" template libraries. Thus, the high interval s_{max} area in conjunction with normalized cross correlation is not able to distinguish the two phases.

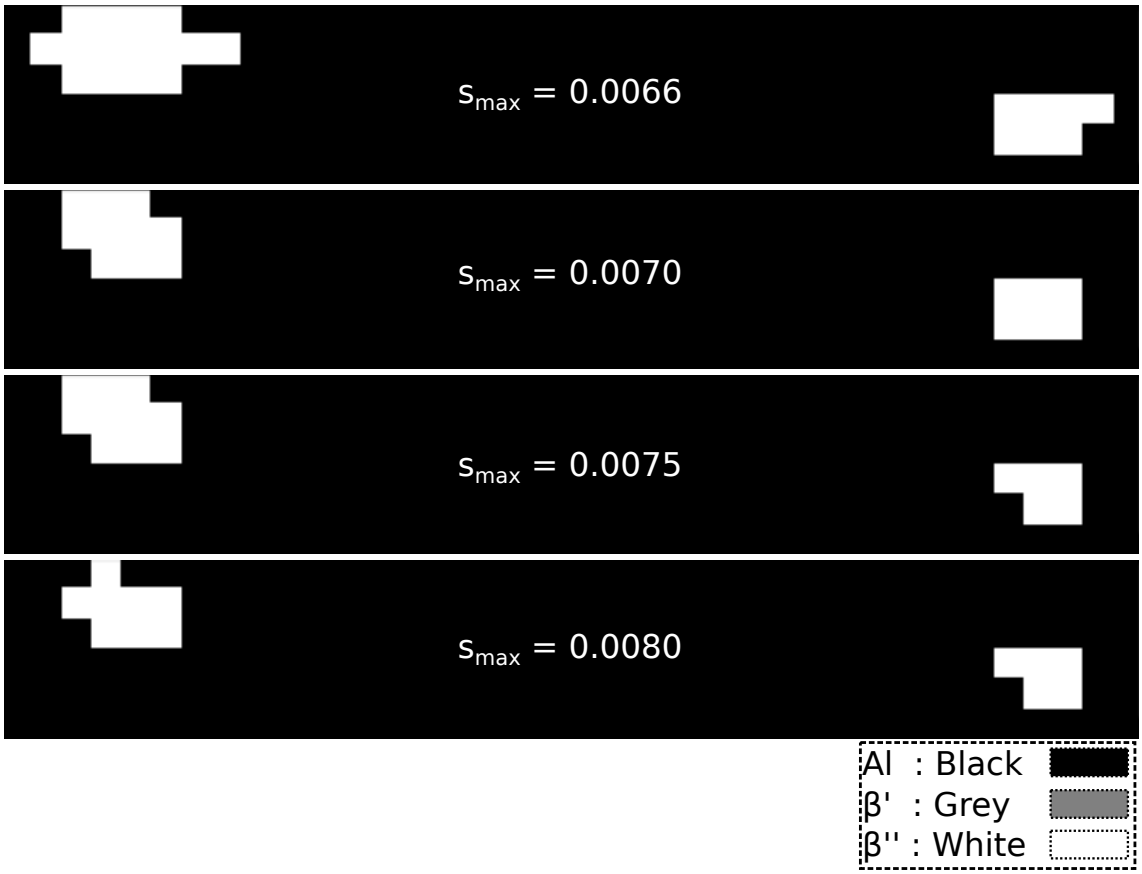

Figure 4.14: Phase map and associated diffraction pattern with best match overlayed for s_{max} values in the range $[0.0066, 0.0080]$. There is no s_{max} in this range which is able to distinguish β' and β". The β' precipitate is falsely identified as a β" precipitate.

4.5.1 Effect of Masking the Direct Beam

Masking the direct beam is proven to be a mandatory step in order to be able to distinguish hexagonal β' from monoclinic β". As can be seen in Figure 4.15, where $s_{max} = 0.0040$. The mask radius which produces the best match is 7 pixels, this mask radius also envelops the entire direct beam. When there is no mask, the β" is falsely identified as a β' precipitate.

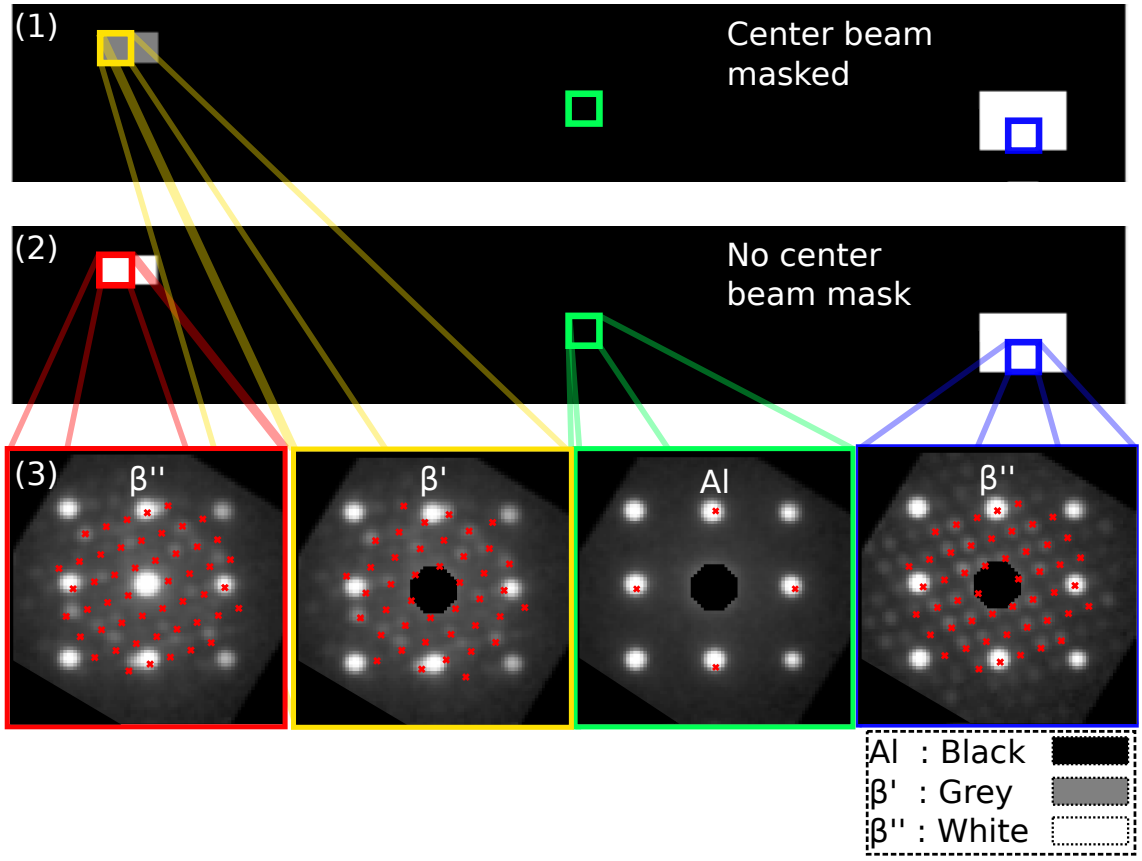

Figure 4.15: The effect of masking the direct beam.(1): When there is no mask, the strong β' reflections gets falsely identified as the β" phase. (2): When there is a mask which envelops the direct beam, the distinction between Al, β' and β" is identified. (3): Best matches overlayed on the signals from (1) and (2).

4.6 Phase Mapping of Phases with the Same Symmetry Order

By introducing a new phase, Q' (see Figure 2.11), which has space group P6 similar to the space group of β', $P6_3/m$, and the same symmetry order of 12, the notebook has been tested for two (almost equal) phases. In order to do this testing, a experimental data-set which was artificially aged(see Figure 3.1 panel (5)) for 8 hr instead of 3 hr was used in order to have the phases Q' and β' to simultaneously present.[6] The analyzed area is shown in Figure 4.16, where both Q' and β' coappear.

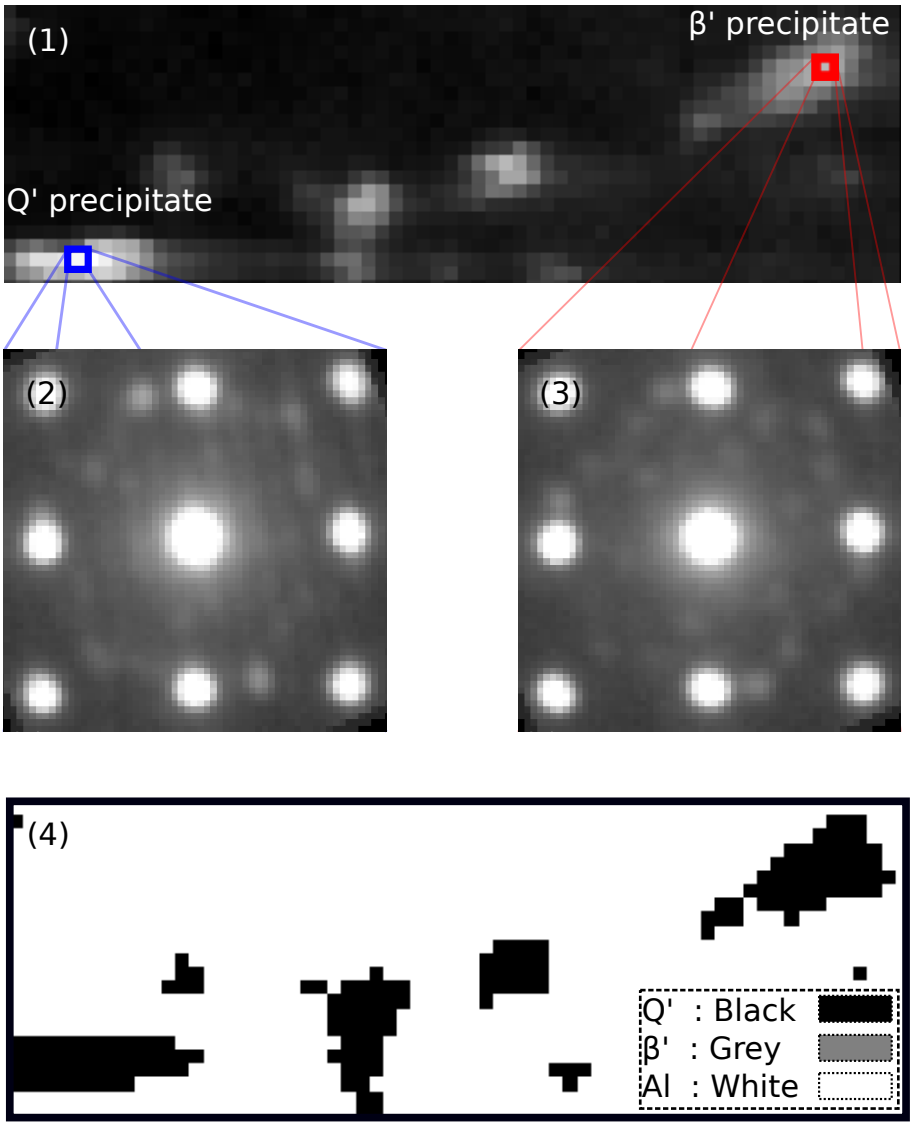

Figure 4.16: VDF image containing β' and Q' precipitates. (1): Investigated area containing β' and Q' precipitates. (2), (3): The diffraction patterns for β' and Q' phases in center of precipitates. (4): Phase map for the three phase system β with $s_{max} = 0.003$ and $\theta = 0.2°$ for the area defined in (1). The β' precipitate gets falsely identified as a Q' precipitate.

When introducing a different data set than analyzed previously, it was anticipated that new values for s_{max} had to be found for each of the phases since the thickness of the samples will be different. This process is however simplified by using the optimal β' s_{max} value for the first dataset, $s_{max} = 0.003$ as a starting point. In fact, $s_{max} = 0.003$ seems to still be the optimal value for β' contrary to what was anticipated.

The template matching routine has not been able to distinguish the similar β' and Q' phases by increasing the angular resolution. This is shown in Figure 4.16. Even if the angular resolution has been pushed to 0.2°, no phase distinction between β' and Q' has been observed. Both Q' and β' can however be distinguished vs the Al matrix. The β' precipitate gets falsely identified as a Q' precipitate.

4.7 Alternative Correlation Functions

In order to decrease the effect of s_{max}, the four correlation functions(SAD, SSD, NCC and ZNCC) explained in subsection 2.6.2 have been tested. The results show that NCC provides the best matches. ZNCC provides the same results as NCC, but at the cost of computational power. SAD and SSD is quite a lot faster than NCC. Both SAD and SSD is able to recognise the Al matrix, but is not able to distinguish it from any phases. Using the known optimal $s_{max} = 0.0040$, the phase maps and associated diffraction pattern for the four correlation functions is shown in Figure 4.17. As a result of this, same symmetry order (such as Q' and β') distinction is not achieved by using SAD, SSD, ZNCC or NCC correlation functions.

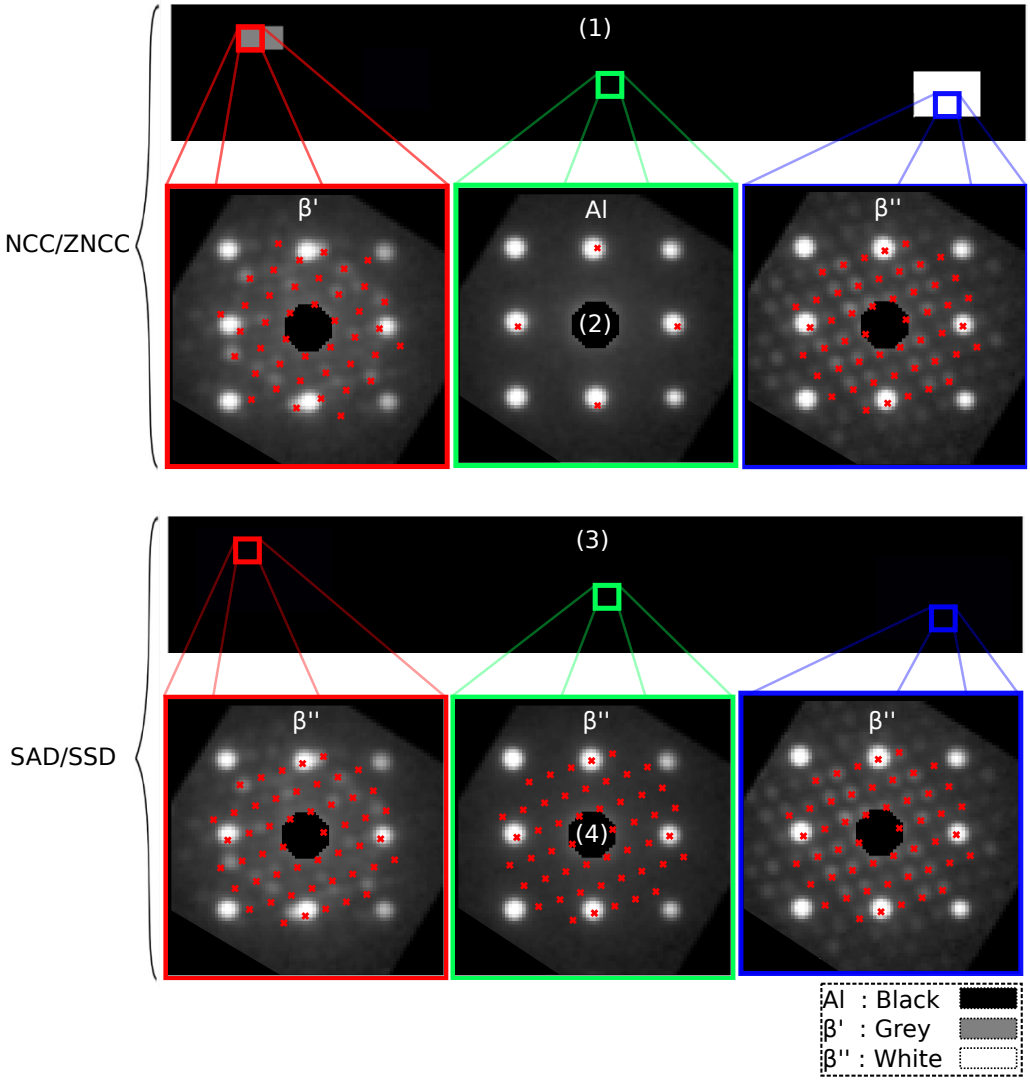

Figure 4.17: Results for four different pixel by pixel correlation functions. Phase map and associated diffraction pattern with the best match overlayed for $s_{max} = 0.0040$. (1): Phase map for NCC and ZNCC, both correlation functions provide the same (perfect) phase map and the same best orientations. (2): Diffraction pattern with best match overlayed for NCC and ZNCC. (3): Phase map for SAD and SSD, both correlation functions can not distinguish between the phases, the whole area is identified as the dense β" phase.

Chapter 5

Discussion

5.1 Reduction of the Template Library

As Table 4.1 shows, a template library with less than 6000 template entries is needed in order to use the template matching algorithm when the available RAM is less than 128 GB. The highest sampling step size which can distinguish the three-phase system β', β" and Al is 1.2°. When comparing this hard limit with Figure 4.1, it is clear the current template matching routine would be impossible when sampling the whole IPF for each phase requiring around 6 million templates. By implementing the new novel OR method (described in Figure 3.2 panels 6 and 7), the number of templates needed is reduced by a factor of 10 000. Figure 4.1 shows that the new method only requires around 1000 templates for a 1.2° sample step size, For comparison, the commercial template software (Nanomegas Index) uses ca. 2000-6000 templates, dependent on settings.[34] Since $1000 \leq 2500$, the new method allows personal computers with less 8 GB RAM to perform the template matching routine for the three-phase system.

The new method is symmetry order invariant, meaning that symmetry order of the phase does not affect the number of templates needed. This makes the increase in the template bank due to addition of new phases a linear function, as shown in Equation 4.1. The black line in Figure 4.1 shows the number of templates needed for any single phase.

The Al-Mg-Si-(Cu) system has 10 possible phases(when counting Al), as described in Table 2.2. Calculating the number of templates needed, by utilizing Equation 4.1, is a trivial task. With $n = 10$, $\phi = 1$ and $\theta = 1.2$:

$$N = 10 \cdot \frac{360 \cdot 1}{1.2} = 3000$$

3000 templates are needed for a 10 phase system, with a misorientation angle of 1 and a angular resolution of 1.2°. 3000 templates excludes a 8 GB RAM computer but a 128 GB RAM computer would easily be able to perform the template matching routine for the 10 phase system with 1.2°resolution with regards to the total template library.

With the old method, the size of the template library is proportional to the symmetry order of the phases. This is due to the difference in the size of the IPF of the phases, as shown in Figure 2.3. With the old method the resolution of the template library is limited by the least symmetric crystal system, in this case monoclinic β''. This effect is shown in Figure 4.1, where β"(yellow line) requires roughly 10 times as many templates than β'(red line).

Alterations on the size of the template library is achieved by the alteration of three variables: The misorientation angle ϕ, the number of phases n and the angular sampling resolution θ. The misorientation angle is dependent on the thermo-mechanical history of the sample. The number of phases to be considered can be altered by using prior knowledge about the aging process of the alloy, and when the phases coexist. Lastly, the angular sampling resolution is dependent on the correlation function.

5.1.1 Misorientation Angle

If the template library needs to be further reduced, a possible way is to decrease the misorientation angle. The OR between the constituent Al matrix and the phase always yields one discrete orientation. The orientation yielded by the OR is the lowest energy configuration for the phase. Addition of a misorientation angle is a safety precaution in which orientations close to the lowest energy configuration also is added to the template library. In fact, the best match for Al is exactly the [0,0,1] orientation, this reduces the number of templates needed for Al to only 1. Which in turn reduces the template library size down to $N = 2641$ per Equation 4.1. In order to use a 8 GB computer, the misorientation angle must then be reduced to 0.94°.

The reduction of the Al template library to 1 template is based upon a few assumptions. First, it is assumed that the beam is perpendicular to the Al foil. The misorientation of the matrix can be determined and works as the reference in all OR. With the current recording (phosphor screen, afterglow), and potentially oversaturation of Al reflections, small variations in the matrix can not be determined and for practical purposes can be set as fixed (i.e exactly [0,0,1]).

The artificial aging step in Figure 3.1 panel 5, attempts to restore the equilibrium state of the metal and to eliminate the unstable conditions brought by the prior operations. The main sample analyzed in this work was artificially aged for 3 hours. Equilibrium of the precipitates occurs when the particles reach a final chemical composition and crystal structure that does not change with further ageing. This is a special case, in which the misorientation angle be very small.

Samples that have have not yet reached an equilibrium state may require a larger misorientation angle in order to accurately find the best orientation. The intermediate precipitates undergo a number of transformations before developing into the final stable condition. It is expected that these phase transformations will be less coherent with the Al matrix and thus requires a larger misorientation angle.

5.1.2 Number of Phases

It is not always necessary to perform the template matching on all 10 phases, as all 10 phases might not coexist. During aging phase transformations occur, in which intermittent phases appear and is transformed. An example is the main sample studied in this work, which is tailored through its thermo-mechanical history as to only contain the three-phase system β', β" and Al. Thus, utilizing prior knowledge about what phases might coexist can linearly decrease the number of templates needed according to Equation 4.1. With $n = 3$, the template library is reduced to $N = 900$, which most likely can be run on any semi-modern home computer.

5.1.3 Angular Resolution

The angular resolution governs two things, the correlation score and whether two phases are distinguished or not. With NCC, $\theta \leq 1.2°$ is required in order to distinguish β" and β' in the current implementation, as shown in subsection 4.3.1. $\theta = 1.2°$ is a already a fine resolution, a finer resolution yields a minimal increase in the reliability and in the correlation score, as presented in subsection 4.3.2, at the expense of increased computational power as;

$$\lim_{\theta \to 0} \left\lceil n \cdot \frac{360 \cdot \phi}{\theta} \right\rceil = \infty. \tag{5.1}$$

Different correlation functions will require different angular resolutions. Pixel by pixel methods are inherently sensitive to minor translations or rotations, see subsection 2.6.2, correlation functions which look at the full-frame may not require such a fine resolution. This is further discussed in section 5.3. In this analysis, experimental finite resolution is not considered. For SPED in the current set-up this is about 1 degree as the pixel number is small and few points in the FOLZ are used. Electron back scattered diffraction based on Kikuchi lines, using HOLZ information, etc. have a superior angular resolution.[42]

By applying the above considerations regarding the misoriention angle for Al and the number of phases for the 8 hour aged sample, the template library for the three-phase system can be safely be reduced to

$$\left\lceil 2 \cdot \frac{360 \cdot 1}{1.2} \right\rceil + 1 = 601. \tag{5.2}$$

5.2 Effects of s_{max}

The simulation is not taking into account the precession angle described in section 2.4, instead a static unprecessed beam is simulated. Further the intensity distribution over the relrod is taken as a simple triangle and not $\sin^2$ function. Estimation of s for precessed data has been shown to be tricky.[43, 21] One could simulate patterns for different separate incoming angles and sum these patterns over a whole 360 degrees round and eventually multislice dynamic simulations to make simulations more like what happens in the experiment, but this will be computational demanding. With the first achievement, section 5.1, allowing for a small number of templates in the template bank this might become in reach, but not with the old IPF sampling method. However, estimating the relrods with a triangle and not utilizing the precession angle is the same thing the commercial package (NanoMegas Index) does and can be considered an acceptable first approximation for precessed patterns.[43]

s_g is defined as the distance from the reciprocal lattice point to a point on the Ewald sphere, subsection 2.2.2. For a perfectly unprecessed electron beam, s_g yields a distinct singular value. When precessing however, the thickness of the Ewald sphere is extended into a "banana-like" shape, see Figure 2.10. This elongation effect is not taken into account when simulating diffraction. This makes estimation of s_{max} for each reflection quite hard.

5.2.1 Reciprocal Space Limitation

As can be seen in Figure 4.5, 4.7 and 4.10, s_{max} can be tweaked in order to match a desired area of the reciprocal image. This effect is seen in the growth (i.e increasing reciprocal radius) of the number of matches overlayed on the diffraction pattern in panels 2-11. This growth can be modelled by concentric circles centered on the direct beam, as shown in Figure 5.1 where the concentric circles is overlayed onto the best matches from Figure 4.10.

The effect shown in Figure 5.1 can be utilized to understand why the higher possible match area in Figure 4.6 is unable to distinguish β' from β" while the lower possible match area is able. When comparing the diffraction pattern containing the strongest β' and β" reflections, it is immediately obvious that β" reflections are visible in the whole regarded reciprocal space, while β' reflections only are visible inside the box outlied by the 4 closest Al reflections. This is schematically shown in Figure 5.2.

In general, it is clear that for a receiver to "see" a signal it has to be greater than the noise floor. To actually detect the signal however, it is often required to be at a power level greater than the noise floor by an amount that is dependent on the type of detection used as well as other factors. For TEM signals, a signal to noise ratio of 10 seems to be sufficient to detect the signal, this is called the **minimum detectable signal**. Only when the intensity of a reflection exceeds the minimum detectable signal intensity one can obtain good results. This effect is shown schematically in Figure 5.3.

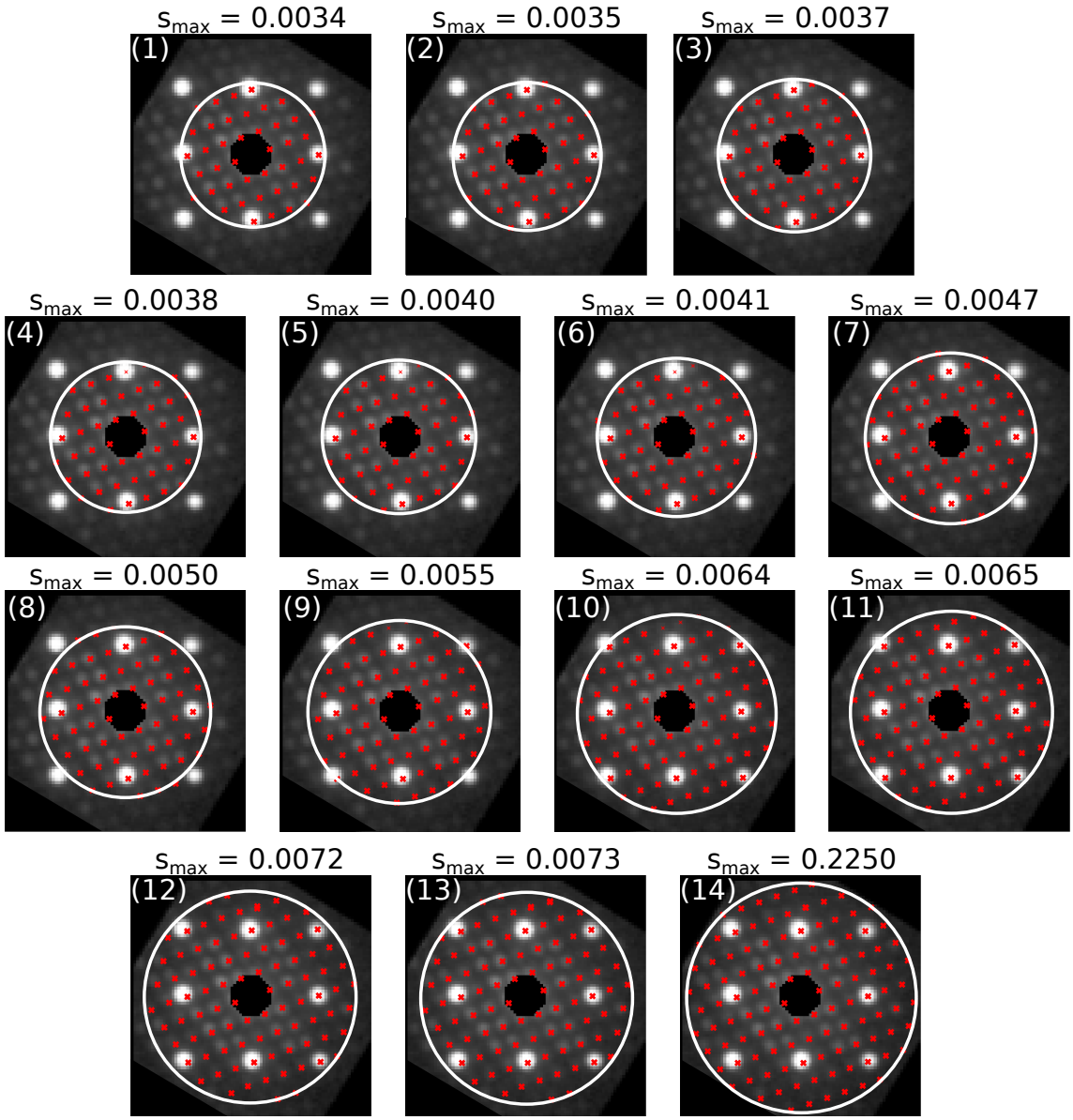

Figure 5.1: Concentric circles overlayed on best matches for β" for different values of s_{max}. (1)-(14): The circles grow in size and more and more of the reflections in the reciprocal space is matched.

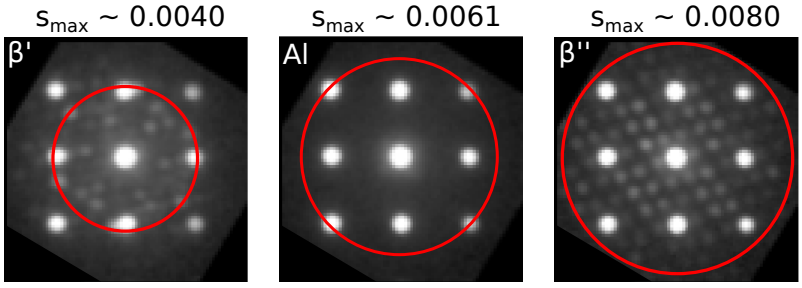

Figure 5.2: Schematic illustration of how far into the reciprocal space the reflections for Al, β' and β" is visible. The s_{max} values is modelled by a circle enveloping all of the (visible) reflections, as shown in Figure 5.1. For β', most reflections are considered when $s_{max} = 0.0040$. For Al, most reflections are considered when $s_{max} = 0.0070$. For β" most reflections are considered when $s_{max} = 0.0080$.

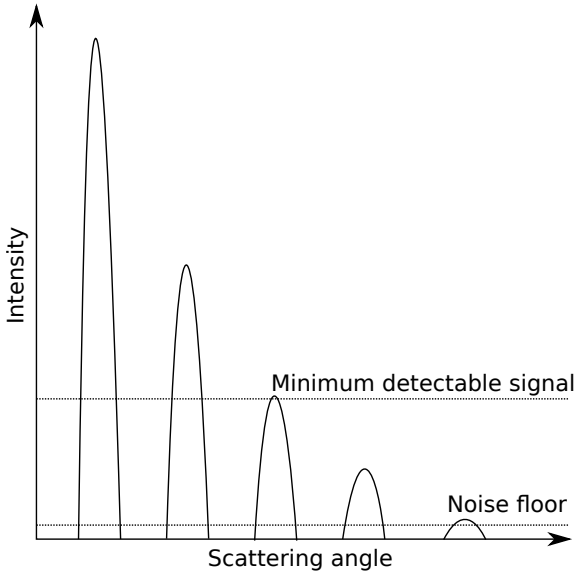

Figure 5.3: Schematic illustration of the miniumum detectable signal. When the Laue condition (Equation 2.14) is fulfilled, diffraction occurs. For real experiments, there will be a constant noise floor. A minimum signal to noise ratio of 10 is used to find the minimum detectable signal. All signals above the minimum detectable signal will be be detected.

With this in mind, another way to understand s_{max} is that it acts as a **signal to noise** limiter. The circles in Figure 5.2 have been found by visual inspection, but they can also be found objectively. First, choose an minimal accepted intensity value (10 times the noise floor). Second, find the furthest out pixel exhibiting the minimal accepted intensity value. The radius of the circle will then be the distance from the center pixel to the furthest out pixel.

Since there are almost no visible β' reflections outside the circle when $s_{max} \geq 0.0040$, the NCC (Equation 2.34) starts to favor the denser pattern produced by the β" precipitate. This explains why the β' precipitate in Figure 4.14 is falsely identified as β" in the higher possible match area $s_{max} \in [0.0066, 0.0080]$. The only possible match area left is thus the lower match area when $s_{max} \in [0.0034, 0.0040]$. As Figure 5.2 shows, when $s_{max} = 0.0040$, the perfectly envelops all of the visible reflections for β'.

The relative sparsity of the Al pattern (when compared to β") explains why Al gets falsely identified as β" in panels 8-12 and 16 in Figure 4.11. When $s_{max} \in [0.0031, 0.061]$ the circle shown in Figure 5.1, only envelops the 4 closest Al reflections. In the same interval, the number of β" reflections which is enveloped steadily increases (by about 25 reflections). This disparity in the density of the matches is a problem when applying Equation 2.34 as a measure of similarity. When s_{max} reaches 0.062, the 8 closest Al reflections is enveloped, and the relative match density between β" and Al decreased, and Equation 2.34 works well until $s_{max} \geq 0.2250$ where the relative match density becomes to large for Equation 2.34 to be able to distinguish the phases accurately.

5.2.2 Initial Value for s_{max}

For unprecessed electron diffraction, s_g is inversely dependent on the thickness of the sample and varies with $\sin^2$. The initial guess for s_{max} would then be around $s_g = 1/80 = 0.0125$. However, as Figure 4.13 shows, $s_{max} = 0.0040$ is the correct value for the regarded sample. The unprecessed guess is quite off the best value. A new method for determining s_{max} by pixel by pixel correlation functions is outlined in the following.

1. Choose a number of phases, n.

2. Find intensity value for minimum detectable signal for the data set- (see Figure 5.3)

3. For each phase: Determine how far into reciprocal space the reflections are visible. (see Figure 5.2 as an example)

    - Note the position of the pixel furthest out in reciprocal which has an intensity above the minimum detectable signal intensity.
    - Create a circle with radius from the center pixel to the noted pixel.

4. The smallest circle determines the best initial guess for s_{max}.

5.2.3 Effect of Masking the Direct Beam

The direct beam is not simulated and does not appear in the templates. Experimentally, the direct beam is the most intense and small variations could have huge impact on final outcome, as well as often being saturated and its position not discriminating between phases. If the reciprocal image contains the direct beam, then intensity based pixel by pixel correlation will be skewed towards the phases with densest patterns. The direct beam is unfortunately quite large, the size of the direct beam allows it to overshadow the underlying precipitate reflections. It is this effect which is shown in Figure 4.15, where the less dense β' gets misidentified as the dense β" when including the direct beam.

In summary, the code is not at all robust when changing s_g and this is one of the main drawbacks of the current approach. This was expected, due to not taking into account the precession angle and the "unphysical" shape function for the rel-rod. Potentially, thickness variations will make the found optimum only locally valid. Therefore, making an automated procedure guessing s_g will not be a viable long term solution. Instead, the simulation itself should be revisited - adding precession and incorporating better shape functions for the rel-rods so that the simulated intensity better matches the experimental results. This is a potential improvement of the right (blue) branch in Figure 3.2.

5.3 Alternative Correlation Functions

Matching phases that have different symmetry orders, and thus quite different diffraction patterns, is easier than matching phases with the same symmetry order and nearly identical diffraction patterns. Pixel by pixel based approaches such as SAD, SSD, NCC and ZNCC compares the intensities for each pixel. This approach will get skewed results when comparing two different phases with different reflection densities, relative intensity variations between the two phases. Testing of different pixel by pixel based approaches is important in order to either strengthen or weaken the assumption that pixel by pixel based approaches is able to distinguish near identical phases.

5.3.1 SAD and SSD

SAD is the simplest and computationally least expensive pixel by pixel correlation function while SSD is almost as computationally cheap, as explained in subsection 2.6.2. Therefore, it is of interest whether or not these functions can replace the NCC correlation function. Figure 4.17 panels 3 and 4 show that this replacement is not possible.

However, there might be merit in using SAD or SSD as a means of blob center detection. For example if one wants to remove the Al reflections, template matching can be used with SAD or SSD correlation functions with only Al reflections in the template bank. Then the best matches can be used as the center of mass for blob detection algorithms.

5.3.2 NCC and ZNCC

ZNCC deals with offset problems that might arise in a stack that is not properly aligned. This correction comes with a large computational cost. As Figure 4.17 shows, there is no difference in the results gotten from NCC and ZNCC. This might be due to a good alignment of the stack (Figure 3.2 panel 3) in the preprocessing step. This might indicate that the centering by using the direct beam is a good method for aligning the stack. However, as there seem to be no difference in the results gotten from NCC and ZNCC methods, NCC is will be the best method by time complexity analysis.

5.3.3 Other Correlation Functions

The template matching notebook has been able to map the three analyzed candidates, these candidates are very distinct (monoclinic, hexagonal and cubic). However, the goal is to be able to map out different phases, potentially nine in this alloy system (see Table 2.2), even if they have a more similar (i.e harder to distinguish) crystal structures. It is anticipated that new correlation functions will be needed. The current correlation function seem to overweight dense patterns and bias towards the simulated patterns. There are in particular three correlation algorithms that might be interesting to investigate further.

In the precipitate matching case where one are looking down one ZA and therefore the precipitates are aligned in a way which can be predicted to be just a rotation about the beam direction, one could do the matching on full frame simulations in polar coordinates using a cross correlation between template and experimental patterns with a shift along the azimuthal coordinate. This has been done by Foden et al[44] for Electron Backscatter Diffraction. They use a log polar space, for our case we could use straight polar space.[45]

Another idea that could be investigated is to reconstruct Kikuchi lines from PED pattern. As we are looking down a known ZA, reconstruction of Kikuchi lines should be possible. Then, matching the Kikuchi lines using open source EBSD software could be a viable option.

It should be noted that different correlation functions cost different amounts of computing time depending on number of pixels, size of total library and algorithm used. The number of comparisons is governed by Equation 3.2, but different correlation functions will have different time complexities. Pixel by pixel based approaches have the benefit of being fast, but full-frame approaches using subpar fourier transform algorithms could become a bottleneck. A optimal correlation function combines both speed and accuracy.

In the c-direction (as is the orientation here), looking along a 3-fold screw axis and normal of mirror plane, the differences between β' and Q' have no kinematically forbidden reflections.[12] However, since the Q' phase has a few large Cu atoms, there will be be stronger diffraction, leading to some reflections being more intense than others. This is seen in Figure 5.4, where some reflections are much stronger than the others. This feature helps experts to distinguish the two similar phases manually. A possible way to distinguish same symmetry order systems could be to identify these stronger reflections and perform a correlation algorithm more sensitive to (relative) intensities on these specific and discriminating reflections for areas NCC identify as Q' and β'. NMF (pattern recognition) applied to SPED data of these alloys can distinguish these two phases[6], but unsupervised machine learning can also misidentify them.[6, 46]

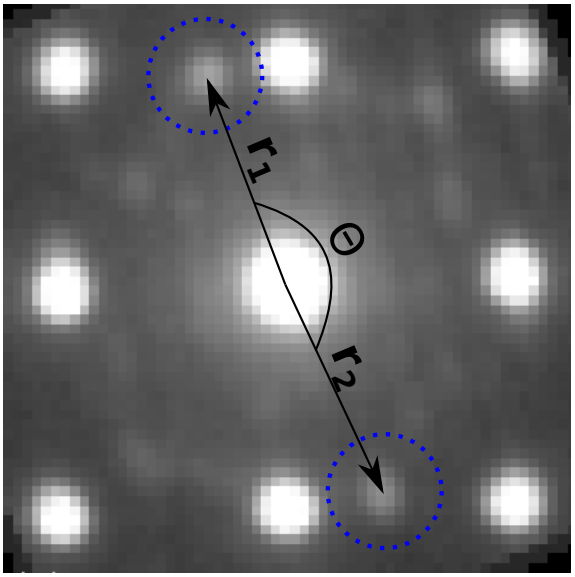

Figure 5.4: Q' diffraction. Some Q' reflections are more intense than others. Two vectors, $\boldsymbol{r_1}$ and $\boldsymbol{r_2}$, end at the centre of mass for these reflections, the angle between the vectors is Θ.

Chapter 6

Conclusion

The working template matching notebook, as described in section 1.2, was achieved. A notebook performing model-based template matching which correctly distinguishes and maps Al, β' and β'' with a good correlation score has been made. This can be used to verify machine learning approaches[6] and potentially be extended to more than 3 phases. However, in cases where candidate phases have same symmetry order, template matching as is falls short.

The template library has been vastly reduced by utilisation of known orientation relationships between the precipitates and Al. Instead of sampling over the full stereographic triangle, the precipitates' OR is cleverly used to only sample about a given orientation with a given misorientation angle. The new novel method reduces the number of required templates by a factor of about 10^4, from 10^7 to 10^3 for high resolution sampling. An analytical formula for determining the number of templates needed with the new method has also been developed. This allows template matching on any PC, ranging from home computers to supercomputers.

It is anticipated that the code will properly map more phases as long as the symmetry order of the phases are different. When phases have the same symmetry order and similar diffraction patterns, pixel by pixel based correlation functions seem to be unfit to perform the template matching and other measures of similarity might be needed.

Four different intensity based correlation functions have been tested: SAD, SSD, NCC and ZNCC. The results show that NCC yields the best correlation scores, and is able to distinguish different symmetry order phase systems. ZNCC increases the time complexity of the algorithm and does not yield better results. SAD and SSD are both not able to correctly identify more than one phase at a time.

Pixel by pixel intensity based correlation functions exhibit two weaknesses. The first weakness appears when there is a relative reflection density difference between the phases, the most dense phase will get a higher correlation score and thus might misidentify a sparse phase as a denser phase. The second weakness is when there is a relative intensity difference between the reflections of the phases. The phase with the most intense reflections will get favored. More intense reflections also might lead to more visible reflections, which in turn increases the effective reflection density.

The simulation also stands in the way of obtaining a fully automated procedure. The simulation does not take into account the precession of the probe, and the shape function of the rel-rod needs to be improved. This leads to the excitation error parameter s_{max} having to be manually found, and the code is not robust when changing s_{max}.

The effect of changing s_{max} has been analyzed systematically for the present experimental data sets with Al, β' and β". A new method for determining an initial guess for s_{max} has been proposed. Each phase combination will have a closed interval of s_{max} values that is able to distinguish the two phases. These s_{max} intervals seem to be a way to counteract the effects of relative intensity/density variations between the samples by effectively reducing or expanding the number of best matches, which usually grows like a circle with midpoint in the direct beam.

Chapter 7

Future Work

The results from this work have shown that further work needs to be done in order to reach the end goal of a fully automated SPED template matching procedure, either directly or via matching NMF components, for phase mapping of precipitates in Al alloys. The open source based template matching notebook developed as a part of this work can be regarded as a successful pilot project and a proof of concept. The first milestone, described in section 1.2 has been achieved. The next step is to test the code for more complex data sets containing more candidate phases. Also, a correlation algorithm which is able to distinguish near equal identical patterns must be developed. This chapter will summarize the discussion of the results and provide concrete suggestions for further work.

7.1 Improving the Speed of the Template Matching Routine

For template matching on the full SPED scan and for all possible phases, the speed of the template matching becomes an issue. As more phases are introduced, the template library will increase linearly. With the new sampling method, RAM is no longer a problem, but the computational time required will be a bottleneck. Three ways of achieving significant speedup have been discussed.

Massive speedup may be achieved by a trifecta of changes: First, and most important is a **reduction of the template library**, which was achieved in this work by utilization of OR. Secondly, **segmentation of the data into chunks** using Dask arrays instead of NumPy array.[47] This functionality is implemented in the latest version of pyXem (V.012) after the merge with pixStem, but the current work is based on V.011. Lastly, time consuming parts of the notebook are all shown to be embarrassingly parallel. Especially three functions will benefit from parallelization. The centering function center_direct_beam(), the simulation of the template library and the correlation functions (pixel by pixel based correlation functions are perfect candidates for parallelization). **Rewriting the code to be parallel**, either on CPU or GPU will give significant benefits.

1. Incorporate lazy-loading using Dask arrays instead of numpy ndarrays.
2. A parallelization of the three functions center_direct_beam(), simulation of the template library and the correlation functions.
3. Investigate the possibilities of using a GPU (e.q programmed using CUDA, openCL or MPI).

7.2 Improving the Simulation of the Templates

In order to make an automatic(low/none manual input) procedure, we need a way to properly determine all parameters used in the code. At the moment, there is one sensitive parameter that has proven hard to determine, namely *max excitation error*, s_g. One reason why this parameter is hard to determine is that the simulation of the template libraries at the moment does not take into account the precession angle. This, in addition to an implementations of more physical shape functions ($\sin^2$ instead of a triangle) might leave s_g obsolete and thus making an automatic procedure possible.

1. Add the precession angle to the simulation of the template library.
2. Add more physical shape functions for the relrods. (e.q $\sin^2$ instead of triangle)

7.3 Exploring Alternative Correlation Functions

The template matching notebook has been able to map the three analyzed candidates, these candidates are very distinct (monoclinic, hexagonal and cubic). However, the goal is to be able to map out different phases, potentially ten in this alloy system (see Table 2.2), even if they have a more similar (i.e harder to distinguish)crystal structure. Based on the result of this work it is anticipated that new correlation functions will be needed. This anticipation stems partly from that the current correlation function overweight dense patterns and bias towards the simulated patterns, and partly because of the relative reflection intensity between the phases. The commercial software is using only NCC[35]. Although tests in this study show that NCC is the most solid (of the four pixel by pixel based correlation functions tested) for SPED template matching, for other type of experimental data or for other questions alternatives might be desired. Two new correlation functions (not intensity based pixel by pixel) functions are suggested:

1. Do the matching on full-frame simulations in polar coordinates using a cross correlation between template and experimental patterns with a shift along the azimuthal coordinate.
2. Reconstruction of Kikuchi lines from PED patterns, then use established EBSD template or library approaches in available software to do the matching.

Another possible way to distinguish β' from Q' specifically could be to identify the stronger reflections in Q' due to large Cu atoms and perform a correlation algorithm more sensitive to (relative) intensities on these specific and discriminating reflections for areas NCC identify as Q' and β' as described in the last paragraph of subsection 5.3.3.

7.4 Improving the Experiment

On the experimental side, different sample thicknesses can be investigated with regard to the optimal s_{max} parameter for a given data set. Thick samples will allow more inelastic scattering, widening the reflections and causing a higher background noise. While thin samples will cause the reflections to collapse, which in turn will give less overlap(i.e excited area by a broadening beam is within different phases. This limits spatial resolution and distinction of phases). Less overlap will make pixel by pixel based approaches more viable. It is thus expected that extremely thin samples will allow for better correlation scores.

Technological advances on the detector side may reduce or eliminate unwanted effects. Afterglow of the phosphor screen, altering the shape of imaged atomic columns, may have (and is) an unwanted effect. Even electrons accidentally hitting the detector can cause errors for thin specimens. Indirect recording by an optical camera (CCD) of the fluorescence screen through the viewing glass gives very high noise levels. Direct detection detectors are causing a revolution in TEM community.[48, 49] If the noise is removed or decreased, pixel by pixel based approaches will be able to detect reflections that are overshadowed, thus increasing the correlation score. The noise floor in Figure 5.3 will thus be removed or decreased, allowing for a lower minimum detectable signal. Still the correlation function, Equation 2.34, is sum of intensity sensitive and extending the radius as discs as discussed subsection 5.2.1 will still be expected. So far, only one SPED system with direct electron detector which shows encouraging results for structural analysis is in operations (in Glasgow).[48] Several are under installation at NTNU, so these suggestions might be in reach in the near future

Especially interesting is whether better experimental setups will allow the template matching routine to distinguish almost equal phases such as β' and Q'. A starting point would be to perform the thermo-mechanical process described in Figure 3.1, where the sample is artificially aged in order to allow β' and Q' to coexist, then use a superior direct electron detector.

Bibliography

[1] T. C. Kriss and V. M. Kriss. "History of the Operating Microscope: From Magnifying Glass to Microneurosurgery". In: *Neurosurgery* 42.4 (Apr. 1998), pp. 899–907.

[2] D. Bardell. "The invention of the microscope". In: *The Biologists' Forum* 1 (2004), pp. 78–84.

[3] The Royal Swedish Academy of Sciences. *Press release for the Nobel Prize in Physics 1986*. `https://www.nobelprize.org/prizes/physics/1986/press-release/`. Accessed: 2020-7-15. 1986.

[4] G. Totten and D. MacKenzie. *Handbook of Aluminum: Vol. 1: Physical Metallurgy and Processes*. 1st ed. CRC Press, 2003.

[5] M. Graef. *Introduction to Conventional Transmission Electron Microscopy*. Cambridge University Press, 2003.

[6] J. Sunde, C. Marioara, H. A.T.J., and R. Holmestad. "The evolution of precipitate crystal structures in an Al-Mg-Si(-Cu) alloy studied by a combined HAADF-STEM and SPED approach". In: *Materials Characterization* 142 (2018), pp. 458–469.

[7] E. F. Rauch, J. Portillo, S. Nicolopoulos, D. Bultreys, S. Rouvimov, and P. Moeck. "Automated nanocrystal orientation and phase mapping in the transmission electron microscope on the basis of precession electron diffraction". In: *Zeitschrift für Kristallographie - Crystalline Materials* 225.2-3 (2010).

[8] D. Viladot, M. Veron, M. Gemmi, F. Peiro, J. Portillo, S. Estrade, J. Mendoza, N. Llorca-Isern, and S. Nicolopoulos. "Orientation and phase mapping in the transmission electron microscope using precession-assisted diffraction spot recognition: state-of-the-art results". In: *Journal of Microscopy* 252.1 (2013), pp. 23–34.

[9] A. Müller and S. Guido. *Introduction to Machine Learning with Python: A Guide for Data Scientists*. 1st ed. O'Reilly Media, 2016.

[10] G. Burns and A. Glazer. *Space Groups for Solid State Scientists*. 3rd ed. 1990.

[11] D. Mckie and C. McKie. *Essentials of Crystallography*. 1st ed. Blackwell Scientific Publications, 1986.

[12] M. Fultz and J. Howe. *Transmission Electron Microscopy and Diffractometry of Materials*. 4th ed. Springer-Verlag Berlin Heidelberg, 2013.

[13] G. Nolze. "Euler angles and crystal symmetry". In: *Crystal Research and Technology* 50.2 (2015), pp. 188–201.

[14] C. Kittel. *Solid State Physics*. 8th ed. John Wiley & Sons Inc, 2015.

[15] L. Euler. *Formulae generales pro translatione quacunque corporum rigidorum*. 1st ed. 1776, pp. 201–203.

[16] R. Egerton. "Choice of operating voltage for a transmission electron microscope". In: *Ultramicroscopy* 145 (2014), pp. 85–93.

[17] G. Y. Fan and M. H. Ellisman. "Digital imaging in transmission electron microscopy". In: *Journal of Microscopy* 200.1 (2000), pp. 1–13.

[18] D. Williams and C. Carter. *Transmission Electron Microscopy: A Textbook for Materials Science*. Vol. III. June 2009.

[19] S. Chapman. *Maintaining and Monitoring the Transmission Electron Microscope*. Microscopy handbooks. Oxford University Press, 1986.

[20] P. Oleynikov, S. Hovmöller, and X. Zou. "Precession electron diffraction: Observed and calculated intensities". In: *Ultramicroscopy* 107.6 (2007), pp. 523–533.

[21] P. A. Midgley and A. S. Eggeman. "Precession electron diffraction – a topical review". In: *IUCrJ* 2.1 (Jan. 2015).

[22] T. White, A. Eggeman, and P. Midgley. "Is precession electron diffraction kinematical? Part I:: 'Phase-scrambling' multislice simulations". In: *Ultramicroscopy* 110.7 (2010), pp. 763–770.

[23] A. Eggeman, T. White, and P. Midgley. "Is precession electron diffraction kinematical? Part II: A practical method to determine the optimum precession angle". In: *Ultramicroscopy* 110.7 (2010), pp. 771–777.

[24] Y. Matsukawa. *Crystallography of Precipitates in Metals and Alloys: (1) Analysis of Crystallography*. 1st ed. IntechOpen, 2019. Chap. 2.

[25] R. Vissers, M. van Huis, J. Jansen, H. Zandbergen, C. Marioara, and S. Andersen. "The crystal structure of the phase in Al–Mg–Si alloys". In: *Acta Materialia* 55.11 (2007), pp. 3815–3823.

[26] J. Sunde, C. D. Marioara, and R. Holmestad. "The effect of low Cu additions on precipitate crystal structures in overaged Al-Mg-Si(-Cu) alloys". In: *Materials Characterization* 160 (2020).

[27] S. Wenner, L. Jones, C. Marioara, and R. Holmestad. "Atomic-resolution chemical mapping of ordered precipitates in Al alloys using energy-dispersive X-ray spectroscopy". In: *Micron* 96 (2017), pp. 103–111.

[28] H. Hasting, A. Frøseth, S. Andersen, R. Vissers, J. Walmsley, C. Marioara, F. Danoix, W. Lefebvre, and R. Holmestad. "Composition of precipitates in Al-Mg-Si alloys by atom probe tomography and first principles calculations". In: *Journal of Applied Physics* 106 (Jan. 2010).

[29] C. Marioara, N. J., K. Matsuda, S. Andersen, R. Holmestad, T. Sato, T. Kawabata, and S. Ikeno. "HAADF-STEM study of -type precipitates in an over-aged Al–Mg–Si–Ag alloy". In: *Philosophical Magazine* 92.9 (2012), pp. 1149–1158.

[30] C. Wolverton. "Crystal structure and stability of complex precipitate phases in Al–Cu–Mg–(Si) and Al–Zn–Mg alloys". In: *Acta Materialia* 49.16 (2001), pp. 3129–3142.

[31] M. Torsæter, E. F.J.H., C. Marioara, S. Andersen, and R. Holmestad. "Applying precipitate–host lattice coherency for compositional determination of precipitates in Al–Mg–Si–Cu alloys". In: *Philosophical Magazine* 92.31 (2012), pp. 3833–3856.

[32] S. Andersen, C. Marioara, A. Frøseth, R. Vissers, and H. Zandbergen. "Crystal structure of the orthorhombic U2-Al4Mg4Si4 precipitate in the Al–Mg–Si alloy system and its relation to the and phases". In: *Materials Science and Engineering: A* 390.1 (2005), pp. 127–138.

[33] C. D. Marioara, S. J. Andersen, S. T. N., H. Hasting, A. T. J. Walmsley J.and Van Helvoort, and R. Holmestad. "The effect of Cu on precipitation in Al–Mg–Si alloys". In: *Philosophical Magazine* 87.23 (2007), pp. 3385–3413.

[34] E. Rauch and M. Véron. "Automated crystal orientation and phase mapping in TEM". In: *Materials Characterization* 98 (2014).

[35] E. F. Rauch and L. Dupuy. "Rapid Spot Diffraction Patterns Identification through Template Matching". English. In: *Archives of Metallurgy and Materials* 50.1 (2005), pp. 87–99.

[36] M. Bennamoun and G. Mamic. *Object Recognition*. 1st ed. Springer-Verlag London, 2002.

[37] Y. Rao. "Application of Normalized Cross Correlation to Image Registration". In: *International Journal of Research in Engineering and Technology* 03 (May 2014), pp. 12–16.

[38] *Neumann Raufoss*. `http://www.raufossneuman.com/`. Accessed: 2020-07-01.

[39] K. Momma. *VESTA [Computer Software]*. `https://jp-minerals.org/vesta/`. Accessed: 2020-7-15.

[40] P. Stadelmann. *JEMS [Computer Software]*. `https://ecrystsolutions.com/software.html`. Accessed: 2020-7-15.

[41] MTEX development team. *MTEX [Computer Software]*. `https://mtex-toolbox.github.io/`. Accessed: 2020-7-15.

[42] A. M. Korsunsky. *A Teaching Essay on Residual Stresses and Eigenstrains*. 1st ed. Butterworth-Heinemann, 2017.

[43] K. Gjønnes. "On the integration of electron diffraction intensities in the Vincent-Midgley precession technique". In: *Ultramicroscopy* 69.1 (1997), pp. 1–11.

[44] A. Foden, D. M. Collins, A. J. Wilkinson, and T. Britton. "Indexing electron backscatter diffraction patterns with a refined template matching approach". In: *Ultramicroscopy* 207 (2019), p. 112845.

[45] pyXem Development Team. *Polar Reprojection*. `https://github.com/pyxem/pyxem/pull/510`. Accessed: 2019-12-11.

[46] B. H. Martineau, D. N. Johnstone, A. T. van Helvoort, P. A. Midgley, and A. S. Eggeman. "Unsupervised machine learning applied to scanning precession electron diffraction data". In: *Advanced Structural and Chemical Imaging* 5.3 (2019).

[47] Dask Development Team. *Dask: Library for dynamic task scheduling*. `https://dask.org`. Accessed: 2019-12-11. 2016.

[48] G. W. Paterson, R. W. H. Webster, A. Ross, K. A. Paton, T. A. Macgregor, D. McGrouther, I. MacLaren, and M. Nord. *Fast Pixelated Detectors in Scanning Transmission Electron Microscopy. Part I: Data Acquisition, Live Processing and Storage*. 2020. arXiv: 2004.02777.

[49] R. Courtland and D. Müller. *The microscope revolution that's sweeping through materials science*. https://www.nature.com/articles/d41586-018-07448-0. Accessed: 2020-8-21.

Appendix A

Appendix

A.1 Pull Requests to pyXem and DiffSims

Table A.1: All pull requests to pyXem and DiffSims. PR 608 added four new pixel by pixel correlation functions. PR 596 utilizes the phase name information in an automatic way, such that the end user can get the phase name information automatically and conveniently when plotting a phase map or in the code development process. PR 540 introduces a feature creating the rotation matrix axis when rotating about an arbitrary axis with a given angle. However, this feature was already present in the well-established library "transforms3d" that has the function "axangle2mat()" which is probably a safer route for achieving this transformation. PR 532 improved the clarity on the function center_direct_beam() for new users. PR 77 adds a function to the class StructureLibrary that returns the total number of orientations and the possibility to print each identifier(phase) with its corresponding number of orientations(setting to_print = True). PR 76 fixed typographical errors in Diffsims.

Pull request link	Library
https://github.com/pyxem/pyxem/pull/608	pyXem
https://github.com/pyxem/pyxem/pull/596	pyXem
https://github.com/pyxem/pyxem/pull/540	pyXem
https://github.com/pyxem/pyxem/pull/532	pyXem
https://github.com/pyxem/diffsims/pull/77	Diffsims
https://github.com/pyxem/diffsims/pull/76	Diffsims

A.2 Template Matching Notebook

1 Import libraries

[ ]:
```
%matplotlib qt
import diffpy

from diffpy.structure import loadStructure

import pyxem as pxm
from pyxem.generators.indexation_generator import IndexationGenerator
from pyxem.utils.expt_utils import circular_mask

import numpy as np

import matplotlib.pyplot as plt
import matplotlib.animation as animation

from transforms3d.euler import euler2mat

from diffsims.libraries.structure_library import StructureLibrary
from diffsims.generators.diffraction_generator import DiffractionGenerator
from diffsims.generators.library_generator import DiffractionLibraryGenerator
from diffsims.generators.rotation_list_generators import get_local_grid
from diffsims.generators.rotation_list_generators import␣
 ↪get_grid_around_beam_direction
from diffsims.generators.rotation_list_generators import get_grid_stereographic
from diffsims.generators.zap_map_generator import␣
 ↪get_rotation_from_z_to_direction

from pathlib import Path
```

2 Set experimental parameters

[ ]:
```
# Experimental parameters.
accelarating_voltage    = 200     # Acceleration voltage.     Unit: [kV]
camera_length           = 0.2     # Distance sample/detector. Unit: [length]
nm_per_pixel            = 1.28    # Real space step length.   Unit: [length/px]
diffraction_calibration = 0.0208   # Diffraction calibration.  Unit: [px/Å]
```

3 Loading and normalization

[ ]:
```
# Loading the hdf5 dataset.
experimental_data_path = "./Datasets/6082S_3h_c.hdf5"
dp = pxm.load(experimental_data_path, signal_type="electron_diffraction")

# Navigation to smaller area.
dp = dp.inav[73:83, 115:125] # betap

# Make sure the data is in float64 format.
if dp.data.dtype != 'float64':
    dp.data = dp.data.astype('float64')

# Normalization, dp.data $\in$ [0, 1]
dp.data *= 1 / dp.data.max() #

# Set scan calibration.
dp.set_scan_calibration(nm_per_pixel)
```

4 Image preprocessing

[ ]:
```
# Affine transformation, rotation to common frame of reference.
dp.apply_affine_transformation(euler2mat(0, 0, np.deg2rad(31.5), 'sxyz'))

# Alignment of the PED stacks by centering around the direct beam.
# Choose radii and half square width of the center pixel
dp.center_direct_beam('cross_correlate',
                      radius_start = 2,
                      radius_finish = 5,
                      half_square_width = 10)


# Set diffraction calibration
dp.set_diffraction_calibration(diffraction_calibration)

# Create a mask around the direct beam radius
def mask_direct_beam(dp, radius):
    mask = dp.get_direct_beam_mask(radius)
    return mask

# Invert the intensities within the mask, radius 7.
dp.data *= np.invert(mask_direct_beam(dp, 7))
```

5 Load a folder containing all CIF files

[ ]:
```
# Define path to CIF folder.
cif_folder_path = Path("./Cif_database/")

def loadStructuresDirectory(directory):
    files = {
        file.stem : loadStructure(
            ("./" + str(file))) \
        for file in directory.glob("*.cif")
    }
    return files


# Load all structures into a structure dictionary
structure_dictionary = loadStructuresDirectory(cif_folder_path)
```

5.1 (Optional) print all phases in the dictionary

[ ]:
```
def printAllPhases(dictionary):
    print("These are the phases in your cif-folder")
    for phases in dictionary.keys():
        print(phases)

printAllPhases(structure_dictionary)
```

6 Choose which phases to investigate.

```
[ ]: # Choose the phases to investigate: ('name', 'crystal system')
phase_info = (('Betap', 'hexagonal'),
              ('Betadp', 'monoclinic'),
              ("Aluminium", 'cubic'))

# Get the required information from the CIF files for the chosen phases.
def getPhaseDescriptions(phaseInfo, structure_dictionary):
    phase_descriptions = []
    for phase in phaseInfo:
        phase_descriptions.append(tuple((str(phase[0]),
                                         structure_dictionary.
 ↪get(str(phase[0])),
                                         str(phase[1]))))
    return phase_descriptions

phase_descriptions = (getPhaseDescriptions(phase_info, structure_dictionary))
phase_names = [phase[0] for phase in phase_descriptions]
phase_structures = [phase[1] for phase in phase_descriptions]
phase_system = [phase[2] for phase in phase_descriptions]
```

7 Set parameters for simulation.

```
[ ]: max_excitation_error    = 0.004   # $\s_{max}$.           Unit: [1/length]
angular_resolution      = 1       # Sampling step size.   Unit: [$\degree$]
misorientation_angle    = 1       # Misorientation angle. Unit: [$\degree$]
```

8 Use OR to define the rotation list for each phase.

8.1 Aluminium rotation list

[ ]:
```
# Aluminium rotation list around [0,0,1]
al_direction = [0, 0, 1]
rot_list_al = get_local_grid(get_rotation_from_z_to_direction(
    structure_dictionary.get("Aluminium"), al_direction),
    misorientation_angle, angular_resolution)
```

8.2 β'' rotation list

[ ]:
```
# $\beta$'' OR with aluminium
betadp_or_to_al = [0, 1, 0]
beam_rotation_betadp = get_rotation_from_z_to_direction(
    structure_dictionary.get("Betadp"),betadp_or_to_al)

# Create $\beta$'' rotation list according to OR with Al
rot_list_betadp = get_grid_around_beam_direction(
    beam_rotation_betadp, angular_resolution, angular_range=(0, 360))

# (Alternative grid function)
#rot_list_betadp = get_local_grid(
 #   beam_rotation_betadp, misorientation_angle, angular_resolution)
```

8.3 β' rotation list

[ ]:
```
# $\beta$' OR with aluminium
betap_or_to_al = [0, 0, 1]
beam_rotation_betap = get_rotation_from_z_to_direction(
    structure_dictionary.get("Betap"), betap_or_to_al)

# Create $\beta$'' rotation list according to OR with Al
rot_list_betap = get_grid_around_beam_direction(
    beam_rotation_betap, angular_resolution, angular_range=(0, 360))

# (Alternative grid function)
#rot_list_betap = get_local_grid(
 #   beam_rotation_betap, misorientation_angle, angular_resolution)
```

8.4 Q' rotation list

[ ]:
```
# Q' OR with aluminium
qp_or_to_al = [0, 0, 1]
beam_rotation_qp = get_rotation_from_z_to_direction(
    structure_dictionary.get("Qp"), qp_or_to_al)

# Create Q' rotation list according to OR with Al
rot_list_qp = get_grid_around_beam_direction(
    beam_rotation_qp, angular_resolution, angular_range=(0, 360))

# (Alternative grid function)
#rot_list_betap = get_local_grid(
 #   beam_rotation_betap, misorientation_angle, angular_resolution)
```

9 Initialize a structure library generator for the specified phases with the chosen rotation lists

[ ]:
```
all_entries_struc_lib_id = phase_names
all_entries_struc_lib_struct = phase_structures
all_entries_struc_lib_orientations = [rot_list_betap,
                                      rot_list_betadp,
                                      rot_list_al]

struc_lib = StructureLibrary(all_entries_struc_lib_id,
                             all_entries_struc_lib_struct,
                             all_entries_struc_lib_orientations)
```

9.1 (Optional) Print the number of entries in the template bank

[ ]:
```
struc_lib.get_library_size(to_print = True)
```

10 Simulate diffraction for the chosen template library

[ ]:
```
diff_gen = DiffractionGenerator(accelerating_voltage=accelarating_voltage,
                                max_excitation_error=max_excitation_error)

lib_gen = DiffractionLibraryGenerator(diff_gen)

target_pattern_dimension_pixels = dp.axes_manager.signal_shape[0]

half_size = target_pattern_dimension_pixels // 2

reciprocal_radius = diffraction_calibration*(half_size - 1)


diff_lib = lib_gen.get_diffraction_library(struc_lib,
                                           calibration=diffraction_calibration,
                                           reciprocal_radius=reciprocal_radius,
                                           half_shape=(half_size, half_size),
                                           with_direct_beam=False)
```

10.1 (Optional) Animate diffraction library for visual inspection

[ ]:
```
list_of_orientations = struc_lib.orientations
plot_intensities = np.zeros((target_pattern_dimension_pixels,
                             target_pattern_dimension_pixels))
ims = []
fig = plt.figure()
fig, axs = plt.subplots(1, 1, figsize=(6, 6))

phase = 0;
for j in range(0, len(list_of_orientations[phase])):
    angle = (list_of_orientations[0][j][0],
             list_of_orientations[0][j][1],
             list_of_orientations[0][j][2])
    library_entries = diff_lib.get_library_entry(
        phase = 'Aluminium', # #Choose phase to animate!
        angle = angle)

    intensities = library_entries['intensities']

    coordinates = library_entries['pixel_coords']

    for i in range (len(intensities)):
        plot_intensities[coordinates[i,0],coordinates[i,1]] = intensities[i]

    im = plt.imshow(plot_intensities,
                    cmap = 'inferno',
                    animated = True)

    title = axs.text(0.5,1.05,
                    'Rotation Angles: [{0:.2f},{1:.2f},{2:.2f}]'.format(*angle),
                    size=plt.rcParams["axes.titlesize"],
                    ha="center", transform=axs.transAxes,)

    ims.append([im, title])

ani = animation.ArtistAnimation(fig, ims, interval=20, blit=False)

plt.show()
```

10.1.1 Visual inspection of Al and β'

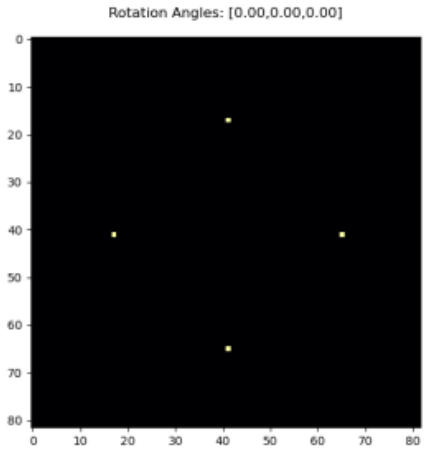

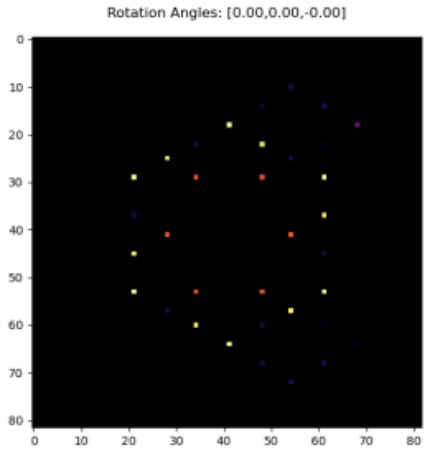

,

10.2 (Optional) Save diffraction library

[ ]:
```
diff_lib.pickle_library('./diff_lib_phases.pickle')
```

11 Matching of the templates vs the experimental patterns.

[ ]:
```
indexer = IndexationGenerator(dp, diff_lib)

# The methods tested have been, NCC, ZNCC, SAD and SSD.
indexation_results = indexer.correlate(
n_largest = 2, method = "normalized_cross_correlation")

indexation_results.data
crystal_map = indexation_results.get_crystallographic_map()

# Plot the phase map.
crystal_map.plot_phase_map(diff_lib)

# Plot the best matches as an overlay on the signal.
indexation_results.plot_best_matching_results_on_signal(
    dp, diff_lib, diff_gen, reciprocal_radius)
```

Endre Jacobsen

SPED Matching for Automated Phase Mapping of Precipitates in Al Alloys

NTNU
Norwegian University of
Science and Technology